Fabrication of Single-Crystal Sapphire Fibres for Sensor Applications

Mengchuan Xing

Submitted in fulfilment of the requirements for the degree of Doctor of Philosophy (PhD)

College of Science & Engineering

Declaration

I declare that the work presented in this thesis, except those specifically declared, is all my original work carried out and finished at University of Glasgow. The copyright of this thesis therefore belongs to the author and due acknowledgement must be made if any material from within is used.

Abstract

For this thesis, single crystal sapphire fibres, have been successfully fabricated as suitable sensor materials through the laser heated pedestal growth technique. Lab-produced aluminium oxide rods, commercial aluminium oxide ceramic rods, and sapphire wafer slices were used as source materials. Pure sapphire fibres with diameters in the range of 300 – 350 µm, both c-axis and a-axis, of high optical quality were fabricated. Some growth issues were encountered including diameter variation and an asymmetric molten zone. These were analysed and solved in the multiple growth trails. Seed orientation dependent longitudinal facets were observed in the sapphire fibres; by using accurately aligned c-axis sapphire crystals as a seed, these facets were eliminated.

Three new types of sapphire fibre sensor structures were designed and fabricated via the laser heated pedestal growth system: a monolithic sapphire capillary blackbody radiation sensor, a monolithic sapphire capillary Fabry-Perot interferometer sensor and a long-period sapphire fibre grating sensor. For the blackbody radiation sensor, a robust blackbody cavity was fabricated by combining silicon carbide and sapphire at high temperature. The use of the sapphire capillary provides a strong protection of the inner transmission fibre, and the controllable size and shape of the cavity can help to manipulate the radiation signal generated. In the case of the Fabry-Perot interferometer sensor, the monolithic closed sapphire endcap design was developed, tested and evaluated. It was found that the internal surface of the end cap was not to be as good optical quality as was expected from the high surface tension of molten sapphire closing the capillary end under heating. The successful development of the crystal insertion method significantly improved the production success rate of the inner reflective surface of the sensor and would improve its stability as a potential high-temperature sensor. As for the long-period grating sensor, by employing the mechanical speed variant technique in the sapphire fibre growth procedure, innovative sapphire fibre gratings were successfully fabricated with the period in a range of 40 – 1000 µm.

To select the suitable sensor for further investigation and development, initial tests were conducted to build the sensing systems for the three sensor candidates fabricated. Challenges were found during this procedure, which provided significant guidance for building sapphire-based sensing systems. Due to its innovative results and outcomes, the long-period

sapphire fibre grating sensor was selected as the most suitable sensor for further development. In the investigation, a clear grating effect was observed in the form of the appearance of a resonant wavelength region, which exhibited a clear shift dependent on cladding refractive index. A back-coupling effect was seen in the gratings with a large period (700 – 900 μm) and fractional amplitude modulation values (0.02). The back-coupling effect was seen in the form of a rise in the signal strength as a resonant peak (RP), which could be clearly located in the spectrum. In the refractive index sensing experiment, the RP of the back-coupling sensor showed clearer wavelength shifts than the resonant wavelength region in the original sapphire fibre long-period grating sensor. In temperature sensing experiments, a strong linear relationship between the wavelength shift of the RP and the ambient temperature was obtained with sensitivity of 2.5 nm/ °C. Furthermore, a unique collimated white light output beam of the long-period sapphire fibre gratings was found and characterised with a significantly decreased divergence angle (6°) and various pseudo-coherent properties such as focusing, collimation, and directionality.

Acknowledgement

First of all, I would like to express my great appreciation to my supervisor, Dr. James Sharp, for giving me this opportunity to continue and contribute to my favourite research topic, fibre optics sensors. During the course of this project, Jim was always there whenever I had a spot of trouble in practical experiments or a difficult theoretical question, even when he was on holiday or ill. Every meeting with him inspires me forward. He consistently allowed this project to be my own work but steered me in the right direction whenever he thought I needed it. His openness, patience, and understanding provided me a fantastic academic atmosphere. Throughout this project, I always felt proud and lucky to have a such nice supervisor. Without his guidance, this work would not have been realised. Thank you, Jim.

Besides my advisor, I would like to thank staff in James Watt Nanofabrication Centre, for offering opportunities to use different equipment. In particular, Dr. Song Tang and Dr. Shengwei Ye are thanked for coaching me and answering my questions at any moment. Discussion with them always enlightened me in my academic life.

I would also like to thank my best Scottish friend, Christopher Connolly, who helped me with my English not only in this thesis, but also in everyday life. His willingness to give his time generously has been very much appreciated. His sincerity and diligence towards life and work also encouraged me to live a better life during my study in Scotland. Friendship with him makes me always feel a strong attachment to this land.

Finally, I would like to give my utmost appreciation and thanks to my parents in China, who always save the best for me and keep difficulties to themselves. My father, a prominent engineer, who supports me spiritually and financially, who always encourages me when I am down. My mother, a caring doctor, who always believes in me, who devotes herself to our family and takes care of my father and my sister when I am gone. Here I would like to give my deepest love to both of you for your devotion to our family and me.

Contents

List of Figures

Abbreviations

SCF	Single-crystal Fibre
RF	Radio Frequency
EFG	Edge-defined Film-fed Growth
LHPG	Laser-heated Pedestal Growth
YAG	Yttrium Aluminum Garnet
OFS	Optical Fibre Sensor
EMI	Electromagnetic Interference
RFI	Radio-frequency Interference
BBR	Black-body Radiation
FBG	Fibre Bragg Grating
LPFG	Long-period Fibre Grating
SCBBR	Sapphire Capillary Blackbody Radiation
SCFPI	Sapphire Capillary Fabry-Perot Interferometer
LPSFG	Long-period Sapphire Fibre Grating
SiC	Silica Carbide
MSV	Mechanical Speed Variant
FAM	Fractional Amplitude Modulation
RW	Resonant Wavelength
CL	Collimated Lens
MO	Microscope Objective
MNC	Monochromator
LIA	Lock-in-amplifier
PD	PIN Photodetector
RI	Refractive Index
RWR	Resonant Wavelength Region
BC	Back Coupling
BCG	Back Coupling Grating
RP	Resonant Peak
BCB	Back-coupling Beam
FFT	Fast Fourier Transform

Chapter 1 – Introduction

1.1 Research Context

Optical fibres have been widely used in the telecommunications field for decades. Their high bandwidth and low attenuation characteristics make them an attractive option for transmitting large volumes of information over a long distance. At the same time, because of their advantages of small size, low cost and immunity to electromagnetic interference, optical fibres have also been utilised for sensor applications; for measuring various physical quantities such as temperature, pressure and refractive index. However, due to the intrinsic physical properties of conventional glass/plastic fibres, there are some material limitations of certain parameters of interest such as strain and temperature which, in effect, limit the sensing range of the sensors. Crystalline optical materials possess properties which are often not seen in conventional fibres. For example, yttria and sapphire single-crystal materials have very high strength and melting points as well as useful optical properties. Therefore, in recent years, small crystal sections have been used as the passive delivery or collection media in some optical fibre sensors. With further advanced fabrication techniques, the quality of single-crystal materials produced is constantly improving, and it would thus be greatly advantageous if such materials could be grown in a fibre form for developing a new generation of optical fibre sensors for particularly extreme environments. Therefore, the aim of this project is to use the laser heated pedestal growth technique to fabricate high-quality single crystal sapphire fibres in order to combine the growth method with optical fibre sensing techniques for development of harsh environment sensors. Three novel sensors have been proposed, designed, fabricated and assessed for practical implementation.

This thesis is composed of nine chapters. **Chapter 2** introduces single-crystal fibres in terms of a comparison with conventional fibres, their origin and development, fabrication techniques, and latest applications.

Chapter 3 begins with an introduction of current fibre optic sensing technologies with an emphasis on three sensing techniques that are to be studied in this project. This is followed by a brief review of the latest sapphire fibre-based sensor development for each of these sensing techniques.

Chapter 4 discusses the design and construction of the laser heated pedestal growth system. The growth of sapphire fibres is described together with the issues met in the procedure. The issue analysis and performance improvement of the growth system are then presented.

In **Chapter 5**, the design and fabrication of three innovative sapphire fibre sensors are carried out. The design concepts of each sensor are introduced with comparisons to the latest corresponding sensing techniques. Different fabrication methods of each sensor are tested and reported with the optimal methods selected at the end.

Chapter 6 details the procedure of building sensing systems for sapphire fibre Fabry-Perot interferometer and blackbody radiation sensor. Different types of systems are designed, and components are tested for the most suitable system. The challenges and issues of each sensing systems are reported and analysed with corresponding solutions proposed.

The optical sensing experimental system design and construction of long-period grating sensor are covered in **Chapter 7.** The optical response of the sensor is then studied followed by a refractive index sensing experiment. The sensing capacity of the sensor is evaluated in terms of the pros and cons.

In **Chapter 8**, the discovery of the back-coupling effect in long-period sapphire fibre gratings is investigated. The sensing experiments of the back-coupling grating sensor in terms of refractive index and temperature are conducted and reported. A special back coupling beam is found and characterised. The development and potential application of the back-coupling effect are also discussed.

Chapter 9 concludes with a summary of the main project contributions. Some recommendations of further work in developing the growth system and potential sensors are also offered together with a short discussion in sapphire fibre cladding as a start to commercialisation of the sensor products.

Chapter 2 – Introduction to Single-Crystal Fibres

Chapter 2 – Introduction to Single-Crystal Fibres

2.1 Introduction to optical fibres

Optical fibres, arguably a key enabling technology of recent times, have been around for over a century. As a universal medium for transmitting information, optical fibres are widely used nowadays, not only in the communication field, but also in varied sectors such as mechanical inspection, broadcasting, sensing, and the medical industry primarily because of their unique properties and advantages such as small size, low transmission loss, great flexibility and low cost.

As is shown in Fig. 2.1, a typical optical fibre is a long transmission cable made of glass or plastic, which usually consists of a core, a cladding, and a buffer or coating. The buffer or coating is used to protect the optical fibre from mechanical damage. The core of the fibre has a larger value of refractive index than the cladding material. This constrains light in the core by the process of total internal reflection as it travels down the length of the fibre, this is illustrated in Fig. 2.2 below and discussed in detail in reference [2.1].

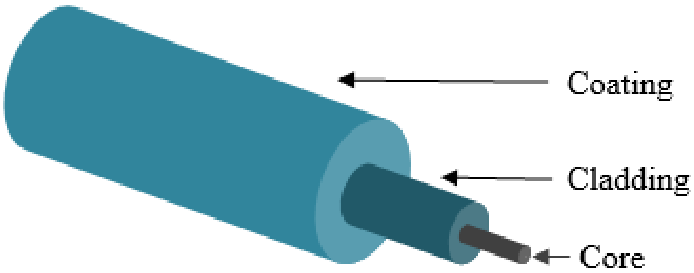

Figure 2.1. Structure of a typical optical fibre

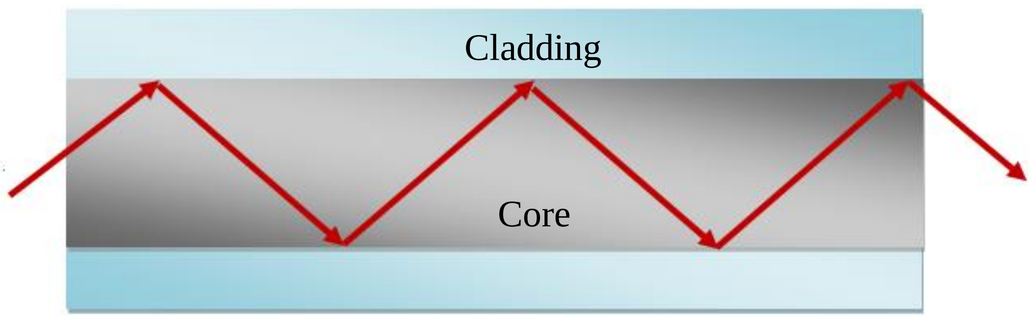

Figure 2.2. Total internal reflection in the optical fibre

Characterised by the size of the core or the number of modes of propagation, optical fibres can be broadly classified into single-mode fibres and multi-mode fibres. Single-mode fibres have cores of a narrow diameter of around 3 to 10 μm; this narrow diameter only allows one transverse mode to propagate. Multi-mode fibres have a much larger core. The core of the multi-mode fibre is usually above 50 μm in diameter, which allows light to pass in numerous transverse modes. However, with the increased number of transverse modes available, multi-mode fibres can carry more information than single-mode fibres concurrently [2.2]. This advantage is typically utilised in occasions where transmissions of a large volume of information is required, but over a relatively short distance, such as computer networks and video applications.

Considering material composition, optical fibres can also be divided into different categories, including glass, plastic and crystal fibres. The glass fibre is an optical fibre made up of single strands of typically silica-based glass. As the earliest and the most conventional optical fibre, the glass material in the fibre is efficient at transmitting light with relatively low loss, hence the common use for long-distance transmission. Moreover, glass fibres can work in a wide temperature range, as low as -5 °C, and as high as 500 °C [2.3]. This property has allowed glass fibres to become an excellent choice for sensing applications in extreme environments such as cold storage rooms, furnaces and ovens.

The plastic (or polymer) optical fibre, can be made from a range of plastic material. A conventional plastic fibre consists of a core made of poly methyl methacrylate and the cladding made of fluorinated polymers [2.3]. Compared with glass fibres, plastic fibres are less expensive and more flexible. They have higher resiliency to bending and vibrations than glass fibres. Unlike glass fibres, with plastic fibres, it is more straightforward for them to be cut and reused without then need for specialised techniques or tools. With regards to transmission, plastic fibres are more suitable for low-speed, low-attenuation applications, and for relatively short distances (between 100 m to 200 m), such as home or industry networks, car networks and military communication networks [2.3].

The crystal fibre is a type of fibre with special structures and unique properties, which have become a new hot topic of interest in both academic and commercial circles over the past decades or so. When considering “crystal” optical fibres, it is necessary to be careful to distinguish single-crystal fibres (made from single-crystal material) and photonic crystal fibres (made from glass). Photonic crystal fibres are also called microstructure fibres, or “holey” fibres. While most photonic fibres are made from pure fused silica, some are made of various other materials such as polymers [2.4]. A photonic crystal fibre has, in its cross-section, a honeycomb microstructure of cavities or air holes, excepting a single defect in the centre of the fibre. In a traditional fibre, the light transmits due to total internal reflections in the high refractive index medium making up the core; However, in a photonic fibre, due to its unique structure, the light is forced to transmit in the low refractive index medium, the air holes [2.4]. Since the energy of transmitted light is gathered in the air, the fibre material is protected from damage caused by very large intensities; thus, high-power transmission can be achieved by using photonic fibres. As a result of their special structure, photonic crystal fibres are applied in various areas including nonlinear devices and fibre lasers.

Single-crystal fibres (SCFs) are made of single crystals. Since an effective fabrication method for growing SCFs was unavailable until relatively recently, most of the research on SCFs has only started over the last three to four decades. With the development of fabrication techniques, the significant advantages of SCFs, both mechanical and optical, are being found and applied in many structural and optical applications such as fibre lasers, high power beam transmission, and sensors. As the core subject of this thesis, SCFs are discussed in greater depth in the following sections.

2.2 The origin of single-crystal fibres

The earliest studies on SCFs was focused on their mechanical advantages such as high temperature resistance, high resistance to scratching and abrasion, and high resistance to chemical attack. During this time, the greatest interest was in using SCFs as reinforcing materials for structural applications. However, because of the high cost of producing SCFs, and the fact that no efficient commercial fabrication method was yet invented, interest waned in the wake of the advent of other low-cost structural reinforcing alternatives. As the technology underpinning optical communication appeared and developed, the interest on SCFs was rekindled. This was primarily to investigate its efficacy as fibre lasers, and for electro-optic applications. Although SCFs in fibre form in lengths comparable to glass were still not available at this time, single-crystal materials became a much more attractive prospect than before, once their optical advantages were understood; for example, excellent optical transmission range and excellent crystalline perfection. Based on the fabrication method of glass fibre, lithium niobate became the first material that could be grown in crystal fibre form, from which was found the potential applications of non-linear optical devices [2.5].

The first reported case of optical fibres in crystalline material was in 1887. A new method was developed to produce SCFs. In this method, an oxyhydrogen flame was used to heat the middle part of a thin quartz rod which was cemented to a straw arrow at one end. The fibre could be produced by pulling the other end of the arrow while heating [2.6]. The fibre produced with this method was about 0.25 mm in diameter and 25cm in length. Although it was proved the fibre was not a true single optical crystal, it indicated the quartz fibres could be manufactured with a high tensile strength by this method. With this idea of pulling fibres for SCF production, in 1967, LaBelle and Mlavsky [2.7] successfully produced sapphire fibres with diameters of 0.1 to 0.5 mm and lengths over 30 cm with a developed method. In their research, a molybdenum crucible was used to hold the sapphire rod and a radio frequency (RF) heating system was used to heat the tip of the sapphire rod instead of an oxyhydrogen flame. By adjusting the heating temperature, the tip of the sapphire rod was heated near to its melting point and fibres could be pulled from the melt. This method was developed in time to become the edge-defined film-fed growth (EFG) method. With the EFG technique, crystal fibres can be commercially produced with improved growth speeds (up to 5 cm/min) and various cross-sectional shapes [2.8].

1970 marked the first use of lasers applied to SCFs growth. Two CO_2 lasers with powers of 400W were first used to heat and melt the single-crystal source material [2.9]. In this technique, the seed and source rod of single crystal material were held by mechanical chucks. With the two beams from lasers focusing on the connection point of the source rod and the seed, a molten zone was created. A crystal fibre could then be pulled from the molten zone. With the help of CO_2 lasers, the maximum temperature at the tip of material in growth process was increased up to 2500 °C and various materials, for example, $CaZrO_3$, $MgAl_2O_4$ and Al_2O_3, could be grown as single crystals. However, the diameter of these crystals was relatively large, approximately 5 mm in diameter, and hardly classed as fibre. Five years later, Stone and Burrus [2.10] improved this method by adding rotation to the seed and source holding chucks, which helped the molten zone to be heated evenly. A thin platinum wire was used as source rod to dip into the molten zone created by CO_2 lasers. By pulling the wire upward, a SCF fibre with a diameter of 50 μm and length of 20 cm was produced. The quality of SCFs grown by this method was improved, and the single crystals in fibre form were applied in the production of single crystalline fibre laser devices.

A significant breakthrough in the fabrication of SCFs occurred in 1980s. Beam positioning and focusing mirrors, as one of the major changes, were designed and applied to help heat the source material symmetrically. Other innovations such as no crucible requirement and a closed loop diameter monitor system, greatly improved the quality of the SCFs grown. With this new technique, crystal fibres with high quality could be produced with little or no impurity [2.11]. Furthermore, this technique requires only a small amount of source material to be used for production, which lowered the economic cost of material studies and made it possible to grow multiple samples per day with expensive materials [2.12]. This fabrication method is now known as laser-heated pedestal growth (LHPG) technique and plays a significant role in producing high-quality SCFs as components for lasers, sensors, and many electronic and optical devices. In the next section, the principles and methodology of the LHPG technique will be discussed in detail along with a comparison with the EFG technique.

2.3 Fabrication of single-crystal fibres

There are essentially two widely used techniques to fabricate SCFs: EFG and LHPG. Each technique has its respective advantages and applications. Regarding the EFG technique (Fig. 2.3), a cold tungsten wire, or a seed fibre, is used; this is plunged into a molten reservoir and pulled out, drawing a fibre from it. The molten material, which serves as the source material for the SCFs, is contained by a high-temperature tungsten or platinum crucible; the crucible is placed in a furnace, usually a large quartz tube, and heated by a RF heating system; a die in the form of a capillary tube, usually made of molybdenum, is used as a shaper. It is worth noting that to avoid rapid oxidation of the molybdenum materials, growth must be undertaken in an inert atmosphere. In the growth process, a shaper, acting like a wick, is inserted into the melt to pass the molten material to the upper surface of the shaper. Once the melt wets the shaper surface and contacts with the seed, the seed is withdrawn. The melt is then crystallized into fibre form at the contact area between the shaper and the seed [2.13]. The schematic of the EFG process is shown at the left in Fig. 2.3. The geometry of the grown crystal fibres is not only defined by the seed, but also the profiles of the shaper, such as size and angle. Factors such as the pressure of the melt on the shaper and the relative position between seed and shaper also influence the quality of the growing fibre.

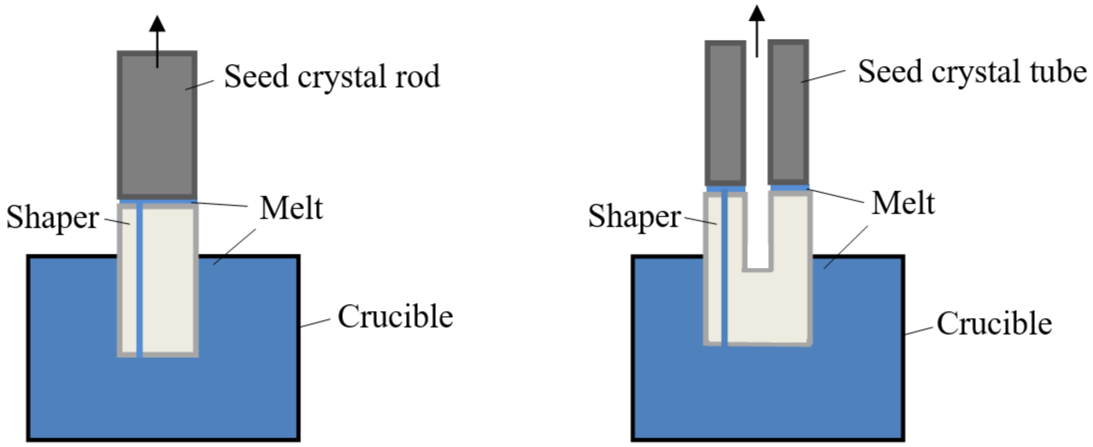

Figure 2.3. Schematic of EFG process

There are two inevitable issues which arise with this growth technique. One is that since shapers and crucibles are used during the whole process, inevitably some contamination occurs between the crystal and crucible/shaper materials. This decreases the purity of SCFs grown. In addition, the use of shapers and crucibles limits the flexibility of growth. The diameter of the fibre is defined by the inner diameter of the capillary shapers; thus, the shapers need to be changed if fibres with different diameters are required, which is inconvenient. Moreover, the material of shapers and crucibles must be matched with the molten crystalline material so that they do not react at high temperature and sufficiently wet the shaper material; the melting points of the shapers and crucibles also limit the type of materials that can be grown. However, the benefits of such techniques are immediate as well. Various cross-sectional shapes of single crystal can be fabricated by simply changing the shapers, for instance, single crystal tubes (or hollow fibres) can be produced from the shaper shown at the right in Fig. 2.3. The other advantage is that by utilizing a specially-made shaper for EFG growth, multiple fibres can be grown at the same time, which can enhance efficiency in manufacture. *Saphikon, Inc.* successfully commercialised sapphire fibre products with the help of the EFG technique in 1998 and has become one of the world's leader in manufacturing diverse sapphire products, including fibres, tubes, windows, rods and other complex shapes [2.14].

Unlike the EFG technique, the LHPG technique does not involve the use of shapers or a crucible. The hardware structure and the growth procedure of LHPG is simpler than in EFG. In LHPG, the main CO_2 laser beam is split and expanded into a cylindrical beam by a series of beam guiding components including a reflaxicon, plane elliptical mirror and parabolic mirror. The plane elliptical mirror is placed at 45° to the horizontal. It reflects the cylindrical beam (produced by the reflaxicon) onto a parabolic mirror. The parabolic mirror focuses the beam onto the tip of the source rod to provide heating and melting. The schematic of the laser beams in the LHPG process is shown in Fig. 2.4. Once the material at the focus point is heated to its melting point, a small molten zone is created at the tip of the source rod. The seed crystal is dipped into the molten zone and a SCF can be formed by slowly lifting the seed from the molten zone. During this process, the source material is replenished by feeding the source rod upward continuously. In this dynamic balance, a crystal fibre can be drawn to the desired length, as shown in Fig. 2.5.

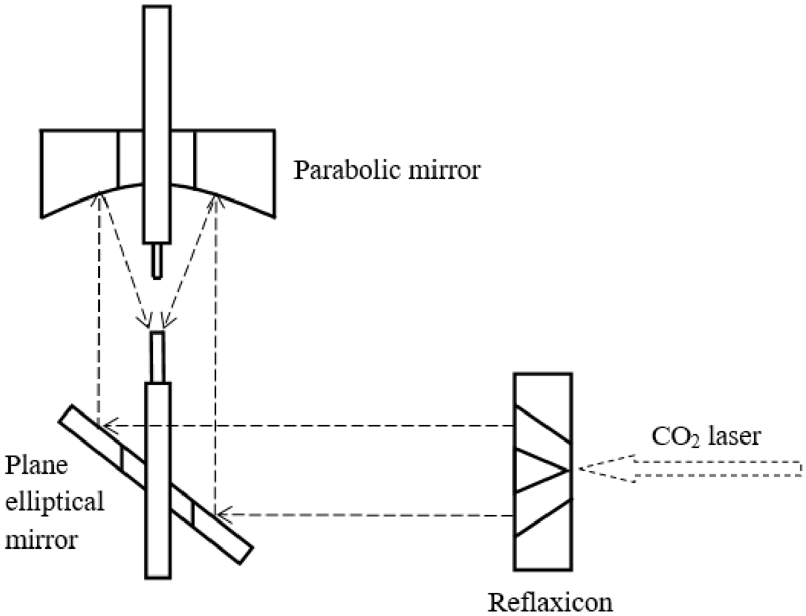

Figure 2.4. Schematic of laser beam in LHPG

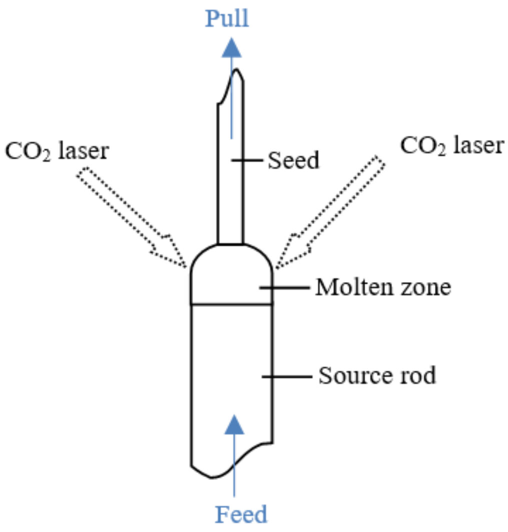

Figure 2.5. Schematic of growth process in LHPG

Compared with the EFG technique, in LHPG, the size of the molten zone is a function of the power of the CO_2 laser. At the tip of the source rod, the molten zone is simply held by surface tension, thus, any fluctuations in laser power, or external disturbance such as experiment bench movement, or air currents in the environment, can influence the stability of growth. Because of this, a very stable laser source is required in the growth, and the growth system has to be isolated from the environment as far as possible. Although the LHPG technique can only grow one fibre at a time, it has some notable advantages over the EFG technique. Firstly, since it is a crucibleless technique and there is no contact between melt and shapers or crucible, this greatly eliminates contamination or impurities between materials, so SCFs with high purity (limited only by source rod) can be grown. Secondly, the CO_2 laser, as the heating source, can provide uniform heating, and the maximum temperature which can be achieved is limited only by available laser power. The laser also provides the significantly more localised heating when compared with RF furnace heating and oxyhydrogen flame heating. Lastly, this technique saves source materials in two aspects. First is that the molten zone in LHPG is much smaller compared with the molten reservoir in EFG (there are always unused materials left on the crucible walls and inside the shapers after growth in EFG). In the LHPG process, the molten zone is small (~ 0.5 mm^3) and almost all the melt is grown into a fibre. At the end of process, the melt that is not used will stay on the tip of source rod for the next growth. Secondly, since the size of the molten zone is small, only small amount of source materials are needed and experimental materials can be grown at lower cost. With these inherent advantages, especially its ability to fabricate high optical-quality SCFs, LHPG has been considered as the best growth technique for growing SCFs in the research field since it was developed in Stanford University [2.15].

The state of art of LHPG studies can be divided into two aspects: material study and LHPG development. For material study, the LHPG technique has been used to grow various materials including but not limited to oxides, fluorides, non-linear optical materials, superconductor and semiconductor materials, and most of all, SCF materials. In the most recent studies since 2010, the material studies using LHPG has been mainly focused on developing new types of crystalline fibres. In 2010, 25 mm length and 1 mm diameter of KDP doped L-arginine phosphate fibres were grown by LHPG with almost 100% transparency in the 250-1200 nm region, which makes it a potential material with higher damage threshold and higher nonlinearity to replace the KDP used presently as harmonic generator [2.16]. Up to 2014, a wide range of single crystal rare-earth (erbium, holmium, thulium, etc.) doped YAG fibres with different concentrations have been fabricated by LHPG technique for high power applications such as solid-state lasers [2.17]. In 2017, a new flexible fibre with a core of dopant (Nd, Er, Yb, etc.) and a polycrystalline cladding of YAG was fabricated by LHPG technique, which exhibited good waveguiding properties in the further experiments [2.18]. These achievements confirmed the potential of LHPG for developing different types of SCFs to overcome the limitations of the conventional glass fibres in the development of new types of high-power compact fibre lasers and amplifiers.

With regard to the LHPG development, the current studies are focused on enhancing functions of the LHPG system. To improve the success rate and stability of growth, the appearance, shape, and temperature of different parts of growing fibres were studied. To ensure the consistency of the diameter of the growing fibres, an automatic diameter control system based on an artificial vision apparatus was developed for the LHPG technique in 2002 [2.19]. This diameter control system successfully reduced the diameter fluctuation of growing fibres to less than 2%, which improved the growth stability and offset the diameter variation problems caused by unwanted laser power fluctuations. To improve the quality of SCF grown by LHPG, in 2013, both three-dimensional simulation and experiments were conducted to study the micro-floating zone of the LHPG, indicating that the shape of the molten zone is influenced much more strongly by an asymmetrical heating effect than by the presence of a gravity field [2.20]. In 2016, a thermal radiation spectral measuring method was used to monitor the temperature distribution of the melting zone of growing fibres in LHPG [2.21]. The result in the study indicated that the temperature of the molten zone can significantly influence the convective flows in the melt, which can change the mass transfer process of the growing material, and thus the growth condition. The existence of a local temperature minimum in the area of the source rod melting region can be determined through this method to help stabilise growth by keeping a constant melting zone temperature. These developments help the LHPG technique to realize automation control and simplify the manual operation and management, developing the efficiency and quality of SCF growth to a higher level.

2.4 Single-crystal fibres and their applications

Unlike standard optical fibres that have a core/cladding structure, as a special type of fibre, SCFs have historically been very difficult to clad due to the low viscosity of molten crystal materials (compared to glasses). As a result of the large difference of refractive index at the crystal-air interface, multimode waveguiding is achieved in sapphire fibres. In material science studies, SCFs are known as “crystal whiskers” [2.22], which are single crystals of tiny size, low impurity, and high crystalline perfection. Several oxide crystals that have been used for producing SCF optics, including sapphire (Al_2O_3), YAG ($Y_3Al_5O_{12}$), GGG ($Gd_3Ga_5O_{12}$), and Spinel ($MgAl_2O_4$). Among these, sapphire and YAG are the two often most mentioned materials in both active and passive applications of SCF optics [2.23]. As sapphire (Al_2O_3) is the most common SCF material studied to date, it is worth commenting on some of its material properties. It is an insoluble, uniaxial crystal. Sapphire fibres have a high melting point at 2050 °C while conventional glass fibres soften and stop working at 1200 °C. Also, sapphire is extremely hard and robust as its Young’s Modulus (345 GPa) is about 6 times larger than that of glass (60 GPa). Moreover, sapphire fibres have excellent optical transmission ranging from 150 to 3200 nm. As it is shown in Fig 2.6, sapphire fibres have a hexagonal structure, and there are two principal optical axes: namely a-axis and c-axis; the longitudinal axis is the c-axis. Light transmitted in c-axis direction has the lowest magnitude of birefringence, which is discussed in [2.24]. YAG fibres are probably the next most common kind of single-crystal fibre due to its popularity as a laser host crystal. Although they have a lower melting point than the sapphire fibres, YAG fibres do not produce birefringence through transmission due to their cubic structure. Also, after fabrication, YAG fibres are easier to polish than sapphire fibres.

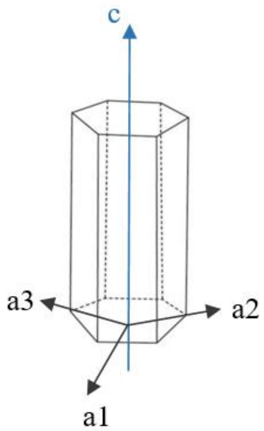

Figure 2.6. Structure of sapphire crystal

Owing to their remarkable mechanical and physicochemical properties such as high melting point, high strength, and high thermal conductivity, SCFs have been widely used in various applications. These applications include, but are not limited to, solid-state lasers, non-linear optics, and superconducting materials. In recent decades, they have been applied in the optical fibre sensing field, especially in harsh environments.

One of the major applications of SCFs is in solid-state and single crystalline fibre lasers. This has been studied and developed since 1964, when Nd^{3+}-doped YAG garnet crystal was first utilised as a material for solid-state lasers [2.25]. In terms of laser geometry, SCFs have a large propagation length that can achieve a high optical gain. Also, SCFs have a high optical damage threshold which means they can deliver much higher optical powers than conventional materials like glass. Some SCFs also have high strength, which can aid the deliver process and prolong the service life of instruments. For these reasons, SCFs have become an ideal material in the domain of ultrashort pulse amplification in multimode fibres.

Due to the special structure and waveguiding geometry of SCFs, they are also used in studies of non-linear optics. For the same amount of optical power, SCFs can provide higher optical gain and nonlinear efficiency than traditional bulk counterparts [2.26]. Also, by varying the impurity in SCFs, desired optical properties can be optimised. The earliest instance of this application is an example from 1988, a barium metaborate single-crystal fibre was produced by LHPG and succeeded in phase matching harmonic generation in the range of 200 to 1500 nm [2.26]. By applying doping techniques in single-crystal growth, different SCFs with unique properties can be produced and create more possibilities in the fibre optics field.

Since 1989, there has been increasing interest in growing high temperature materials in single-crystal form. SCFs and their growth techniques have been used in creating novel superconducting materials, for instance, superconducting ceramics. Since superconducting ceramics can have unstable reactions while melting, growing this material becomes a difficult task. Growing superconducting ceramic in SCF form allows it to have a fixed orientation as single crystals while enhancing its original properties such as high temperature resistance. With the help of the LHPG techniques, the density of the superconducting ceramics grown can be well controlled and the efficiency of growth is improved [2.27].

In the early 21st century, utilising SCFs in optical sensing applications in harsh environments became an emerging research focus. Sapphire fibres, as the most popular SCFs in these studies, are very regularly used as sensing probes in high temperature environments. With the participation of single-crystal fibres, the superiority of fibre optic sensors over conventional electronic sensors becomes more and more evident, especially in harsh environments. In the current research, SCFs have been utilized in many optical fibre sensing techniques in terms of temperature, strain and radiation. As the main contents of this thesis, SCF sensing techniques and applications are discussed in detail in **Chapter 3**.

To maximise the range of SCF applications, the most recent studies of SCF include improving SCF properties and functionality and investigating SCF claddings. In the case of the improvement of SCF properties and functionalities, the latest studies have been focused on developing new types of fibres using different methods. In 2010, single crystal sapphire was used to fabricate the sapphire photonic crystal fibre [2.28]. The fabricated fibre consists of six symmetrical holes arranged with the outer single crystal sapphire layer surrounding the solid single crystal sapphire core. It is the first-time repeated fabrication of photonic crystal fibres using single a crystal material, which combines the advantages of single-crystal fibres and photonic fibres together and has a huge potential in high-temperature sensing and communication applications. In 2015, a new type of single crystal sapphire fibre with a reduced number of guided modes was fabricated. The diameter of a 10 cm length of commercial sapphire fibre was reduced from 125 μm to 6.5 μm by the high-temperature wet acid etching method. The single-mode propagation effect was observed above 783 nm in the fabricated single-mode air-clad sapphire fibre [2.29, 2.30]. With the extremely large modal volume of sapphire fibres decreased, the resolution of the sapphire fibre sensors that requires low modal volume may be increased, such as Bragg grating, long-period grating, and Fabry-Perot interferometer. In 2017, [2.31] reported the first growth of a SCF of Pr:KY_3F_{10} (KYF). This material is a promising laser material, especially for solid-state laser operations. In 2018, α-Al_2O_3 SCFs were successfully grown from the source material of single-crystal α-Al_2O_3 whiskers and Al_2O_3 particles synergistic reinforced copper-graphite composites by mechanical alloying and hot isostatic pressing techniques [2.32]. Owing to their advantages of high elastic modulus, thermal and chemical stability, α-Al_2O_3 SCFs can be used as a novel reinforcement in high-temperature structures.

As for SCF cladding, it has always been a constant obstacle in the development of SCF applications ever since SCFs were developed. The reason that full utilization of SCF based high-temperature devices have not been realized is mainly due to the lack of appropriate high-temperature cladding on SCFs. The lack of cladding leads to the unwanted loss in optical signals due to reactions at the sapphire surface or impurities adsorbed onto the fibre surface, causing the higher environmental vulnerability of the SCFs. However, different cladding methods including out-diffusion method [2.33], He^+ implantation [2.34], rod-in-tube method [2.35], have been reported since 1977. With the progress of technology and the discovery of new materials, the cladding problem has been gradually addressed to improve the performance of SCF based devices.

2.5 References to Chapter 2

[2.1] A. Snyder and J. Love, *Optical Waveguide Theory*. London: Chapman and Hall Ltd, 1983, ISBN 978-1-4613-2813-1.

[2.2] R. Paschotta, *Field Guide to Optical Fiber Technology*. Bellingham: RP Photonics, 2010, ISBN: 9780819480903.

[2.3] J. Buck, *Fundamentals of Optical Fibers*, 2nd. ed., Hoboken: Wiley Interscience, 2004, ISBN: 978-0-471-22191-3.

[2.4] P. Sidhar, P. Signal and S. Singla, "Photonic crystal fiber: A review," *Optical and Wireless Technologies*, vol. 472, pp. 230-245, 2018.

[2.5] P. Rudolph and T. Fukuda, "*Fiber Crystal Growth from the Melt*," *Cryst. Res. Technol.*, vol. 34, pp. 3-40, 1999.

[2.6] C. V. Boys, "On the production, properties, and some suggested uses of the finest threads," *Proc. Phys. Soc*., vol. 9, 1887.

[2.7] H. LaBelle and A. Mlavsky, "Growth of sapphire filaments from the melt," *Nature*, vol. 216, pp. 574-575, 1967.

[2.8] H. LaBelle, "Growth of the controlled profile crystals from the melt: Part II – edge-defined film-fed growth," *Mat. Res. Bull*., vol. 6, pp. 581-590,1971.

[2.9] D. Gasson and B. Cockayne, "Oxide crystal growth using gas laser," *J.Mater. Sci*., vol. 5, pp. 100-105, 1970.

[2.10] C. Burrus and J. Stone, "Single-crystal fiber optical devices: A Nd: YAG fiber laser," *Appl. Phys. Lett*., vol. 26, pp. 318-320, 1975

[2.11] M. Fejer, J. Nightingale, G. Magel and R. Byer, "Laser-heated miniature pedestal growth apparatus for single-crystal optical fibres," *Rev. Sci. Ins*., vol 55, pp. 1791-1796, 1984.

[2.12] R. Feigelson, "The laser-heated pedestal growth method: A powerful tool in the search for new high-performance laser crystal," in: *Tuneable Solid-State Lasers*, P. Hammerling, A. Budgor and A. Pinto, Ed. Berlin, vol. 47, pp. 129-142, 1985.

[2.13] L. Tang, "The EFG growth of sapphire single crystals," *Pergamon Journals Ltd*., vol. 11, pp. 351-356, 1985.

[2.14] J. Fitzgibbon and J. Collins, "High-volume production of low-loss sapphire optical fibers by Saphikon EFG (edge-defined, film-fed growth) method," *Proc. SPIE,* vol 3262, pp. 135-141, 1998.

[2.15] M. Fejer, "Single Crystal Fibers: Growth Dynamics and Nonlinear Optical Interactions," *PhD thesis,* Stanford University, 1985.

[2.16] S. Singh and B. Lal, "Laser heated pedestal growth and characterization of the crystalline fibers of KDP doped L-arginine phosphate," *Journal of crystal growth,* vol. 312, pp. 443-446, 2010.

[2.17] C. Nie and J. Harrington, "Single-crystal, rare-earth doped YAG fiber lasers grown by the laserheated pedestal growth technique," Proc. SPIE 8961, Fiber Lasers XI: Technology, Systems, and Applications, 896126 (2014); doi: 10.1117/12.2041769.

[2.18] G. Maxwell, "Advances in single-crystal fibers and thin rods grown by laser heated pedestal growth," *Crystal,* vol. 7, pp. 12, 2017.

[2.19] M. Andreeta, "Automatic diameter control system applied to the laser heated pedestal growth technique," *Material Research,* vol. 6, pp. 107-110, 2002.

[2.20] C. Y. Lo and P. Y. Chen, "Three-dimensional simulation and experiment on micro-floating zone of LHPG with asymmetrical perturbation," J. Cryst. Growth, vol. 362, no. 1, pp. 45–51, 2013.

[2.21] G. A. Bufetova, S. Y. Rusanov, V. F. Seregin, Y. N. Pyrkov, V. A. Kamynin, and V. B.Tsvetkov, "Temperature distribution across the growth zone of sapphire (Al_2O_3) and yttrium-aluminum garnet (YAG) single crystal fibers," J. Cryst. Growth, vol. 433, pp.54–58, 2016.

[2.22] H.C. Seat, "Growth and characterisation of single-crystal fibres for sensing applications," Doctoral dissertation, Dept. Mech. Eng., Gla. Uni., Glasgow, UK, 2001.

[2.23] J. Harrington, "Optical properties of single-crystal sapphire fibers" *App. Opt.*, vol. 36, pp. 5934-5940, 1997.

[2.24] F. Benabid, M. Notcutt, L. Ju and B. Blair, “Birefringence measurements of sapphire test masses for laser interferometer gravitational wave detector,” *Optics Communications*, vol. 167, pp. 7-13, 1999.

[2.25] J. Geusic, “Laser oscillations in nd-doped yttrium aluminum, yttrium gallium and gadolinium garnet” *Applied Physics*, vol 4. pp.182-192, 1964.

[2.26] D. Tang, R. Route and R. Feigelson, “Growth of barium metaborate single crystal fibre by the laser-heated pedestal growth method,” *Journal of Crystal Growth*, vol. 91, pp. 81-89, 1988.

[2.27] F. Wallenberger, “Structural silicate and silica glass fibre” in *Advanced inorganic Fibers: processes, structures, properties, applications,* Dordrecht, Netherlands: Kluwer Academic Publishers, 2000, ch. 6, pp. 159-160.

[2.28] N. Pfeiffenberger, G. Pickrell, and K. Kokal, “Sapphire photonic crystal fibres,” *OE Letter*, vol. 9, pp. 49, 2010.

[2.29] C. Hill, D. Homa, Y. Cheng and G. Pickrell, “Single mode air-clad single crystal sapphire optical fibre,” *Applied sciences*, vol 7, pp. 473, 2015.

[2.30] C. Hill, D. Homa, and G. Pickrell, “Submicron diameter single crystal sapphire optical fibre,” *materials letters*, vol. 138, pp. 71-73, 2015.

[2.31] J. Shu, E. Damiano, and A. Sottile, “Growth by the µ-PD method and visible laser operation of a single-crystal fiber of Pr3+:KY3F10,” *Crystals*, vol. 7, pp. 200-208, 2017.

[2.32] G. Zhang, X. Jiang, Z. Shao, and D. Zhu, “Investigation of the Microstructure and Mechanical Properties of Copper-Graphite Composites Reinforced with Single-Crystal α-Al_2O_3 Fibres by Hot Isostatic Pressing,” *Material*, vol. 11, pp. 982, 2018.

[2.33] C. Burrus and L. Coldren, “Growth of single-crystal sapphire-clad ruby fibres,” *App. Phys. Lett.*, vol. 31, pp. 383-384, 1977.

[2.34] D. Saini, Y. Shimoji, R. Chang, and N. Djeu, “Cladding of a crystal fibre by high-energy ion implantation,” *Opt. Lett.*, vol. 16, pp. 1074-1076, 1991.

[2.35] C. Lo and et al., “Double-clad Cr^{4+}:YAG crystal fiber amplifier,” *Opt Lett*., vol. 30, pp. 129-131, 2005.

Chapter 3 – Introduction to Fibre Optic Sensing

Chapter 3 – Introduction to Fibre Optic Sensing

3.1 Introduction to fibre optic sensing

Optical fibre sensor (OFS) technology is one of the important applications of optical fibre, which has been studied for nearly five decades since the emergence of fibre optic technology in the 1970s and 1980s. As technology has advanced, interest in OFS has been maintained due to its significant contributions to sectors such as military, manufacturing, aerospace, and medicine. Although OFS has tended to find use in niche commercial applications, it has proved its unique advantages over conventional electrical sensors in numerous industrial applications including temperature measurement, strain measurement, chemical sensing and distributed sensing [3.1].

A significant benefit of OFSs is their relatively small size and light weight, which means they can be set in positions that are difficult to reach. This advantage is used in precision applications in the aerospace and auto-industries, where space is limited. Some OFSs can target very small areas in a structure and thus increase the spatial precision of measurement. Besides the size and weight, the material of optical fibres is non-conductive, which means there is no electrical current in the optical fibres in OFSs. This is particularly useful in places that have explosive hazards. Also, since OFSs use optical signals instead of the electrical signals to transmit information, they are immune to electromagnetic interference (EMI) and radio-frequency interference (RFI) [3.1]. Hence, even when there is powerful electronic equipment around OFSs, the performance of OFSs will not be affected. This provides an opportunity for OFSs to work with a guaranteed precision with other electronics side by side. Moreover, the low-power requirement and low-cost components of OFSs make it commercially available for increasing numbers of applications. All these advantages make OFS a technology that can replace conventional electrical sensors in variety of fields. For instance, for temperature sensing, a thermistor is a common electrical temperature sensor that has been widely used in current protection. However, the working temperature of the most thermistors is very limited, usually between -90 °C and 130 °C. In contrast, OFSs can easily achieve temperature measurements up to 800 °C with the most common glass fibres, as the sensing components [3.2]. High-temperature thermocouples, can of course, be used in high-temperature sensing, and can also achieve measuring temperatures up to 800 °C [3.2]. However, once the object temperature exceeds 800 °C, the thermocouple junction can start to corrode, which influences the stability of measurement and shortens the lifetime of the sensor. By contrast, this issue does not exist in OFSs. When applying OFS techniques such as black-body radiation sensors, the temperature can also be measured without direct contact with the surface of the target object and the sensitivity can be higher than thermocouples in such a high-temperature environment [3.2].

The essential principle of OFS is the conversion of measurands such as changes in temperature, strain, pressure, and position into changes of relevant optical variables of the light transmitted in the fibre: intensity, phase, frequency, etc. By studying and defining the relationship between changes in measurand and light properties in this transduction, the changes in light properties can be used to indicate the changes in measurand. Accordingly, OFSs can be used to measure various environmental parameters.

Most OFSs fall into two broad categories: intrinsic sensors and extrinsic sensors. In intrinsic sensors, the sensing procedure takes place entirely within the fibre as the optical signal propagates down the fibre. Since the fibre itself is used for sensing, it is also called “all-fibre” sensing. One benefit of these sensors is the ability to achieve multi-point sensing along the entire length of the fibre. For example, multiple grating-based sensors can get information at very many points along the fibre to measure temperature, pressure, and strain [3.3]. In extrinsic sensors, the fibre is only used for transmitting the light signal to and from the sensing region where the light can couple to the measurand. A significant advantage of extrinsic sensors is that sensors can be placed in positions that may not be accessible otherwise. For instance, a radiation temperature sensor in a jet engine of an aircraft. With the advance in the capabilities and applications of OFSs, the types of OFSs are becoming more and more extensive. Since every each of OFSs has its own special abilities, selecting the right type of sensor should always be based on the application. In the following sections, black-body radiation sensors, Fabry-Perot interferometer sensors, and grating sensors, as the three OFSs within the scope of this thesis will be described in terms of principles, applications and their current place in state-of-the-art engineering.

3.2 Black-Body Radiation Sensors

An ideal blackbody is a theoretical absorber that can absorb all the incident radiation falling upon it without transmitting or reflecting. In this case, the energy of the emitted radiation only depends on its temperature, therefore, black-body radiation sensors are typically used for high-temperature measurements. Just as its name implies, the emitted radiation from a blackbody is called black-body radiation (BBR); it is thermal electromagnetic radiation that has a specific intensity and spectrum, whose only relationship is with the temperature of the blackbody. Since all objects with a temperature over absolute zero (-273.15 °C) emit electromagnetic radiation, which only increases in frequency and intensity as temperature rises, the blackbody model can be utilized to infer temperature from this radiation. When the temperature of a blackbody rises by thermal radiation or by contact, causing it to emit BBR. The re-emitted radiation can then be further transmitted to an optical analytical system through optical fibres. With knowledge of the relationship between thermal radiation and optical parameters, the temperature can be calculated. This relationship is based on Plank's Blackbody Radiation Law [3.4], which describes the spectral energy density of the emitted radiation for a blackbody at a certain wavelength at a specific temperature, given as

$$W_\lambda = \frac{C_1}{\lambda^5}\frac{1}{exp\,(C_2/\lambda T) - 1} \tag{3.1}$$

Where W_λ is the radiant power emitted of per unit area at per unit wavelength; C_1 and C_2 are the first and second radiation constants respectively (C_1 = 3.7418 × 10^{-16} Wm^2, C_2 = 1.43879 × 10^{-2} mK); λ is the wavelength in meters, and T is the temperature of the blackbody in Kelvin.

A typical black-body radiation sensor consists of three parts: a transducer, transmitting fibres, and an optical detecting system, as illustrated in Fig. 3.1. The transducer is a sensing tip of a high-temperature fibre such as a glass or a sapphire fibre; the sensing tip is usually in form of an isothermal cavity that has approximately equal emissivity to a blackbody; therefore, it is also known as blackbody cavity. The function of the blackbody cavity is to convert thermal signals to optical signals by re-emitting the radiation.

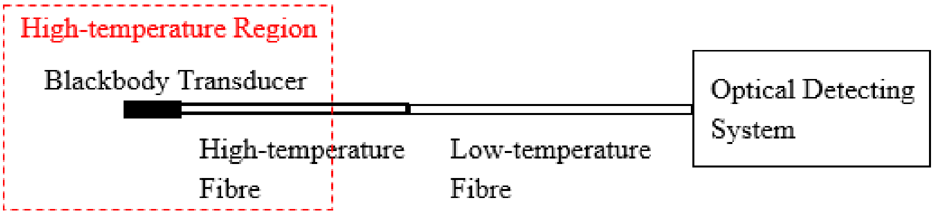

Figure 3.1. Schematic of a typical BBR sensor

In fibre-based sensors, there are basically two main methods to create a blackbody cavity. One is coating the fibre tip with thin ceramic and sintering it at high temperature [3.5]. Another is to sputter a noble metal onto the fibre tip [3.6]. One example of a blackbody cavity is shown in Fig. 3.2. The protective coating in Fig. 3.2 is used to prevent the sensing tip from external damage in the environment and is usually made of aluminium oxide. Once the blackbody cavity generates the optical signal, a transmitting fibre delivers the signal to an optical detecting system. The transmitting fibre usually consists of high- and low-temperature optical fibres; silica glass and sapphire fibres are often used as the high-temperature fibre; normal glass or plastic fibres are often used as low-temperature fibres. The main components of the optical detecting system are lenses, a narrow band filter, and a photodiode. The coupling lens is used to collect and collimate the light and pass it to a narrow filter, where only the light signal at the desired wavelength is passed and signals at other wavelengths are filtered out. Finally, a photodiode converts the optical signal into the electrical signal to then infer the information on measured temperature.

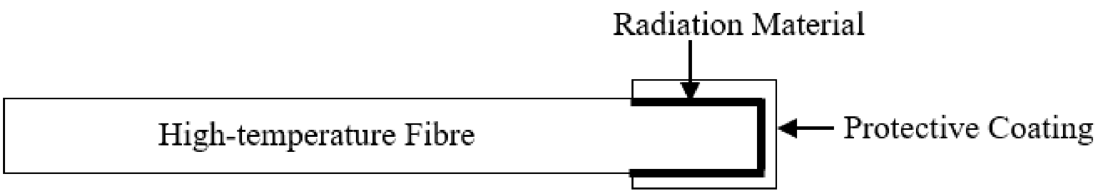

Figure 3.2. Schematic of Blackbody sensor head

Due to excellent thermal stability and high accuracy in high-temperature measurements, BBR sensors have been proven to be very efficient in high-temperature measurement for hot manufacturing processes of materials such as glass, metal and super plastics [3.7]. Their general utilisations in different types of furnace, auto-engines and ovens are beginning to replace traditional electrical temperature sensors. Since BBR sensors detect radiation from heated objects, it needs no optical light source to help sensing and can easily realise non-contact sensing. This distinct advantage makes BBR sensors even more compatible and portable than other OFSs. One example of this is the use of BBR sensors in the thermal control system of microgravity furnaces on the International Space Station [3.6]. However, since the intensity of the thermal radiation is nearly exponentially related to temperature, the intensity is weak at low-temperature ranges, which means that the sensors produce a weaker signal and therefore a poorer performance of low-temperatures compared to high-temperatures. The useful optical measuring temperature range of BBR sensors is estimated to be above 500 °C [3.4]. Thus, BBR sensors are more suitable for high-temperature applications.

Since R. Dils [3.8] used a sapphire fibre as a high-temperature fibre in a BBR sensing system for the first time, sapphire fibres have gradually replaced glass fibres in BBR fibre sensors. In recent decades, sapphire fibres have become an irreplaceable component in the development of BBR sensing due to their high melting point and excellent thermal stability. Due to the high cost of producing blackbody cavities by coating the tip of sapphire with noble metals, the most recent studies are focused on seeking a relatively low-cost material or method to produce a blackbody cavity. Zirconium oxide thin films have been successfully developed and applied for coating the tip of sapphire fibre by sputtering and plasma spraying technology [3.9], this achieved transient high-temperature sensing on the order of microseconds. In reference [3.10], a layer of titanium nitride film is adapted to produce a low-cost blackbody cavity. To find even cheaper metal coating materials, metalized molybdenum and tantalum film have been used in coating the sapphire fibre [3.11]. These studies have further scaled the feasibility and practicality of BBR sensors to broader domains.

3.3 Fabry-Perot Interferometer Sensors

Developed in 1899, the Fabry-Perot interferometer (FPI) has been broadly utilized in lasers, telecommunications and sensors. A typical FPI consists of a pair of semireflecting parallel mirrors and the cavity formed by those two mirrors. Each time the incident light reaches the first mirror, part of the light is reflected back, and part is transmitted through the cavity, reaching the second mirror. At the surface of the second mirror, likewise, part of the light is reflected back towards the first mirror and part of the light is transmitted through the second mirror. This results in several offset beams. These offset beams interfere and produce a basic interferometer [3.12]. The early work on optic fibre FPI sensors was conducted in [3.13]; the results showed that the sensor had 0.5% error in temperature measurement with 150 °C range. Since then, optical fibre FPI sensors have developed rapidly from a single assembled prototype to commercial sensors that can detect extended properties such as temperature, pressure, refractive index, and vibration [3.12].

The principle of an optical fibre FPI is based on the original FPI. Typically, an FPI consists of two parallel reflectors within or external to the basic fibre structure. When the light signal in a fibre is transmitted along to the surface of the first reflector, part of the light is reflected back while the rest is delivered to the surface of the second reflector. At the surface of the second reflector, a part of the light reflects, and the rest is passed to the environment. This results in several reflected light beams interfering with each other and creating an interference pattern. The interference pattern is read and acts as a reference point for sensing the measurand. The variation of the measurand, for instance, temperature, can change the spacing between two reflectors through thermal expansion of reflector material. This variation changes the transmittance of the interferometer, causing a shift in the interference spectrum. By studying the relationship between temperature change and spectrum shift, the optical fibre FPI can be used for temperature sensing. The overall performance of FPI sensor is generally characterised by finesse equation below [3.13], where R is the reflectance of reflectors. An FPI with high finesse has narrow peaks for transmission, which are useful for a high-resolution FPI sensors; an FPI with low finesse will exhibit broad transmission peaks and allow sensors to have linear operations over a boarder range of measurand [3.13].

$$F = \frac{4R}{(1-R)^2} \tag{3.2}$$

According to their configuration, FPI sensors fall into two types: intrinsic and extrinsic. The structure of a typical intrinsic FPI is shown in Fig. 3.3. In Fig 3.3, a length of multimode fibre is spliced between two single-mode fibres. Since the refractive index of the two types of fibre is slightly different, the two splice points between the single-mode and multimode fibres can be regarded as reflectors in an FPI arrangement. In the case of extrinsic FPI sensors, the second mirror is generally placed outside of the transmitting fibre. Fig. 3.4 shows an example of an extrinsic FPI sensor. In this sensor, generally single-mode fibre is inserted into a partially polymer-filled glass capillary, using the fibre tip of SMF and the surface of the polymer as two reflectors [3.14]. To realise dual-parameter sensing, sometimes intrinsic and extrinsic FPIs can be cascaded in one sensing system [3.15], as illustrated in Fig. 3.5. Two reflectors in the intrinsic FPI are produced by micromachining the core of a single-mode fibre with a femtosecond laser; the extrinsic FPI consists of two single-mode fibres and a fused silica capillary tube; the capillary tube is fusion-spliced between two single-mode fibres; one single-mode fibre is cleaved precisely to create a thin diaphragm-sealed cavity; the ends of two fibres act as two reflectors, and a sealed air-cavity is formed between them. In this case, the intrinsic FPI was sensitive to temperature while the extrinsic FPI is sensitive to pressure, therefore realising a dual-parameter sensing technique.

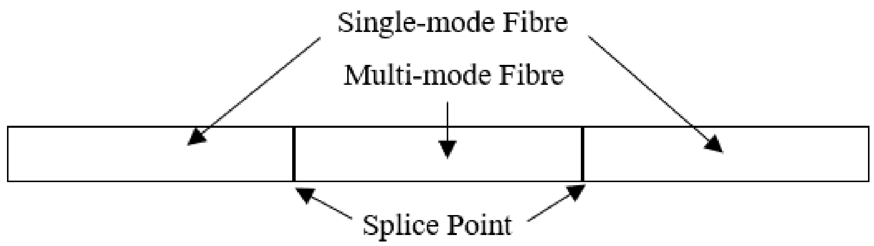

Figure 3.3. Structure of intrinsic FPI

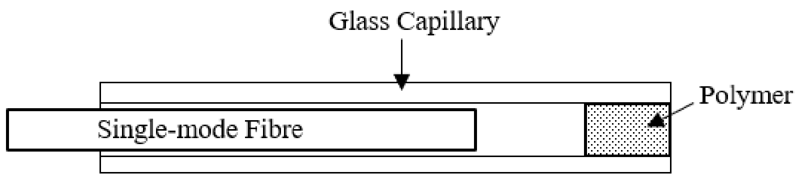

Figure 3.4. Structure of extrinsic FPI

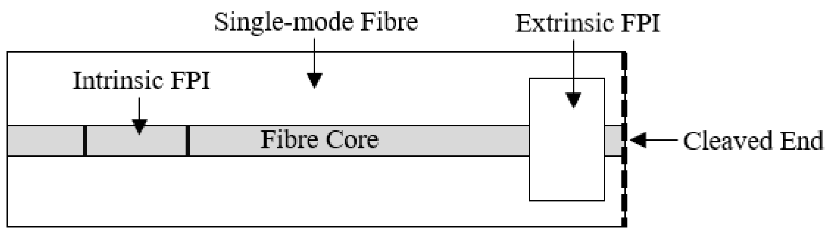

Figure 3.5. Schematic of the cascaded FPI sensor

FPI sensors are of importance as they have many advantages over conventional electrical sensors and some other types of optical sensors. Constant innovations in producing FPI reflectors in conventional fibres have made FPI a common low-cost sensor with inexpensive sensing elements. As a temperature sensor, FPI has very high sensitivity and wide measurement range. Unlike BBR sensors, which only show higher performance in the high-temperature range, FPI sensors have a reliable performance of high-accuracy measurement even from room temperature. This makes it easier than BBR sensors to extend application areas for commercialisation. As a sensor with huge potential, more and more parameters can be measured using FPI sensors. In recent years, an optical fibre FPI for relative humidity sensing is proposed [3.16]. Extrinsic FPI sensors have been successfully used in the continuous measurement of the hematocrit (HCT) level in human blood to provide important information about the patient's health in 2013 [3.17]. FPI has also been utilized not only in the manufacturing industry, but also in other domains such as environmental engineering and medical diagnosis. Another advantage of the FPI sensor is that it can be integrated with other OFSs such as grating sensors to achieve even more functionality. In 2006, an FPI sensor was integrated with a fibre Bragg-grating sensor to achieve simultaneous temperature and strain measurement [3.18]. Utilising its excellent compatibility with other sensing elements, measurement of transverse load [3.19], acceleration and vibration [3.20] can also be achieved.

With the development of crystalline fibre growth techniques, SCFs with their unique properties have started being applied in FPI sensing technology as well. To date, There are two types of SCF-FPI sensor reported: wafer-based and air-based. In 2005, Y. Zhu and his colleagues [3.21] placed a sapphire wafer in front of a sapphire fibre inside an alumina tube connected by some high-temperature adhesive, shown in Fig. 3.6. An LED is used as a light source and projected into a standard silica multi-mode fibre; light transmits through the sapphire fibre which is fusion spliced to the silica fibre at one end and connected to the wafer at the other end. When the ambient temperature rises, both the thickness and refractive index of the wafer increases, changing the interference patterns which encode the temperature information. The sensor was tested to 1600 °C with an error of 0.2% [3.21].

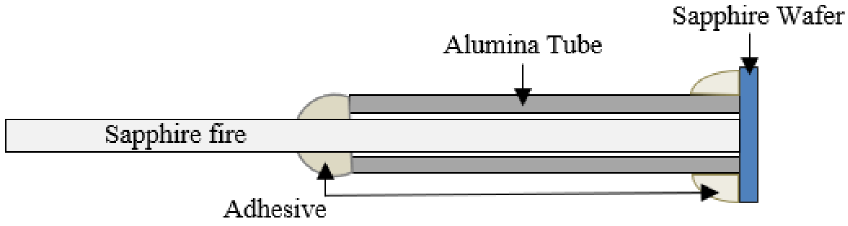

Figure 3.6. Schematic of the sapphire fibre FPI sensor

In 2010, an air gap-based FPI high-temperature sensor was reported in [3.22]. Two sapphire fibres were inserted into a zirconia tube to form an air gap FPI, as illustrated in Fig. 3.7. Ceramic glue was used to bond the fibres and the tube. Both the refractive index of the air in the gap as well as the width of the gap change with temperature rises, resulting an improvement on the sensor sensitivity, compared with the wafer-based sensing method. This air gap-based sensor shows a sensitivity of 20 nm/°C and resolution of 0.3 °C in a temperature range up to 1000 °C. Although these FPI sensing structures are not monolithic in sensing materials, whether wafer-based or air-based, have provided the sapphire fibre FPI sensor with a positive first step. The inherent properties of sapphire fibres such as the large diameter and multimode transmission, provide sapphire fibre FPI sensors with the ability to efficiently couple to low coherence sources such as LEDs. Use of LEDs as an inexpensive, long-operating lifetime light source, cuts down the expense of SCF-FPI sensors.

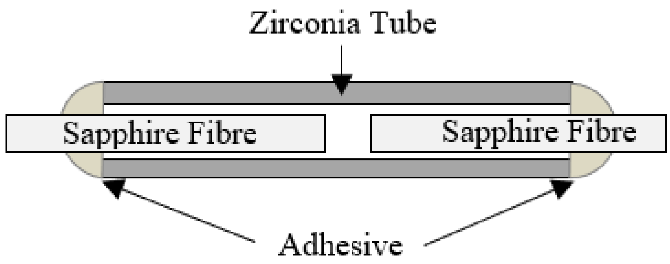

Figure 3.7. Configuration of the air-based FPI sensor

3.4 Grating Sensors

Gratings are the periodic disturbance to the optical (refractive index) or geometrical (waveguide thickness) properties within a fibre. These periodic disturbances change the propagation behaviour of light within fibres. They have made significant contributions in the development and research of optical communication and sensing. The key element of gratings is the regular, periodic modulation of the fibre properties. This can be achieved either by changing the refractive index of fibre core permanently or by deforming the fibre physically [3.23]. Different techniques can be used to modulate the core refractive index of conventional fibres: ultraviolet irradiation [3.24], ion implantation [3.25], irradiation by CO_2 lasers or femtosecond pulses [3.26], and electrical discharges [2.27], to name a few. To deform the fibre physically, the mechanical technique [3.28], the tapering technique [3.29], and the core or cladding deformation technique [3.30] have been reported. According to their period, fibre gratings can be classified into two types: short period fibre gratings or fibre Bragg gratings (FBGs) and long-period fibre gratings (LPFGs).

Typical FBGs have grating periods of a few hundred nanometres. It is the grating which couples light between the forward propagating mode and reverse counter propagating mode at a particular wavelength, which is also known as the Bragg wavelength. The Bragg wavelength reflected by FBG is dependent on the effective index of the propagating mode and grating period. These parameters are influenced by ambient conditions such as pressure, strain, and temperature. Therefore, the change of these parameters can result in the shift of the Bragg wavelength [3.31]. This forms the basis of FBG sensors. The Bragg wavelength λ_B of a grating is given by

$$\lambda_B = 2n\Lambda \tag{3.3}$$

where n is the effective index of the fibre core and Λ is the grating period. An illustration of FBG is shown in Fig. 3.8. When broadband light is transmitted along the fibre, the FBG functions as a filter that only reflects the light at the Bragg wavelength while passing all other light.

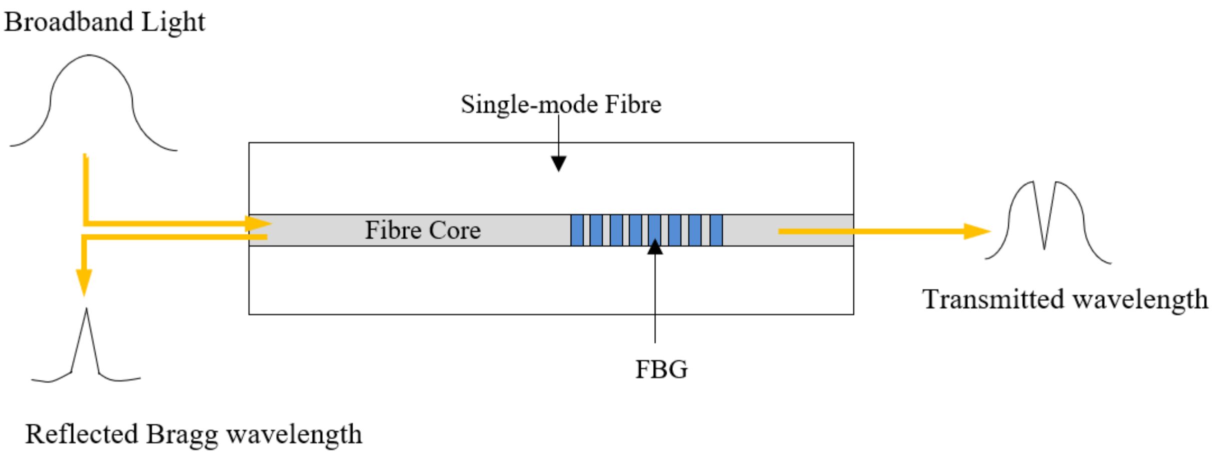

Figure 3.8. Illustration of FBG

In the case of LPFGs, these typically have a period of a few hundred micrometres. LPFG couples light between forward propagating core modes and co-propagating cladding modes at certain wavelengths. The light coupled to the cladding modes quickly decays because of the loss at the interface between the cladding and outer environment; the rest of the light not coupled to cladding modes continues as guided modes. The spectrum of final light received after transmission shows several dips which indicates the loss due to coupling effect of several different cladding modes. Fig. 3.9 shows an example of a transmission spectrum of LPFG [3.23]. The coupling wavelength is called the resonance wavelength λ_R, which is determined by

$$\lambda_R = (n_{core} - n_{clad})\,\Lambda \tag{3.4}$$

where Λ is the grating period, and n_{core} and n_{clad} are the effective index of fibre core and cladding respectively. Since the light signal at the resonant wavelength is lost to the ambient environment through the cladding, and the configuration of the cladding mode is very sensitive to the changes of parameters such as refractive index and temperature, changes of these parameters alter the mode coupling to the cladding modes, leading a shift of the dips in the transmission spectrum.

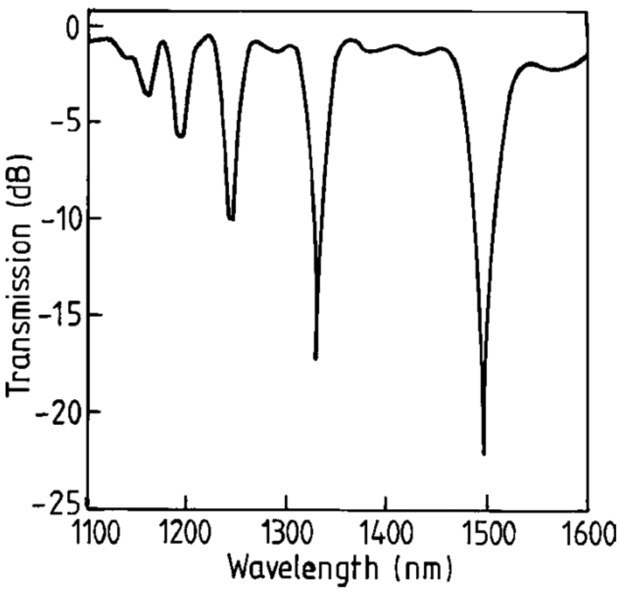

Figure 3.9. Transmission spectrum of LPG [3.23]

Compared with FBG, the coupling to the cladding modes in LPFG can be more sensitive to temperature and refractive index change in the ambient medium. It was reported in [3.31] that the response of LPFG to temperature can be up to seven times stronger than FBG. Comparing FBG and LPFG side by side, it indicates that LPFG possesses a larger temperature coefficient than that of conventional FBG in temperature sensing [3.32]. More importantly, since the period of modulation in the fibre is larger, relatively low-cost fabrication techniques can be employed to produce LPFG, such as etching and precision dicing making it simpler to implement than FBG. With the advantages of lower back reflection, and smaller insertion loss, LPFG becomes a strong candidate for sensing applications. With the advent of innovative grating inscribing techniques and new types of optical fibre, LPFG sensors have also been used to measure humidity [3.33], torsion [3.34], strain [3.35], and an ever-greater number of other measurands. In very recent years, the studies on LPFG are generally focused on increasing the sensitivity in temperature measurements. The sensitivity has been improved from 0.77 nm/ °C to 19.2 nm/ ºC by different techniques including: enhancing LPFG performance by atomic layer deposition technology (reaching to 0.77nm/ ºC in sensitivity) [3.36]; applying a novel cladding structure (achieving a sensitivity of 0.8 nm/ ºC) [3.37]; producing an etched fibre with extremely thin cladding (resulting in a sensitivity of 2.1nm/ ºC) [3.38]; surrounding LPG with a high thermo-optic coefficient liquid (improving sensitivity up to 19.21 nm/ ºC) [3.39].

Entering the 21st century, most developments in LPFG temperature sensing are based on low-temperature applications. As the applications which require high-temperature sensors are increasing, such as improving the efficiency of combustion processes, monitoring super material manufacturing, and measuring the temperature in aero engines, single crystal sapphire fibres have naturally become an attractive choice for development of LPFG high-temperature sensors. However, at this stage, there are no mature fabrication methods such EFG or LHPG to easily produce sapphire fibre sensors. Conventional ultraviolet irradiation methods cannot be used for inscribing gratings in sapphire fibres. Because of its high mechanical strength and strong ionic bonding, it is challenging to produce long-period gratings in sapphire fibres by conventional physical or mechanical techniques. Up to 2004, S. Nam and his colleagues first inscribed LPFG on sapphire fibre by precision dicing with a computer-controlled diamond saw blade. In this paper [3.40], a sapphire fibre, 5 cm in length and 150 µm in diameter was used for grating inscription. Continuous cuts with a period of 150 µm and depth of 50 µm were produced on one side of the sapphire fibre. Since the thickness of the diamond blade was 60 µm, a roughly 50% duty cycle grating could be successfully produced. Although the grating period fabricated is not accurate and these fibres did not have cladding, with the help of index matching oil, the coupling effects of the long-period grating fabricated on sapphire fibre were experimentally observed with reflected specklegram pattern. Although this paper did not prove the LPFG effect directly by its typical spectrum, it has successfully shown the positive possibilities of inscribing long-period gratings on sapphire fibres by precision dicing and laid a solid foundation for follow-up studies.

3.5 References to Chapter 3

[3.1] K. Li, “Review of optical fiber pressure sensor,” in *Conference on Fiber Optic and Laser Sensors and Applications*, 1998, vol. 3541, pp. 217-222.

[3.2] Q. Zheng and K. Torii, “Response of optical fibre thermometer with blackbody cavity sensor,” *JSME International Journal*, vol. 37, pp. 588-595, 1994.

[3.3] A. Tongue, Sensuron (2004), *Extrinsic vs Intrinsic Fiber Optic Sensors* [online]. Available: https://www.sensuron.com/industry-news/extrinsic-vs-intrinsic-fiber-optic-sensors/ [date last accessed: 18/04/19]

[3.4] Y. Yu and W. Chow, “Review on an Advanced High-Temperature Measurement Technology: The Optical Fiber Thermometry,” Journal of Thermodynamics, vol 20, pp. 11-20, 2009.

[3.5] G. Zhao and X. Tong, “research progress and development of sapphire fibre sensor,” *sensors and transducers*, vol. 174, pp. 8-13, 2014.

[3.6] M. Jones and D. Barker, “Use of blackbody optical fiber thermometers in high temperature environment*,” Journal of Thermophysics and Heat Transfer*, vol. 16, pp. 306-322, 2002.

[3.7] A. Ghosh and C. Hamilton, “Superplastic Forming and Diffusion Bonding of Titanium Alloys,” *Sci. J.*, vol. 36, pp. 153-177, 1986.

[3.8] R. Dils, “High-temperature optical fibre thermometer,” *Journal of Applied Physics*, vol 54, pp. 1183-1198, 1982.

[3.9] X. Hao and S. Tao, “Research on characteristic parameter of Ta-Zro2 fiber blackbody cavity temperature sensor,” *International Journal of Signal Processing*, vol. 9, pp. 287-296, 2016.

[3.10] Z. Liu, “Sapphire fiber sensor technology research blackbody cavity formed,” *Inner Mongolia Petrochemical Industry*, vol. 6, pp. 90-94, 2013.

[3.11] X. Hao, “Design of black-body cavity transient high temperature sensor on sapphire fiber,” *Optic Technology Application*, vol. 25, pp. 54-57, 2010.

[3.12] S. Pevec and D. Donlagic. “Miniature all-fiber Fabry-Perot sensor for simultaneous measurement of pressure and temperature,” *Appl. Opt*., vol. 51, pp. 36-45, 2012.

[3.13] E. Udd and W. Spillman, *Fiber Optic Sensors: an introduction for engineers and scientists*, 2nd ed. New York: A Willey-Interscrience Publication, 1991. doi:10.1002/9781118014103.

[3.14] G. Zhang, M. Yang, and M. Wang, "Large temperature sensitivity of fiber-optic extrinsic Fabry-Perot interferometer based on polymer-filled glass capillary," *Opt. Fiber Tech.*, vol. 19, pp. 618–622, 2013.

[3.15] Y. Zhang, J. Huang, X. Lan, L. Yuan, and H. Xiao, "Simultaneous measurement of temperature and pressure with cascaded extrinsic Fabry–Perot interferometer and intrinsic Fabry–Perot interferometer sensors," *Opt. Eng.*, vol. 53, pp. 101-105, 2014.

[3.16] V. Antonio, "Optical fibre humidity sensor based on polyvinylidene fluoride Fabry-Peorot," *IEEE Photonics photonic letters*, vol. 31, pp. 549-552, 2019.

[3.17] P. Wierzba and M. Jedrzejewska, "Optimization of a Fabry-perot sensing Interferometer design for an optical fibre sensor of hematocrit level," *ACTA physica polonic*, vol.124, pp. 586-597, 2013.

[3.18] Y. Rao, "Recent progress in fiber-optic extrinsic Fabry-perot interferometric sensor," *Optical fibre tech.,* vol. 12, pp. 227-237, 2006.

[3.19] M. Manders, P. Matthew and J. Stephen, "Transverse strain response of in-fibre Fabry-perot microcavities," in *23rd International conference on optical fibre sensors*, 2014, vol 9157, pp. 4-8, doi: 10.1117/12.2059615.

[3.20] J. Goicoechea, "Vibration detection using optical fiber sensors," *Journal of sensors*, vol. 2010, pp. 1-6, 2010.

[3.21] Y.Zhu, Z. Huang, F. Shen and A. Wang, "Sapphire-fiber-based white-light interferometric sensor for high-temperature measurements," *Optics letter*, vol. 30, pp. 711-713, 2005.

[3.22] J. Wang, B. Dong, "Multiplexed high temperature sensing with sapphire fiber air gap-based extrinsic Fabry-Perot interferometers," *Optics letters*, vol. 5, pp. 619-621, 2010.

[3.23] L. Madhavan, "Temperature and strain sensitivity of long period grating fiber sensors: review," International Journal of Research in Engineering and Technology, vol. 4, pp. 776-782, 2015.

[3.24] A. Vengsarkar, and P. Lemaire, “Long period fibre gratings as band rejection filters,” *J. Lightwave Technology*, vol. 14, pp. 58-64, 1997.

[3.25] M Fujimaki, “Ion-implantation induced densification in silica-based glass for fabrication of optical fiber gratings,” *Journal of Applied Physics*, vol. 88, pp. 5534-5537, 2000.

[3.26] D. Davis, T. Gaylord, and E. Glytsis, “CO2 laser induced long-period fibre gratings: spectral characteristic, cladding modes and polarisation independence,” *Electron. Lett*., vol. 34, pp. 1416–1417, 1998.

[3.27] G Humbert, “Electric-arc-induced gratings in non-hydrogenated fibres: fabrication and high- temperature characterizations,” J. *Opt. A: Pure Appl. Opt*., vol. 4 pp. 194–198, 2002.

[3.28] P. Sehgal, “A Review on Optical Fiber Long Period Grating, its applications in Optical Communication System,” International Journal of Advanced Research in Computer and Communication Engineering, vol. 4, pp.624-630, 2015.

[3.29] M. Putnam, G. Williams, and E. Friebele, “Fabrication of tapered, strain-gradient chirped fiber Bragg gratings,” *Electron. Lett*., vol. 31, pp. 309-310, 1995.

[3.30] C. Poole, “Two mode fibre spatial-mode converter using periodic core deformation” *Electron. Lett*., vol. 30, pp. 1437–1438, 1994.

[3.31] A. Kersey, M. Davis and H. Patrick, “Fiber grating sensors,” *Journal of Lightwave Technology*, vol. 15, pp. 1442-1463, 1997.

[3.32] V. Bhatia, T. Alberto, “Comparison of optical fiber longperiod and Bragg grating sensors,” in: Smart structure and materials 1996, vol. 2718, pp. 17-23, 1996, doi: 10.1117/12.240853.

[3.33] H. Jiri and H. Nurul, “Simultaneous in situ temperature and relative humidity monitoring in mechanical ventilators using an array of functionalised optical fibre long period grating sensors,” *Sensors and actuators*, vol. 286, pp. 306-314.

[3.34] W. La, C. Lin and G. Chen, “Torsion sensor made of corrugated long period fiber grating,” in:14th international conference on optical fiber senor. Venice, 2000, vol 4185, pp. 640-643.

[3.35] R. Gaspar, F. Rosane and I. Oleg, “Simultaneous temperature and strain measurements performed by a step-changed arc-induced long-period fiber grating,” *Applied optics*, vol. 46, pp. 1392-1396, 2007.

[3.36] F. Zou, Y. Liu, and S. Zhu, “Temperature sensitivity enhancement of the nano-film coated long-period fiber gratings,” *IEEE Sensor Journal*, vol. 16, pp. 2460-2465, 2016.

[3.37] S. Khaliq, S. James and R. Tatam, “Enhanced sensitivity fibre optic long period grating temperature sensor,” *Meas. Sci. Technol.*, vol. 13, no. 5, pp. 792-795, 2002.

[3.38] S. Yin, K. Chung and X. Zhu, “A highly sensitivity long period grating based tuneable filter using a unique double cladding layer structure,” *Opt.Comm*, vol. 188, pp. 301-305, 2001.

[3.39] S. James, S. Khaliq, and R. P. Tatam, “Enhanced sensitivity fibre optic long period grating temperature sensor,” *Meas. Sci. Technol.*, vol. 13, no. 5, pp. 139–142, 2002.

[3.40] S. Nam, C. Zhun, and S. Yin, “Recent advances on fabricating in-fiber gratings in single crystal sapphire fibre,” in: Conference on Photorefractive Fiber and Crystal Devices - Materials, Optical Properties and Applications X, Denver, 2004, pp 147-155.

Chapter 4 – Sapphire Fibre Growth and Analysis

Chapter 4 – Sapphire Fibre Growth and Analysis

4.1 Design and Setup of LHPG

4.1.1 Design of LHPG

The design of the LHPG system in this project was based on the original model that was established at Stanford University [4.1]. The primary consideration of the design was to minimize the diameter variations of the growing fibre for the high-quality crystal fibre fabrication. Additionally, the design also needed to be efficient at growing SCFs and easy to use. To achieve this, the selection and design of the heat source, laser beam guiding optics, pull/feed system, and viewing system, as several parts of the whole system, should require consideration. Since the CO_2 laser is a Class 4 laser, to protect users from laser radiation, the main components of the system were isolated by a polycarbonate laser protection box (opaque to the laser wavelength while allowing visual inspection) and a growth chamber, leaving only the growth controllers outside. The overview design of the LHPG system is schematically shown in Fig. 4.1, which is discussed in the following sections.

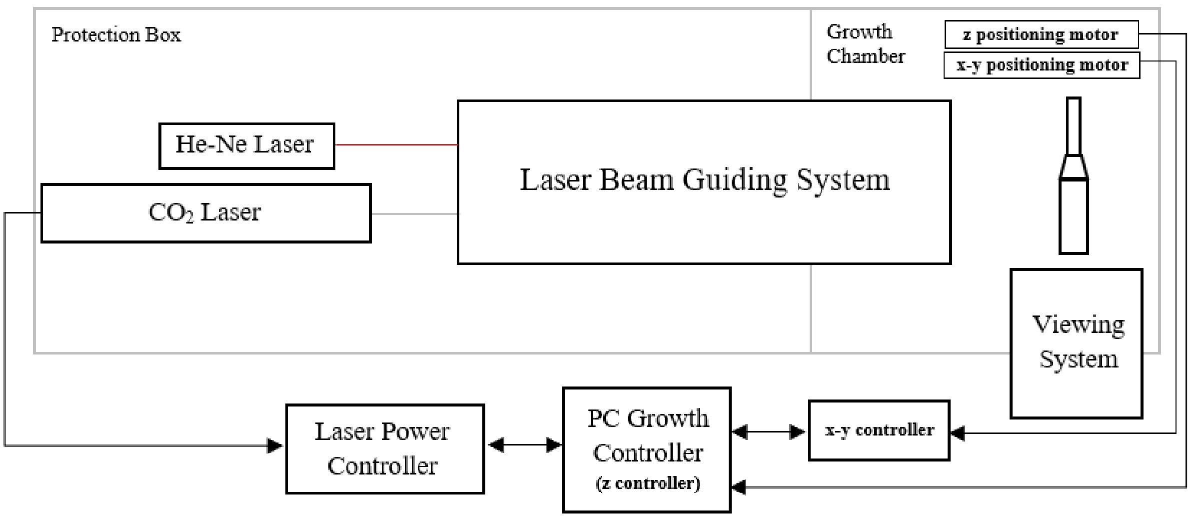

Figure 4.1. Schematic of LHPG system

4.1.2 Heat source

As mentioned above, variations in fibre diameter need to be minimised to produce high-quality crystal fibres; otherwise, the as-grown fibre with variations in diameter can cause significant transmission signal loss due to side-wall surface scattering. It has been reported in [4.1] that the stability of the shape of the molten zone during growth can directly affect variations in diameter of the growing fibre. Since a drop or rise in the heat source power can change the shape of the molten zone by decreasing or increasing the volume of the melt, the stability of the molten zone shape is influenced by the power stability of the heat source. Therefore, to ensure minimal variation in the crystal fibre diameter, a stable heat source with minimum power fluctuation is necessary. A *Synrad Inc*. Series 48-2 CO_2 laser was used as the heat source in this project. This CO_2 laser has a maximum output power of 28 W with "all-metal" tube technology, which means it is a sealed laser with no requirement of an external CO_2 gas supply; also, the laser uses air-cooling instead of a water-cooling method. Compared with water-cooling CO_2 laser, these characteristics of air-cooling CO_2 laser make it a lightweight, compact and jitter-free heat source with several advantages such as high performance, good reliability and long life. A UC-1000 *Synrad Inc*. laser controller was installed to set and stabilise laser output power, which is quoted at ±2 % stability in operation [4.2]. The input current of the laser controller is from 4 to 20 mA, isolated from EMI in the environment, and used as control signal to adjust the laser power precisely. Since the diameter of the source rod is usually as small as 1 mm, even small differences (±1%) in the laser power can strongly influence the fibre diameter (±5%).

4.1.3 Laser beam guiding optics

Since the beam of the CO_2 laser is in the infrared region ($\lambda = 10.6$ μm), this makes it difficult to direct the light path as well as focus the laser beam onto the source rod. Therefore, a low power He-Ne laser with the visible red-light beam at 632 nm wavelength was used as a visual guide for the CO_2 laser. A mirror was positioned in front of the He-Ne laser to direct it towards a beam combiner which allows the CO_2 laser beam and He-Ne laser beam to travel along the same path. As is schematically shown in Fig. 4.2, a set of four gold-coated flat mirrors were used to direct the laser beams to the reflaxicon. The use of the mirrors increases the propagation distance of laser beam, leading to a natural increase of the beam diameter;

the expanded beams are further split by the reflaxicon into a “hollow” Gaussian beam with a ring of uniform intensity distribution; this Gaussian beam is then reflected onto a parabolic mirror by the elliptical turning mirror; at last, the parabolic mirror focuses the beam onto the tip of the source rod to achieve symmetrical heating for fibre growth. All mirrors were highly polished to provide a high-quality, low-loss guiding for laser beams. The photographs of the laser beam guiding optics are shown in Fig 4.3.

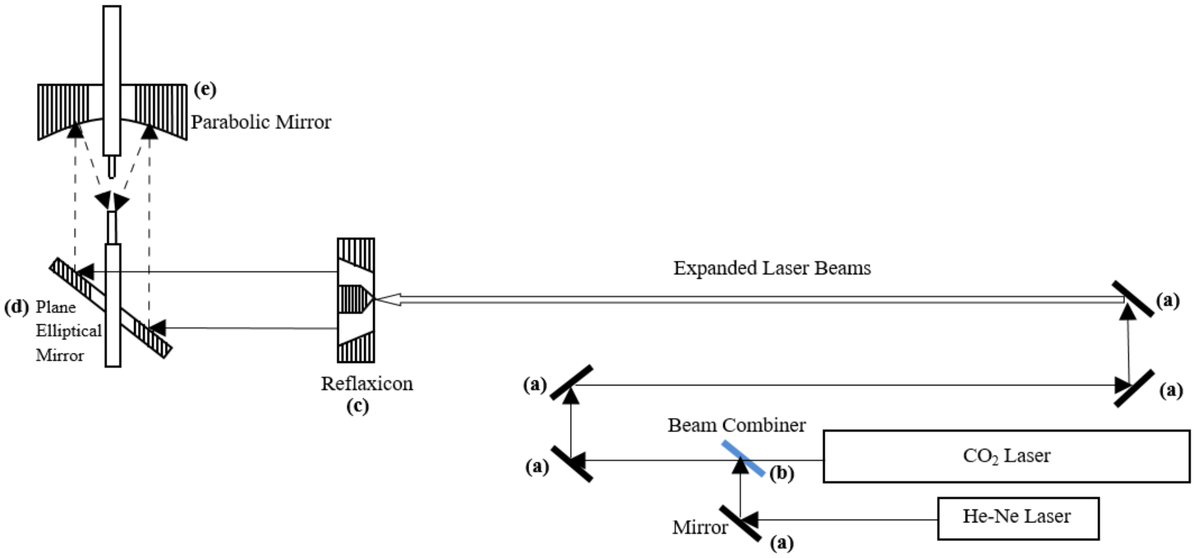

Figure 4.2. Schematic of laser beam guiding optics

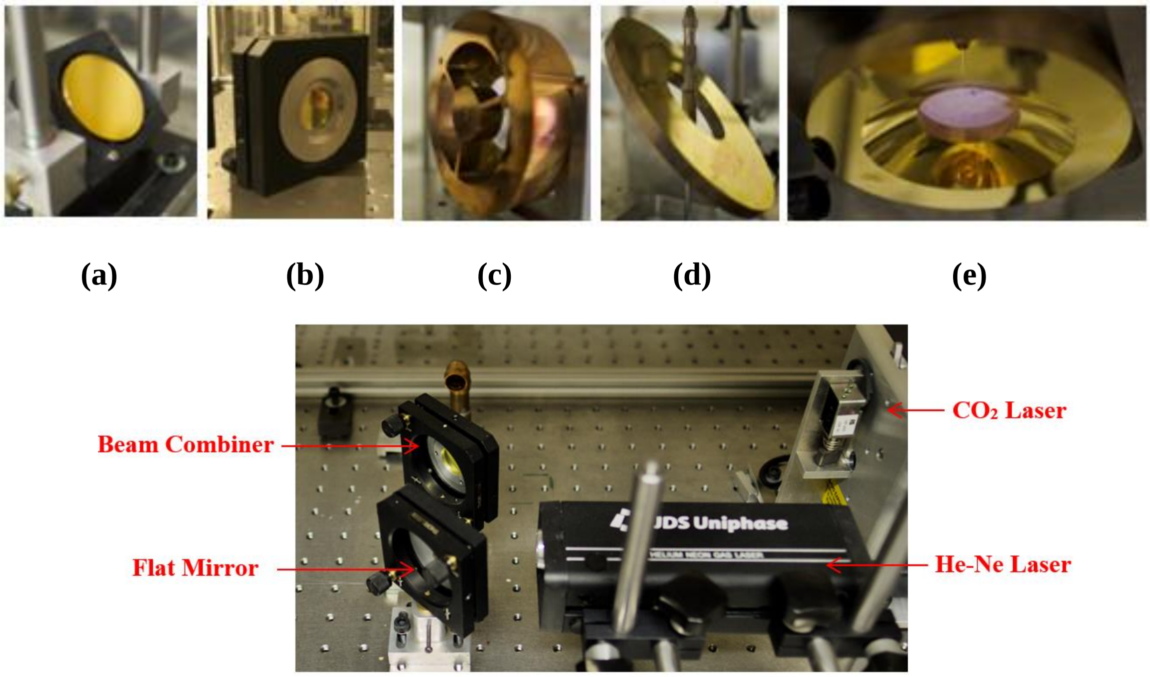

(f)

Figure 4.3. Laser beam guiding optics: (a) flat mirror; (b) beam combiner (c) reflaxicon; (d) elliptical mirror; (e) parabolic mirror; (f) CO_2 and He-Ne lasers.

4.1.4 Pull and feed systems

Since the single-crystal materials have a much lower viscosity in their molten state than glass materials, small external perturbations can adversely influence the stability of the molten zone during growth, resulting in variations in fibre diameter. Therefore, the minimisation of variations in pull/feed rate (less than 1%) is a priority in the design and building of the pull/feed system (fibre pulling from top stage and source material feeding from the bottom stage). A C136 series DC motor from *Physik Instrumente* is used as the pull/feed system driver. This DC motor unit is equipped with a backlash-free gearbox and controlled by a two-channel C842 series motor controller card with a digital PID control on board. Compared with conventional stepper motors, the DC motor can provide accurate steep less speed with constant torque for the growth [4.3]. Due to mass conservation, the pull/feed rates are related to the ratio of source rod diameter and desired fibre diameter [4.4], which is given as

$$\frac{V_{pull}}{V_{feed}} = \left(\frac{D}{d}\right)^2 \tag{4.1}$$

where V_{pull}, V_{feed}, D, and d respectively are fibre pull rate, source rod feed rate, the diameter of the source rod, and the diameter of the desired fibre. Therefore, by selecting a suitable diameter of source rod and choosing the appropriate pull/feed rate, users can specify the desired diameter of the grown fibre. To hold the seed crystal, a small pin chuck with a v-groove was co-linearly aligned and attached to the end of the pull arm. The v-groove provides a straight and vertical alignment for the seed crystal, and the pin chuck holds the seed crystal firmly in the v-groove. To secure the source rod into the feed arm, a small chuck with four miniature retaining elements was screwed onto the end of feed arm. A source rod with a maximum diameter of 1 mm can be held securely by tightening the chuck jaws. The use of small chucks in both pull and feed arms ensures a secure mount for the seed crystal and source rod, providing the basis of straight growth. The assembly of the pull and feed systems are represented in Fig. 4.4.

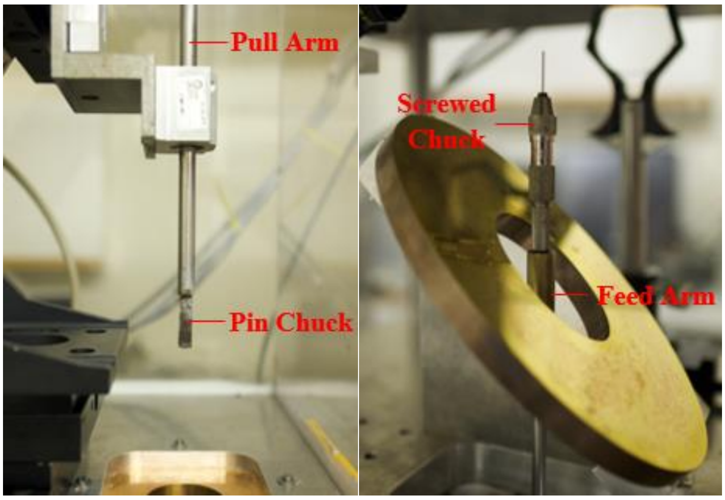

Figure 4.4. Pull and feed system

To align the source rod to the laser focal spot, the x- and y-axes movement of the pull/feed arm are controlled by an external controller and the z-axis motion for fibre growth is controlled by software, programmed in LabVIEW and presented in Fig. 4.5. There are three main parts in this software. The first part is the basic **LHPG growth setting**, where the pull/rate can be set, and the laser power can be manipulated. Various growth options can be chosen from a list to grow various fibre structures including straight fibre, fibre grating, and fibre taper. Once the growth parameters are set, the growth can be initiated by pressing the start button, and the growth information such as elapsed time and length of growing fibre can be viewed. The second part, **LHPG growth option**, is used to set the growth parameters for growing fibre gratings and tapers. For example, by setting grating parameters such as grating type, period, and length, gratings can be grown with the designed size and shape. The last section, **LHPG growth control**, is used to manually control the z-axis movement of the pull/feed arm. This movement was also programmed to be controlled by the keyboard to provide more precise adjustment for initial alignment.

To illustrate the different LHPG growth options, the growth procedure was simulated and plotted in MATLAB based on the growth mechanism of the LHPG. Fig. 4.6 shows the illustration of the grating growth. As it can be seen in the figure, with the growth velocity increases, the radius of the growing fibre decreases, and vice versa. With this periodic change in growth velocity, fibre gratings can be easily fabricated during the growth. The illustrations of the growth of different taper shapes are also shown in Fig. 4.7, Fig. 4.8 and Fig. 4.9. It is necessary to note that these modelling results are the ideal response. In practice, the actual fibre fabricated can vary depending on material, laser power and alignment.

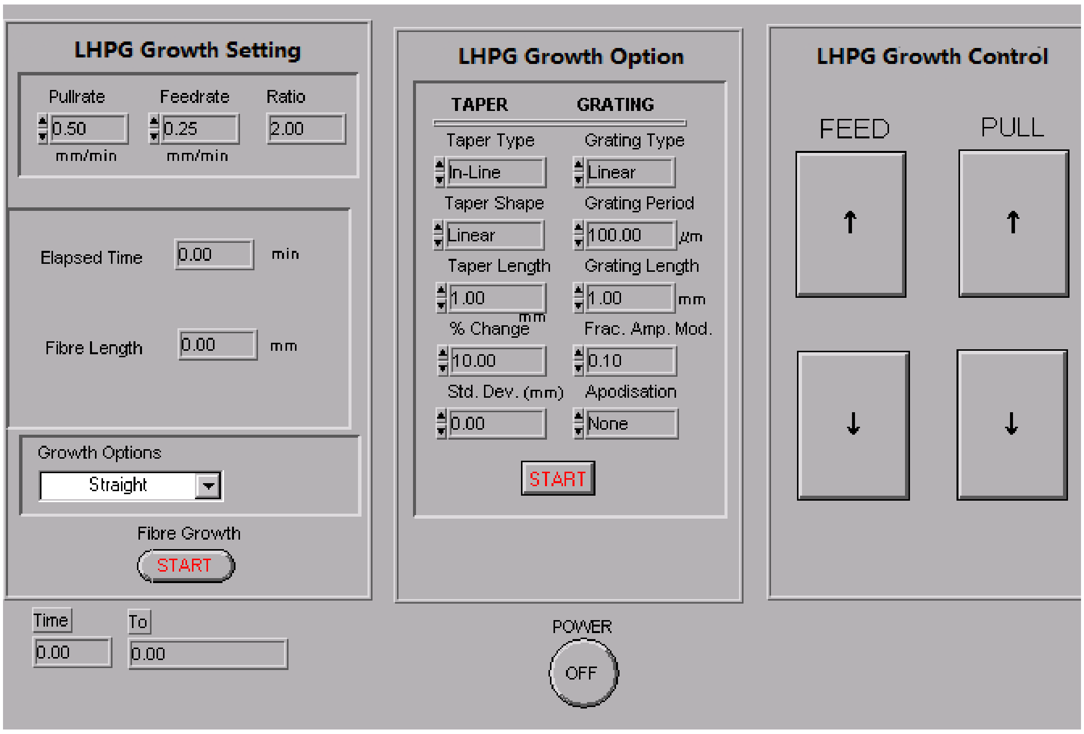

Figure 4.5. LabVIEW software of LHPG

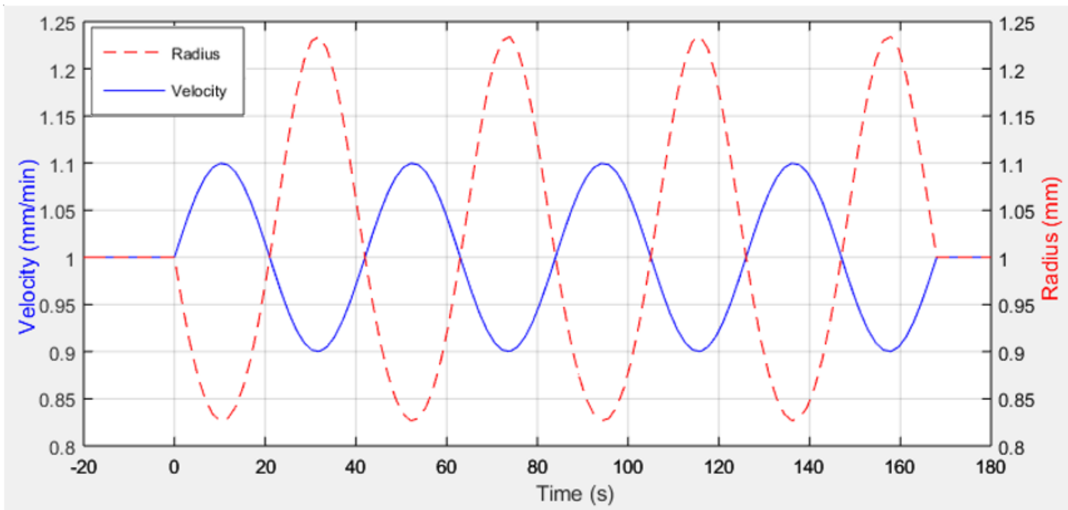

Figure 4.6. Illustration of LHPG grating growth (pull rate = 1 mm/min, initial fibre diameter =1 mm, length of grating = 3 mm, period of grating = 0.7 mm)

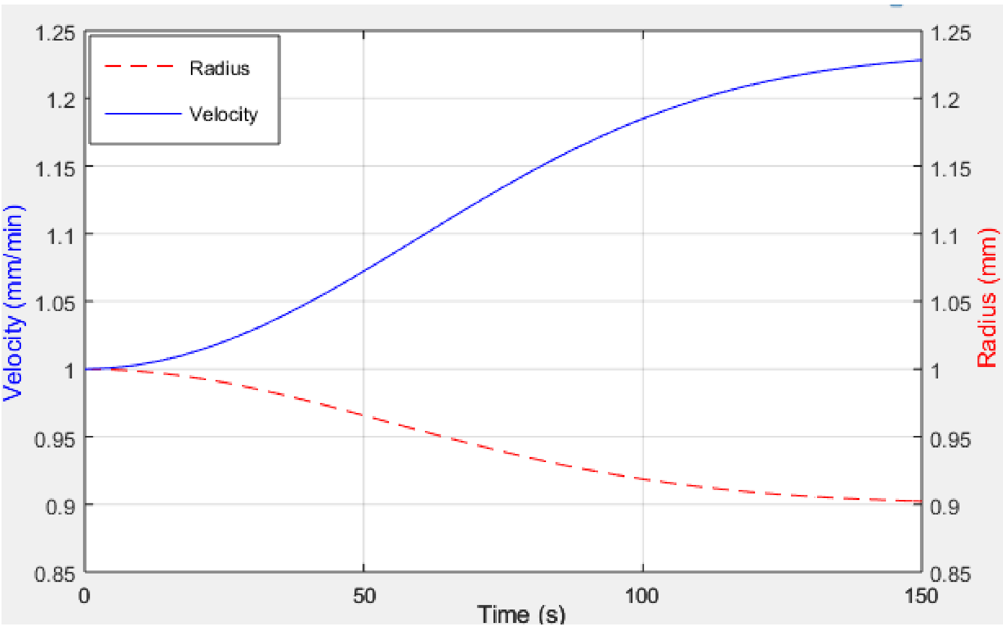

Figure 4.7. Illustration of LHPG Gaussian taper growth (pull rate = 1 mm/min, initial fibre diameter =1 mm, fractional change in diameter = 0.1 mm, taper length = 1 mm, standard deviation = 1 mm)

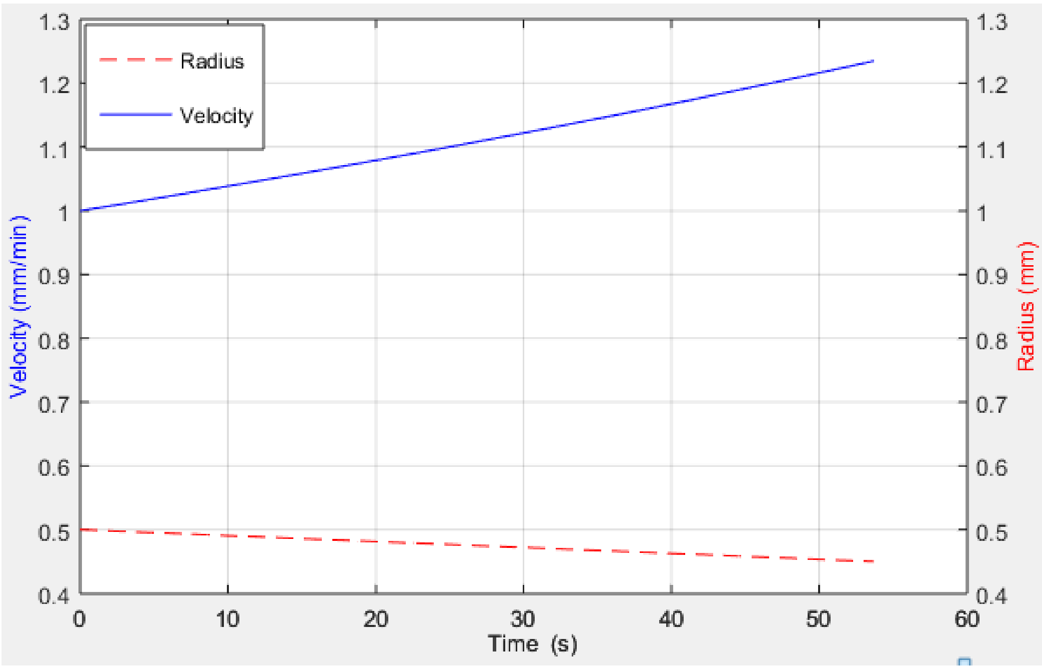

Figure 4.8. Illustration of LHPG linear taper growth (pull rate = 1 mm/min, initial fibre diameter =1 mm, fractional change in diameter = 0.1 mm, taper length = 1 mm)

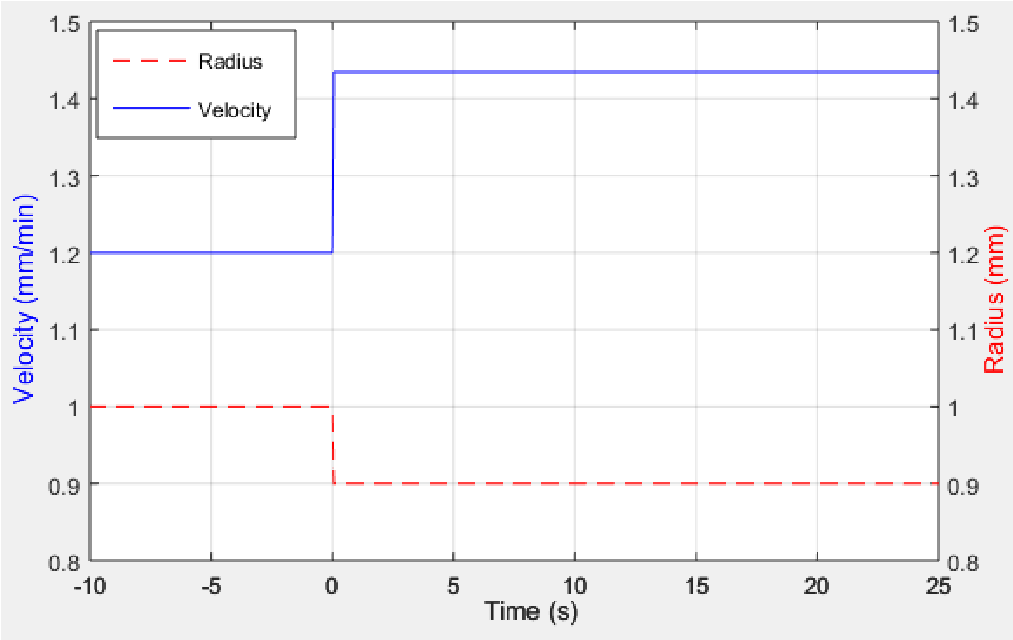

Figure 4.9. Illustration of LHPG step taper growth (pull rate = 1 mm/min, initial fibre diameter =1 mm, fractional change in diameter = 0.1 mm, taper length = 1 mm)

4.1.5 Viewing system

As is schematically shown in Fig. 4.10, a viewing system facilitates multiple functions including initial alignment of the source rod and seed before the growth, monitoring conditions of the molten zone and the growing fibre during growth, and recording the growth process for later studies. In this viewing system, two microscope objective lenses were positioned in the x- and y- directions respectively to get perpendicular views of the growth; two microscope eyepieces were used in each direction to provide the view from the lenses for users to observe; filters were used with the eyepieces to control the brightness of the views and ensure the image was suitable for observation and recording; a beam splitter was positioned between one of the eyepieces and its corresponding lenses to split the image and deliver it to a video camera for recording or monitoring in a computer display. With this viewing system, the CO_2 laser could be aligned co-linearly with the visible He-Ne laser to provide an accurate heating point at the tip of the source rod. Additionally, it allowed users to have fine adjustment of the position of the source rod and seed during growth. The utilisation of this system ensures a good initial positioning of the pull/feed stage and users can also correct errors in positioning that may occur during the growth.

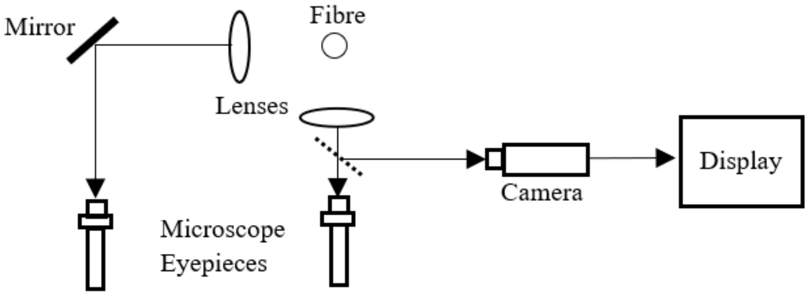

Figure 4.10. Schematic of viewing system (plan view)

4.2 Sapphire Fibre Growth

4.2.1 Preparation of seed and source rod

The seed crystal is the short length of single crystal material used to determine the crystalline structure and orientation of the desired SCF. Since SCFs with different orientations can have different properties, the use of a seed crystal to specify a fixed orientation avoids producing SCFs with unknown or random orientations. As is discussed in **Chapter 2**, there are two major orientations in sapphire fibres, c- and a-axes, each of which has a characteristic cross-sectional shape. As shown in Figure 4.11, the cross section of the c-axis sapphire fibre is round/hexagonal, while the cross section of the a-axis sapphire fibre is an oblong shape with two straight parallel sides [4.3]. For sensing applications, the c-axis sapphire fibre is commonly preferred since it is the optical axis of sapphire and exhibits the lowest birefringence. In this project, an unoriented seed was first used in the initial growth to study and characterise the growth result of the current LHPG method, and the c-axis seed is then prepared to grow sensing elements for optical tests.

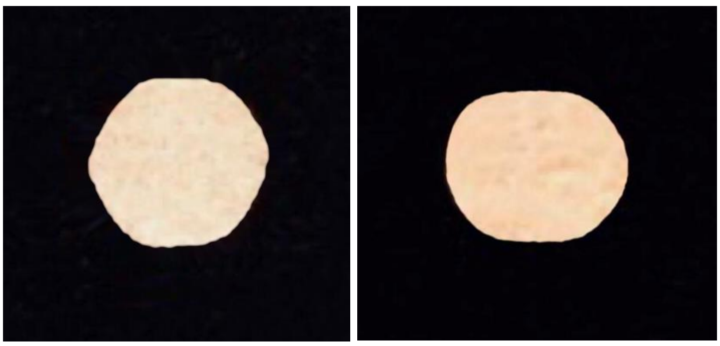

(a) **(b)**

Figure 4.11. Cross sections of c-axis fibre (a) and a-axis fibre (b)

With regards to the preparation of a source rod, three methods were studied, and the performance of each method was tested. The first method was to cold press the aluminium oxide powder with a hydraulic press. The pressed pellet was sintered at high temperature (1100 °C for 3 hours) and then cut to the required dimension (1 mm^2) for growth, shown in Fig. 4.12. Unfortunately, these source rods did not perform well in growth tests. During the growth, many bubbles appeared inside the molten zone and circulated around the melt which adversely influenced the stability of the molten zone, leading to crystal grown with irregular shapes. The appearance of bubbles was due to insufficient source material density, even after sintering. This final density of source rods provided by the cold press technique is not high enough for the LHPG growth of sapphire fibres. Since sapphire has a Mohs hardness of 9, this problem would be expected to be less significant with softer, more compressible source materials.

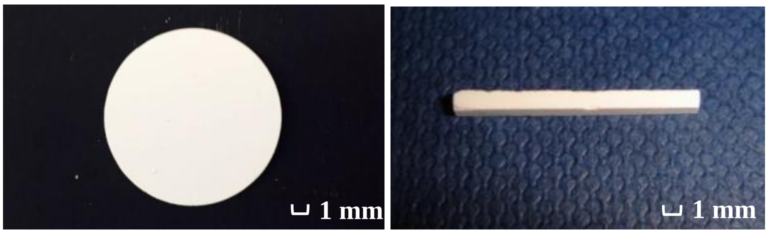

(a) **(b)**

Figure 4.12. Pressed pellet (a) and cut slice (b)

The second method was to use a commercial aluminium oxide ceramic rod directly as the source rod, pictured in Fig. 4.13 (a). For the third method, a single crystal sapphire wafer was used to prepare the source rod, pictured in Fig. 4.13 (b). The aluminium oxide ceramic rod had a diameter of 1 mm which fits the source rod chuck well; however, the sapphire wafer needed to be cut into 1 mm width slices for growth. As is shown in Fig. 4.13 (b) and (c), a 0.5 mm thick sapphire wafer was cut into 1 mm wide rods using a precision diamond saw.

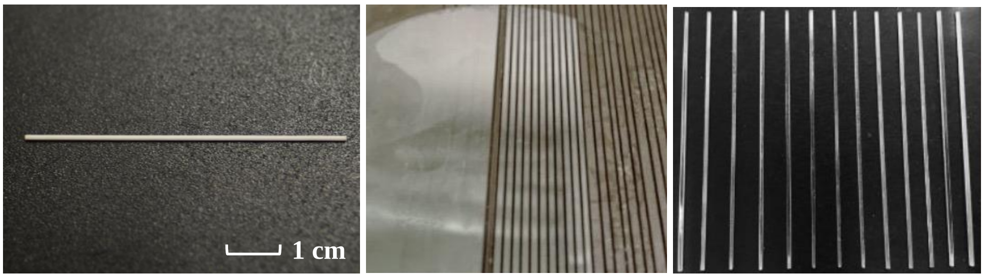

(a) (b) (c)

Figure 4.13. Two methods of preparing source rod: (a) aluminium oxide ceramic rod; (b) cut sapphire wafer; (c) cut sapphire wafer slices.

Comparison of the crystal fibres grown by two different source rods can be seen in Fig. 4.14, the sapphire wafer slice shows distinct advantages over the aluminium oxide ceramic rod as a source rod. The fibre grown from the aluminium oxide rod exhibits a strong coloration of grey and orange, while those grown from the sapphire wafer slice are transparent and pure. The surface of the fibre grown from the aluminium oxide rod has some irregular "rough" structures. By contrast, the fibre grown from the sapphire wafer has a smoother and cleaner surface. The reason for the result in Fig. 4.14 (a) almost certainly arises from the impurities in the aluminium oxide ceramic rod, which were incorporated into the fibre during growth, leading to colouration and the uneven surface. Therefore, the sapphire wafer slice, as the best source rod material among the three, was selected to produce sensing elements.

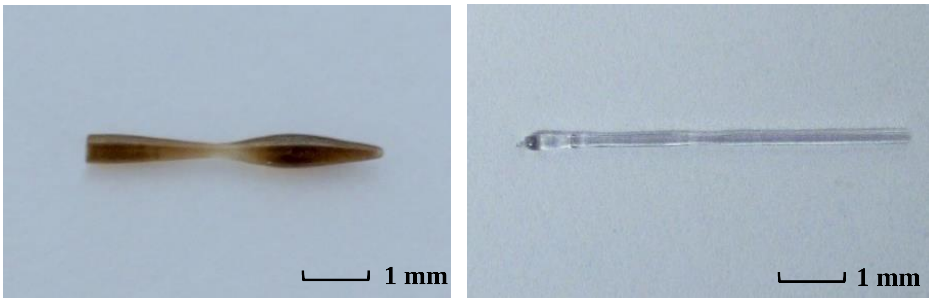

(a) **(b)**

Figure 4.14. Comparison of the fibres grown by two methods: (a) ceramic rod method; (b) sapphire wafer slice method.

4.2.2 Sapphire fibre LHPG

In this section, the LHPG procedural process of sapphire fibre growth is described. Although LHPG can grow many different materials, the basic process remains the same. As discussed previously, sapphire wafers were selected for use as the source material. Initially, an unoriented sapphire fibre was used as the seed crystal to grow fibres and test the performance of the system. The seed crystal and the source rod were firmly secured into the chucks on the pull and feed arms separately; the seed crystal and the source rod were aligned straight and parallel with reference to the vertical pull/feed arms; with the aid of the viewing system, the He-Ne laser beam was aligned on the tip of the source rod by adjusting the fibre positioning remote controller for x-y axis movement, and the LabVIEW software for z-axis movement. Once alignment using the He-Ne was complete, the power of the CO_2 laser was increased to melt the tip of the source rod until a molten zone was formed; with the molten zone formed, the alignment could be re-checked and adjusted to achieve the most symmetric molten zone; after that, with increasing laser power, a bright spot was evident on the top of the molten zone, which indicated the hottest point of the melt; by controlling the pull arm, the seed crystal was axially aligned with the source rod and then dipped into the molten zone (shown in Fig. 4.15); when the seed penetrated the melt, the seed crystal and molten zone were attached and settled; the growth was then initiated by setting the LabVIEW software in terms of pull/feed rate, desired shape of fibre, etc. During the growth process, fine adjustment on the CO_2 power and the pull/feed positions could be made to maintain steady-state growth; if the molten zone volume is decreasing during growth, CO_2 laser power could be risen, and if the shape of molten zone is asymmetrical, pull/feed position could be adjusted for a better alignment; while the growing fibre was uniform and straight, continuous growth was conducted to grow the fibre; when the desired length of fibre was achieved, the growth was stopped in the software and the pull arm was lifted to separate from the molten zone; the power of the CO_2 laser was then reduced to zero and turned off, leaving the cooling fan on for 30 min; finally, the grown fibre with the original seed was taken out from the pin chuck, the seed was then separated from the grown fibre with a diamond scribe and saved for the next growth, while the length of grown sapphire fibre was taken for the use in subsequent tests.

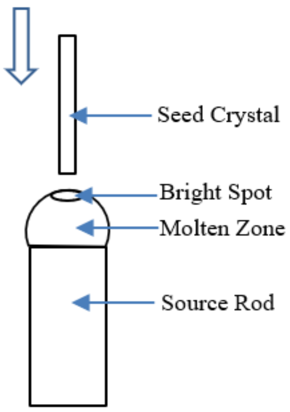

Figure 4.15. Schematic of seed, source rod and molten zone

4.2.3 Follow-up processes

To allow light coupling into the sapphire fibres for optical testing, the two ends of the grown fibre had to be polished. The prepared sapphire fibre was co-linearly aligned with the longitudinal axis of a length of glass capillary and secured into the capillary with the help of quartz wax; the capillary was then secured in an adapted jig which allowed multiple crystal fibres to be polished at same time; finally, the adapted jig was fixed onto an *Ultra Tec* polishing machine to start the polishing process. To initially cut down the sapphire materials so that the ends of the glass capillary and sapphire fibre were at the same level, a SiC grinding pad with 1200 grit was first applied for polishing; then the sapphire fibre was polished with the capillary by different Al_2O_3 polishing pads in the order of 30 µm, 12 µm, 3 µm, and 1 µm. Also, diamond paste/oil was available for fine finishing. The two fibre ends were polished parallel with the help of the gradienter of the polishing machine. Once the process was finished, the wax in the capillary tube was melted on a hot plate and the polished sapphire fibre was removed with tweezers; the fibre was then put in a test tube filled with acetone and cleaned in an ultrasonic cleaner. The polished and cleaned sapphire fibres were then ready for measurement. Fig. 4.16 shows the components used in the polishing process. A high precision digital calliper was used to measure the diameter and length of the sapphire fibre. The diameter of the fibre was measured 7-10 times at different points along the fibre, and the mean value of the measured diameter was calculated as the final value. As was discussed in the previous section, some issues can appear during growth which sometimes produce miniature structures on the as-grown fibres such as bumps, a length of fibre grown at an angle, etc. Therefore, to identify the size and angle of miniature structures on the sapphire fibre, a high-power Nomarski optical microscope from *Leica Microsystems* was used for inspection in a clean room located in the *James Watt Nanofabrication Center*.

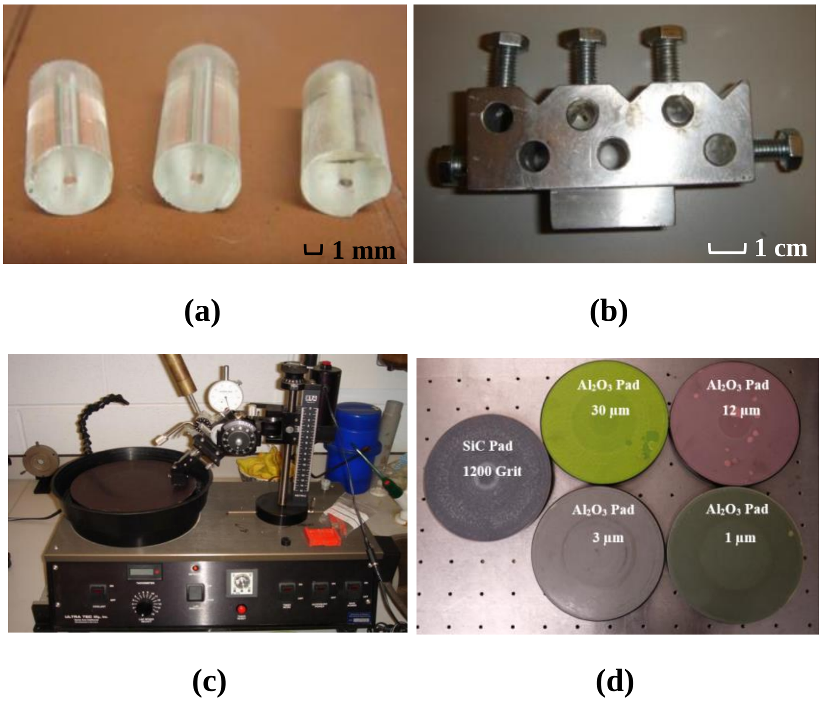

Figure 4.16. Components used in polishing process: (a) glass capillary tube; (2) adapted jig; (3) polishing machine; (3) polishing pad.

4.3 Issues analysis and performance improvement

4.3.1 Growth issues

In accordance with the above steps, several batches of sapphire fibres were grown. Two main issues arose during the growth process, which indicated problems in different parts of the system. The first issue was that the diameter of the growing fibre changed during the growth; this usually happened after a short period of steady-state growth; the diameter of growing fibre suddenly started increasing for a short length of time and then decreased to its previous diameter, producing a “bump” structure on the grown fibre, as illustrated in Fig. 4.17.

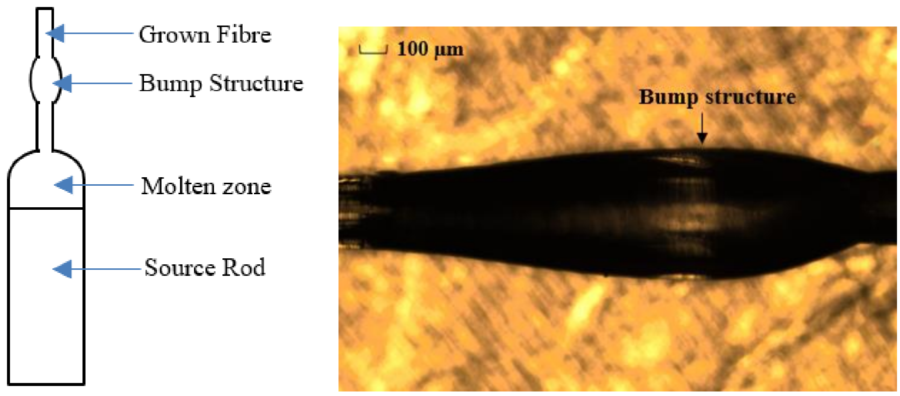

(a) **(b)**

Figure 4.17. Bump structure: (a) schematic; (b) microscope image

The reason for this issue may arise from the fluctuations in the CO_2 power as a change of the molten zone brightness was seen sometimes during the growth. To test the cause, a laser power testing system was built to study the stability of output power of the CO_2 laser, as shown in Fig. 4.18. In this system, a *Coherent Inc.* model 3949 high power thermopile sensor was put in front of the CO_2 laser to receive the laser beam; a *Coherent* model 201 power meter was connected to the thermopile sensor to measure the laser power; the result was then transmitted to a computer and plotted in a graph of power versus time using LabVIEW. As the laser power setting of normal sapphire fibre growth is between 25% to 30% on the laser controller, in this stability test, the laser power was first set to 25% for a 1-hour stability test. Then the power was raised to 30% for 1.5 hours. The result of this test is shown in Fig. 4.19.

It can be seen in the first hour (power setting = 25%), the power fluctuated in the first 40 mins with appearance of several peaks and valleys ranging from 5.5 W to 6.5 W, which disappeared after 40 mins and the laser power became stable. The residual noise on the graph is originated from the power testing system itself. When the laser power was raised from 25% to 30%, the power fluctuated strongly for 40 mins, as seen in the five periodic fluctuations from 6 W to 8 W with each time period of approximately 8 mins. 40 mins after raising to 30% power, the fluctuation disappeared, and the power curve became stable.

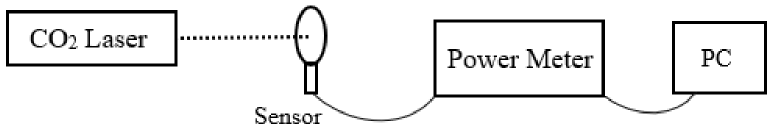

Figure 4.18. CO_2 laser power testing system

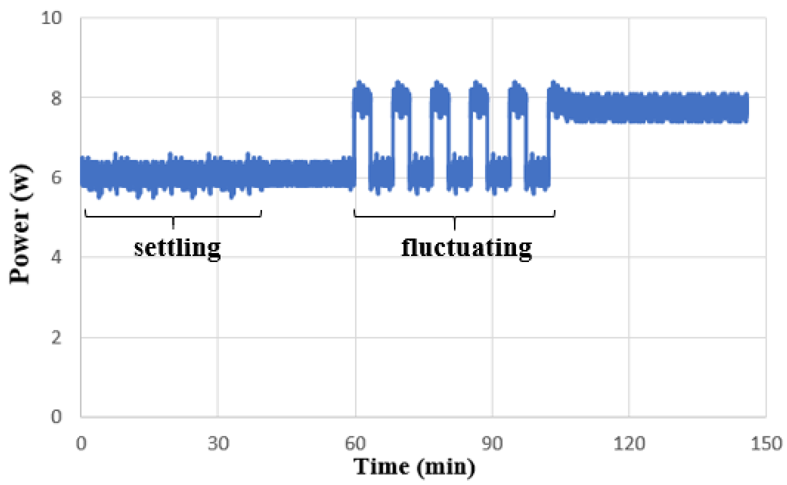

Figure 4.19. Result of the CO_2 laser power test

To further verify if the transient bump structure on the fibre was caused by the fluctuations in the laser power, two steps were added to the growth procedure according to the test result above. Firstly, a warm-up process was added prior to growth, which was further extended and divided into two parts. Part one, a 40 mins warm-up was processed when the desired molten zone is formed after the initial alignment with the CO_2 laser; and then, when the seed penetrates the molten zone and was combined with the melted source rod, 10 mins settling delay was used to stabilise any undulation in the melt. Part two: when the laser power needs to be changed between growths, 40 mins delay was added with the desired power before another growth. As a result, several groups of sapphire fibre growth with the warm-up and delay processes indicated that the fibres showed no obvious sign of diameter change or transient bump structures. Therefore, a stable laser power was found to be essential for successful growth of straight fibre, and relatively small fluctuations (±1%) in laser power can lead to a change in fibre diameter (±5%, or ±15 μm for a 300 μm fibre).

The second issue was that the molten zone could become asymmetric during growth, as illustrated in Fig. 4.20. This issue became more obvious at higher laser powers and as the molten zone size grew larger. The asymmetric molten zone caused deformity in the grown fibre, irregular shape of fibre edges, and eventually, it leads to the lack of molten material on one side of the fibre, causing a break. In addition, the asymmetric molten zone was seen to cause random changes in the shape, diameter, or roughness of the growing fibre. Thus, it had to be eliminated.

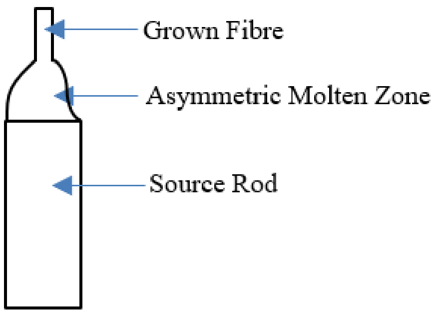

(a) **(b)**

Figure 4.20. Asymmetric molten zone: (a) schematic; (b) photo from viewing system.

Since the source rods were homogeneous and uniform, it was inferred that the asymmetric molten zone must due to asymmetric heating from the CO_2 laser: if the CO_2 laser beam is not symmetric, the distribution of laser power on the source rod will not be symmetric and uniform, which results in more material being melted on one side of the source material than the other, leading to the asymmetric molten zone observed. The cause of asymmetric heating was traced back to the misalignment of the laser guiding optics. As the reflaxicon, elliptical mirror and parabolic mirror were fixed in the growth chamber, the cause was found to come from misalignment of the beam steering mirrors and the beam splitter. Since the transmission distance of laser beams was enlarged to allow for natural divergence to expand the laser beam, even a slight change in the position and angle of any mirrors or the splitter due to mechanical creep can be amplified and finally cause the asymmetric distribution of laser beams.

Therefore, the alignment of these components was redone precisely starting from the first mirror. To ensure the accuracy of the results, the burn marks of the CO_2 laser from the reflaxicon were created before and after alignment, shown in Fig. 4.21 (a) and (b). It is necessary to note that the ideal burn mark at this point should have been a ring shape of equal intensity distribution. The gaps between burn marks are due to the existence of the pull arm and the interior supports of the reflaxicon assembly, which does not influence normal growth. By comparing the two burn marks, it can be found that the burn mark before alignment showed poorer quality in both shape and distribution, while the burn mark after alignment was more uniform and balanced. With the improved alignment of the laser beam guiding optics, the molten zone on the source rod was tested again and the result was improved as an optimised molten zone with a symmetric and uniform shape had been formed, as presented in Fig. 4.21 (c). In subsequent growth tests, the problems related was eliminated by initiating the growth with a symmetric molten zone. Thus, in LHPG, not only the instability of the laser power, the misalignment of the laser beam guiding optics and pointing stability of the laser could also influence the quality of grown fibres.

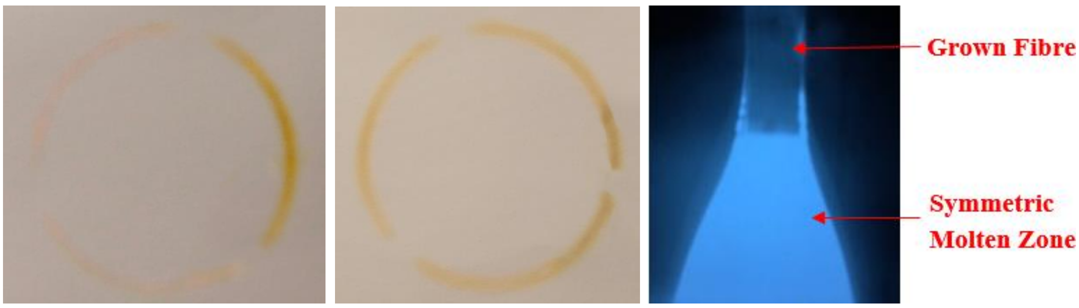

(a) (b) (c)

Figure 4.21. Improved alignment: (a) burn mark before alignment; (b) burn mark after alignment; (c) photo from viewing system after alignment.

4.3.2 Striations issue

Generally speaking, errors caused by the above issues on the appearance of sapphire fibres are irregular and random. However, some relatively regular features on the grown fibre were also observed at times. These features were in the form of striations along the crystal fibre. The striations are streaks or stripes with a regular period, schematically shown in Fig. 4.22. Since one potential sapphire fibre sensor in this project is a grating-based sensor, the striations could have a significant influence on the sensor performance due to the existence of striations with a similar period as gratings. Therefore, the origin of the striations was investigated and discussed.

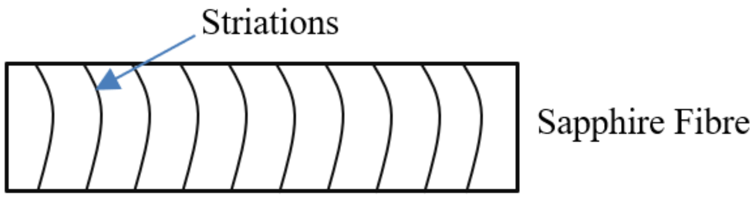

Figure 4.22. Schematic of striations on a length of sapphire fibre

In Fig. 4.23, striations on a sapphire fibre grown from an unoriented seed are pictured from different angles with the microscope. In picture 4.23 (a), striations on the sapphire fibre are shown. It can be seen clearly that the striations are in the form of bright streaks and recur in a regular period of 150 μm (mean value). To view the influence of striations on the edge of the fibre, the fibre was turned to different angles to get a clear view of the edges, and the best image is shown in picture 4.23 (b). It can be seen in picture 4.23 (b) that the lower edge of the fibre was relatively flat, while the upper edge had a regular corrugated outline; in the enlarged picture, it can be seen that the corrugated outline of the upper edge consisted of two sides, one is shorter and the other is longer. However, this sequence of the outline did not exist on the lower edge in any direction. To have a clearer view of the corrugated edge, the upper edge was positioned with its front side up and inspected, pictured in 4.23 (c). From this view, the corrugated outline looks like a sequence of periodic “grooves”, which have a regular trapezoidal surface.

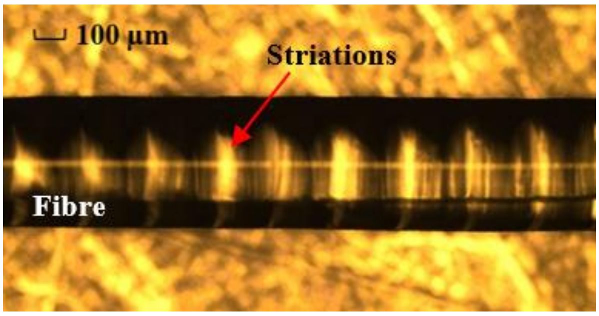

Figure 4.23. (a) striations on sapphire fibre

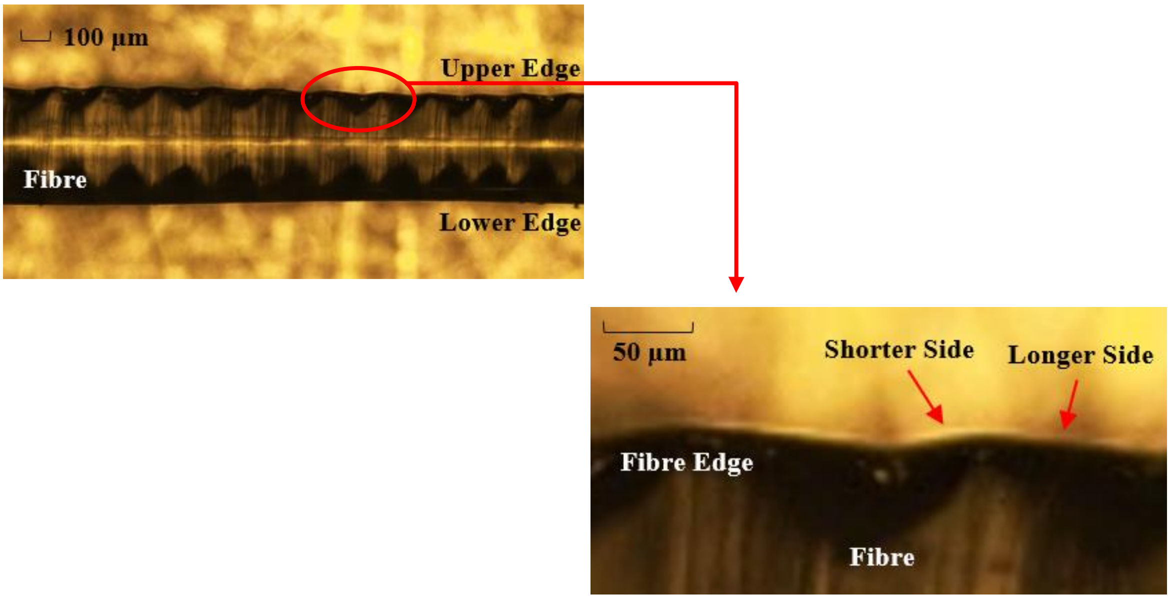

Figure 4.23. (b) striation edges along sapphire fibre

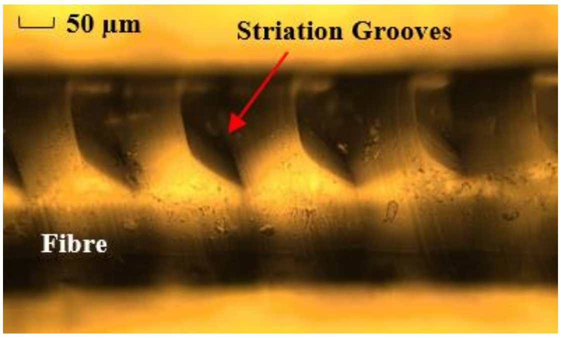

Figure 4.23. (c) corrugated edges of striations

The three possible causes of striations were taken into consideration: the periodic power fluctuations of the CO_2 laser, the periodic vibration in the pull/feed system or from the environment, and the faceting effect. As is reported in [4.5], poor stability of the heating laser and molten zone can lead to rough growth ridges, presented in Fig. 4.24. The striations could also have been caused by the periodic vibrations from the pull/feed system or the surrounding environment, for example, the vibration from the cooling fan of the CO_2 laser.

Besides, these striations could have been the result of the faceting effect, which is a common effect in SCF growth [4.5, 4.6, 4.7]. Unlike the rough ridges in Fig. 4.24, the striations on the grown fibres in the lab were clear, regular, and periodic, strongly consistent with the results of the latest research on SCF faceting [4.8]. Therefore, the faceting effect was regarded as the first potential cause of the striations to be studied.

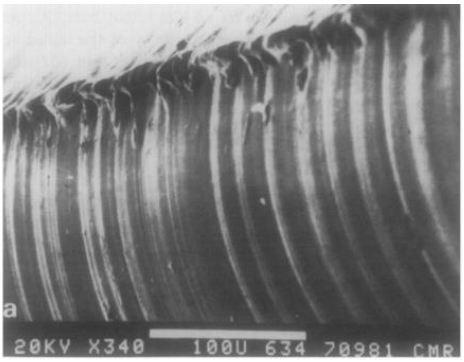

Figure 4.24. Rough ridges on sapphire fibres due to poor heating stability [4.5]

The faceting effect in SCF growth is natural, and its appearance on SCFs has been studied repeatedly for different conditions and growth techniques including LHPG and EFG [4.9, 4.10]. Various explanations have been made for the SCF faceting effect: (1) misalignment of seed [4.11]; (2) the impact of an inaccurate shaper in the EFG method [4.12]; (3) unstable heating power and pull/feed rate [4.13]. The faceting effect has also been found in different single-crystal materials: (1) the facets with a period of approximately 8 µm have been commonly found in YAG crystal fibre [4.7]; (2) the facets in the shape of the cylindrical core region have been observed in garnet crystal [4.14]; (3) the appearance of facets on sapphire fibres during LHPG growth has been reported in [4.8]. The relationship between the period of facets and the diameter of their crystal fibres were also studied in [4.5, 4.7, 4.8], reaching the conclusion that facets only form in the larger diameter fibres (more than 300 µm).

The structures and causes of facets on sapphire fibres are complicated due to the unique uniaxial structure of the sapphire crystal; however, in the latest research, it has been found that the occurrence of faceting in sapphire fibres depends on the direction of the seed crystal [4.8]. It is worth noting that the diameter of the sapphire fibres studied in [4.8] is in the range of 400 to 800 µm. In this research, a precisely orientated c-axis seed was firstly used to grow the sapphire fibres by the LHPG method, providing successful growth of sapphire fibres without noticeable faceting on the fibre surface; then a seed crystal with a misalignment angle (7°) relative to the c-axis direction was used to grow sapphire fibres, resulting the appearance of a sequence of facets in the shape of a “sawtooth” or “notches” only on one edge of the lateral surface. The facets have two sides, a shorter rounded forward side and a longer flat end side. Compared with the groove-like striations grown from an unoriented seed in the lab, distinct similarities could be found in the aspect of shape and outline, shown in Fig. 4.25.

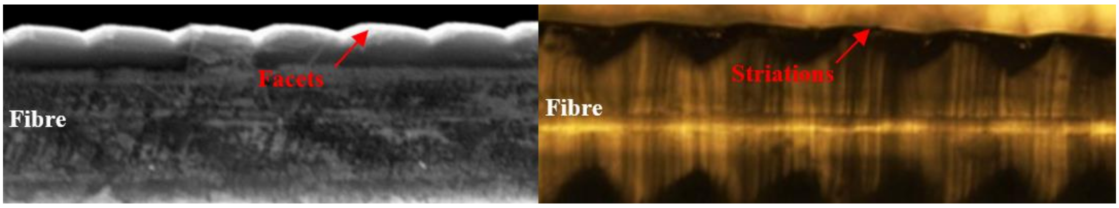

(a) **(b)**

Figure 4.25. (a) facets in [4.8]; (b) striations in this project.

Therefore, the striations observed on the sapphire fibre grown in the lab are mostly like to be the same as the facets in the paper due to the similarity of structure [4.8]. To validate this hypothesis, a c-axis sapphire fibre was used as the seed crystal to grow sapphire fibres and test if there was an absence of striations. The growth was conducted with the same source rod, CO_2 power and pull/feed rate as the previous growth, the only difference being the seed orientation. Unlike the sapphire grown from the unoriented seed, the fibre grown from the c-axis seed had a smooth outline, and no observable striations along the fibre were found even when it was viewed from different angles. This indicates that the appearance of striations on sapphire fibres depends on the orientation of the seed.

To reproduce and verify the results, a few tests were carried out. Instead of c-axis sapphire fibre, a c-axis sapphire wafer slice was used as a seed to produce sapphire fibres; this sapphire slice was cut from a sapphire wafer in the c-axis direction, as illustrated in Fig. 4.26 (a); the fibre grown from this seed is pictured in Fig. 4.26 (b), showing the same result of no noticeable striations on the sapphire fibre or its edges. To further examine the findings, a rotated plate was installed on the cutting platform of the precision saw, and a sapphire slice was cut with a misalignment angle (7°) relative to the c-axis direction, as illustrated in Fig. 4.26 (c). Then, the sapphire fibres were grown from this specially cut wafer slice seed. After inspection, it was found that the striations had reappeared on the fibre, shown in Fig. 4.26 (d). These two growth tests with sapphire wafer slices not only verified the hypothesis that the striations inspected are actually facets, but also illustrated the fact that the appearance or absence of the facets on sapphire fibre depends on the orientation of the seed rather than the material form of the seed, in other words, whether the seed is a sapphire fibre or a sapphire wafer slice does not influence the existence of the facets. Therefore, to grow sapphire fibres without facets, the orientated c-axis sapphire seed should be used.

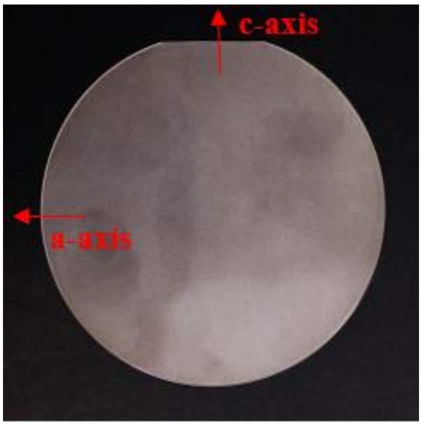

(a) sapphire wafer orientations

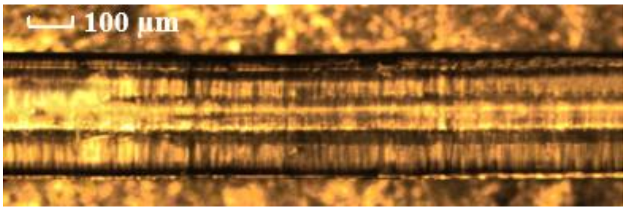

(b) fibre grown by c-axis seed fibre

(c) misalignment relative to c-axis

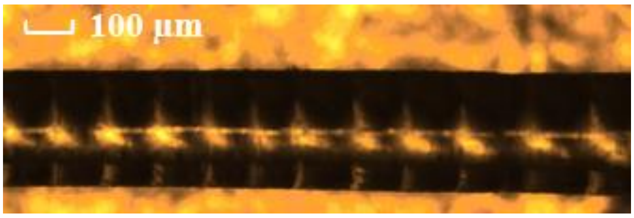

(d) fibre grown by the misalignment seed

Figure 4.26. Seeds with different orientations and fibres grown

The existence of the facets on sapphire fibres is undesirable in most cases especially in the aspect of transmitting optical information as facets on unclad sapphire fibres can further increase the surface scattering loss. However, the appearance of facets could become a natural advantage in some cases, for example, sensor applications. Although in this project, the LPFG sensor was produced through another method and facets were regarded as unwanted disturbance, the excellent periodicity of facets shown during the investigation has proven its great potential in designing an innovative grating-based sensor. Therefore, the dependence of facet period and depth on seed orientation can be investigated in future work.

4.3.3 Possible improvement to the system

After studying the issues and calibrating the system, high-quality straight sapphire fibres with a length of 3 to 7 cm were successfully grown with less than ±1.5% diameter variation, which were sufficient to serve as a sensing element in an optical sensing system. Nevertheless, it needs continuous observation and adjustment during growth. Some following modifications and improvements could be made to develop a more accurate and user-friendly growth system in the future.

Firstly, piezoelectric motors could be used to replace current mechanical motors for movement of the pull/feed arm. Compared with mechanical motors whose movement is not perfectly linear, piezoelectric motors can provide a smooth and linear movement for pull/feed movement at an elevated level. This would allow for crystal fibres with fewer imperfections to be grown. Secondly, a closed loop system could be installed to improve the interaction between the growing fibre and the control system. Once the diameter of the growing fibre changes due to the external disturbance, the control system could be used to monitor changes and adjust the corresponding parameters such as laser power and source rod position to counteract these changes. To monitor the diameter of growing fibre, a real-time diameter measurement function could be applied by programming LabVIEW software for calculating the fibre diameter from image pixels received by the viewing system. With a link to the control system, this set-up could eliminate most unexpected fluctuations during growth and improve the stability of growth. Last but not least, a beam expander could be used instead of a set of mirrors to increase the diameter of the laser beams. This could shorten the propagation distance of the laser beams, and thus reduce alignment errors which can appear due to mechanical creep. With these improvements, higher quality (with less than ±0.5 diameter variation) of sapphire fibres could be achieved by the LHPG system.

4.4 References to Chapter 4

[4.1] M. Fejer, "Single Crystal Fibers: Growth Dynamics and Nonlinear Optical Interactions," PhD thesis, Stanford University, 1985.

[4.2] Brad Snyder, About CO2 Lasers [online]. Available [data last accessed:17/5/2019]:https://www.synrad.com/resources/general_information/about co2lasers

[4.3] H. C. Seat, "Growth and characterisation of single-crystal fibres for sensing applications," Doctoral dissertation, Dept. Mech. Eng., Gla. Uni., Glasgow, UK, 2001.

[4.4] M. Fejer, L. Nightingale, G. Magel and R. Byer, "Laser-heated pedestal growth apparatus for single-crystal optical fibres," Rev. Sci. Instrum., vol. 11, pp. 55-58, 1984.

[4.5] R. Feigelson, "Pulling optical fibres," Journal of Crystal Growth, vol. 79, pp. 669-680, 1986.

[4.6] J. Harrington, "Single-crystal fiber optics: a review" in 2014 Proc. SPIE, vol. 8959, pp. 1-9, doi: 10.1117/12.2048212

[4.7] C. Nie, "Single-crystal, rare-earth doped YAG fibre lasers frown by the laser-heated pedestal growth technique," PhD thesis, University of New Jersey, 2017.

[4.8] L. Iskhakova and S. Lavrishchev, "Facet appearance on the later face of sapphire single-crystal fibres during LHPG growth," *Crystal*, vol 6, pp. 101-109, 2016.

[4.9] T. Ciszek and K. Yang, "Factors influencing surface quality and impurity distribution in silicon ribbons grown by the capillary action shaping techniques," *J. Cryst. Growth*, vol 50, pp. 160-174, 1980.

[4.10] P. Rodolph and T. Fukuda, "Fibre crystal growth from the melt," *Cryst. Res. Technol.*, vol. 34, pp. 3-40, 1999.

[4.11] J. Pollock and J. Bailey, "Fracture strength in tension of a-axis filamentary sapphire grown by EFG," *J. Mater. Sci.*, vol. 9, pp. 510-512, 1974.

[4.12] M.Klejch, M. Nemec, J. Kubat, “Preparation, properties and application of sapphire single-crystal fibres grown by the EFG method,” *EPJ Web Conf*. vol. 48, pp. 1-5, 2013.

[4.13] G. Young, J. Heminger, “Modelling the time-dependent growth of single-crystal fibres,” *J.Cryst. Growth*, vol. 178, pp. 410-421, 1978.

[4.14] S. Ishibashi, K. Naganuma, I. Yokohama, “Cr, Ca: Y3Al5O12 laser crystal grown by the laser-heated pedestal growth method,” *J. Cryst. Growth*, vol.183, pp. 614-621, 1997.

Chapter 5 – Design and Fabrication of Sapphire Fibre Sensors

Chapter 5 – Design and Fabrication of Sapphire Fibre Sensors

High-quality sapphire fibres were fabricated using the LHPG technique, demonstrating that the growth system was well calibrated and ready to be used for sensor development. To produce an effective sapphire fibre sensor for temperature or strain measurement in harsh environments, three sensor structures were investigated as potential candidates. Depending on the light source and detectors available in the lab, one of these would then be selected for further development. The design and fabrication of a sapphire capillary black-body radiation (SCBBR) sensor, a sapphire capillary Fabry-Perot interferometer (SCFPI) sensor, and a long-period sapphire fibre grating (LPSFG) sensor are presented and discussed in this chapter.

5.1 Sapphire Capillary Black-Body Radiation Sensor

5.1.1 Design of sapphire capillary BBR sensor

The design of the monolithic SCBBR sensor is shown in Fig. 5.1. There are three main parts to this sensor: a blackbody cavity to convert temperature into a radiation signal, a sapphire fibre to transmit this radiation signal to an analysis system, and a length of sapphire capillary to align the blackbody cavity and the sapphire fibre.

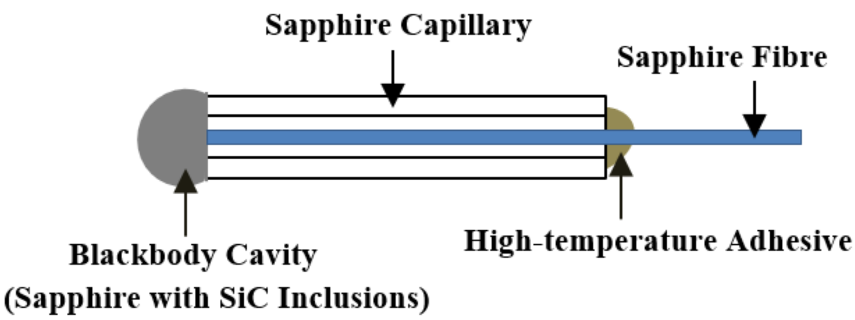

Figure 5.1. Design of the SCBBR sensor

Unlike the previous BBR sensors discussed in **Chapter 3**, whose blackbody cavities are produced either by coating the fibre tip with thin ceramic or by sputtering noble metal onto the fibre tip [5.1, 5.2], the blackbody cavity of SCBBR sensors are a combination of sapphire and silicon carbide (SiC). As a chemical compound of carbon and silicon, SiC was initially made by a high-temperature electro-chemical reaction of carbon and sand. Commonly, SiC has been used as an abrasive due to its high strength and high hardness. Now it is been widely used in refractory, ceramic, and various other high-tech applications. Since it has the properties of low thermal expansion coefficient, high thermal conductivity, excellent thermal shock resistance and chemical stability, the SiC material has also been used for applications in high-temperature environments, such as flame igniters, resistance heating and electronic components [5.3, 5.4]. At 1200 °C in air, a protective silicon oxide coating is formed by the material which can then work up to 1600 °C. Also, because of its high emissivity coefficient (0.96) [5.5], when the temperature of the SiC material rises, a large amount of thermal energy can be emitted in the form of radiation. As its radiation spectral behaviour corresponds approximately to that of a blackbody [5.6, 5.7], especially in 1 to 2.5 um region [5.8], SiC is frequently chosen as a near-blackbody or full-spectrum type of emitter material and widely used as a good approximation of a blackbody in infrared spectroscopy, optical antenna, thermophotovoltaic generator applications [5.7, 5.8, 5.9]. These properties make SiC an excellent candidate as a high-temperature sensing material for harsh environment.

Compared with other blackbody cavities in BBR sensors, this new blackbody cavity achieves the collaborative advantages from two high-temperature materials: SiC and sapphire. In conventional BBR sensors, the blackbody cavities made of thin ceramic or noble metal can be easily damaged by external factors in the sensing environment such as collision and friction, which greatly influences the stability of the radiation signal generated from the blackbody cavity, causing permanent damage to sensors. Also, in conventional BBR sensors, the addition of a protective coating to the outside of the blackbody cavity influences the conduction between the environment and the cavity, delaying the response speed of the sensor in dynamic or transient temperature measurements. Plus, with repeated thermal cycling, the coatings can detach from the fibre due to the thermal stressing arising from different expansion co-efficients. In contrast, with the proposed blackbody cavity design, the extreme hardness and excellent chemical stability of sapphire can help the sensor head weather most external physical damage and chemical corrosion; even if the outside is damaged, the solid spherical SiC-sapphire cavity can provide higher robustness than the thin cylinder film cavity in the conventional BBR sensors; the sapphire capillary can also protect the head of the transmission sapphire fibre to make sure the radiation signal from the cavity is safely received. Furthermore, the use of SiC and the LHPG technique in the fabrication process allows users to control the amount of SiC incorporated during growth. By removing the cost of using noble metals and sputtering techniques in conventional methods, this new method could develop a low-cost harsh environment high temperature sensor.

5.1.2 Fabrication of sapphire capillary BBR sensor

The core of the SCBBR sensor is the blackbody cavity. To combine the SiC and sapphire, the LHPG technique was applied. The whole procedure can be divided into three main stages, as shown in Fig. 5.2 below. Firstly, a length of the sapphire capillary was clamped in the v-groove on the pulling arm of the LHPG system. After alignment, the CO_2 laser was used to seal one end of the capillary by melting it, as shown in Fig. 5.2 (a). Once the end of the capillary was sealed, it was removed and held by a clamp on the bench. A measured amount of SiC powder was then added into the capillary from the other end, as shown in Fig. 5.2 (b) and Fig. 5.3. Lastly, the half-filled capillary was clamped in the same way on the pulling arm and melted by the CO_2 laser from the bottom to the halfway point while lowering the pulling arm, as shown in Fig. 5.2 (c). In this way, SiC and sapphire were combined at the end of the capillary and the SiC-sapphire solid cavity head was formed.

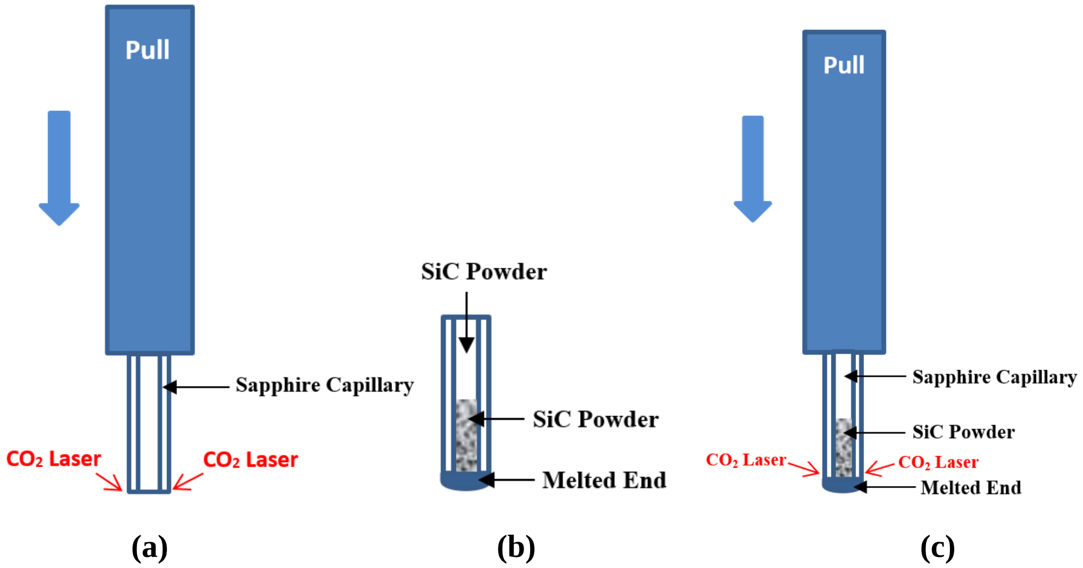

Figure 5.2. SCBBR sensor fabrication procedure: (a) seal the end of the sapphire capillary; (b) add SiC power into the sealed capillary; (c) combine sapphire and SiC.

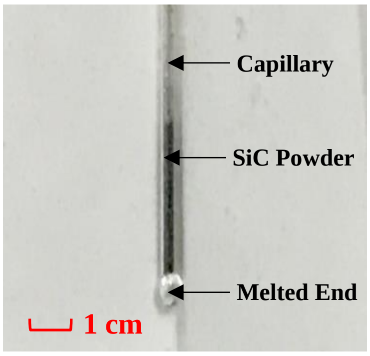

Figure 5.3. SiC powder in sapphire capillary

To control the size of the cavity produced, another method was applied, shown in Fig. 5.4. In this method, a sapphire slice was fixed on the feed arm. When the molten zone was formed during the combination process in Fig. 5.2 (c), the sapphire slice was fed to the molten zone and combined with it. By lowering the feed arm a short distance, a part of the material in the molten zone was pulled down with the wafer slice. Therefore, at this stage, when the feed and the pull arms were lowered and separated individually, the amount of melted material at the capillary end could be controlled, and a head with desired size could be formed at the end.

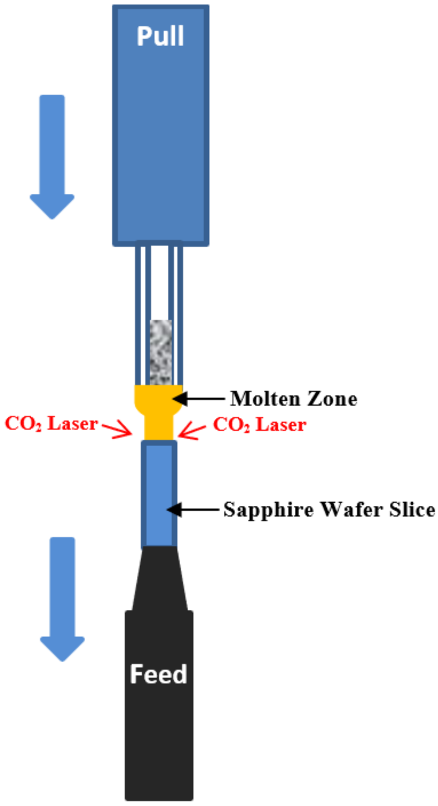

Figure 5.4. Head size control method

To compare the results, a head fabricated without and with size control were inspected under a microscope, shown in Fig. 5.5 (a) and (b), respectively. The diameter of the spherical head fabricated without size control method in Fig. 5.5 (a) was measured 954 µm, and the dimension of the head fabricated with size control method in Fig. 5.5 (b) was measured 446 µm length and 500 µm width. As it can be seen, the head fabricated without size control is clearly larger than the one with size control, indicating that the size of the head can be effectively controlled by this method. Compared with the original section of the sapphire capillary that is a clear and transparent, the SiC-sapphire head in both Fig. 5.5 (a) and (b) have a “frosted” appearance with a uniform grey color. This indicates that the SiC powder had combined and been homogenously mixed with the sapphire during high temperature growth. Therefore, the combination of sapphire and SiC for head fabrication was considered successful. With a SiC-sapphire head fabricated, a sapphire fibre can be inserted into the capillary from the open end to constitute the SCBBR sensor head for further tests.

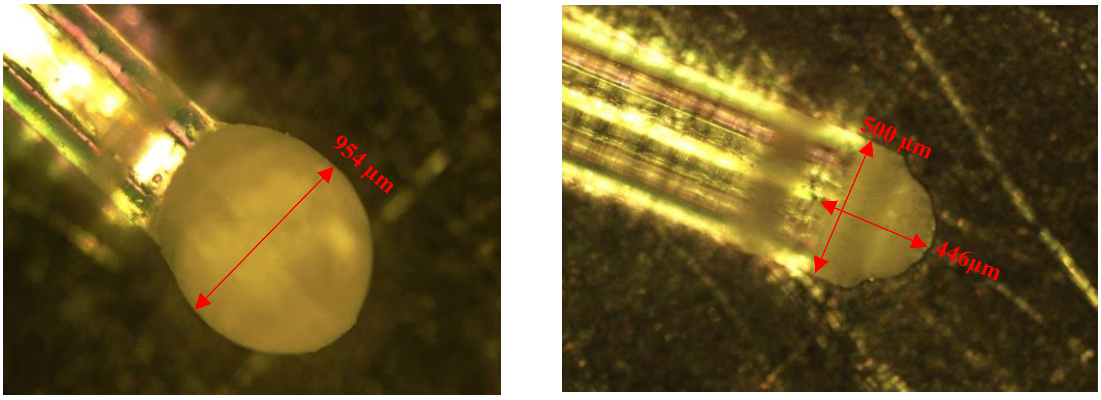

(a) **(b)**

Figure 5.5. Inspection of fabricated cavities: (a) the cavity without size control; (b) the cavity with size control.

5.2 Sapphire Capillary Fabry-Perot Interferometer Sensor

5.2.1 Design of sapphire capillary FPI sensor

The design of the sapphire capillary FPI sensor was built on the basic structure of an FPI [3.14]. There should be at least two mirrors in the FPI sensor to create two reflected light signals for interference signal. The schematic of the design is shown in Fig. 5.6. Like the SCBBR sensor designed above, a sapphire capillary is sealed at one end by the LHPG method. During this process, surface tension of the melted sapphire can help close the capillary end, ideally creating a relatively flat or concave inner surface. The reflection from the inner surface of the melted capillary end can be regarded as one “mirror”. Then a sapphire fibre can be inserted into the prepared sapphire capillary. This sapphire fibre delivers light to the sensing head and its end acts as the other “mirror”. By adjusting the distance between the two mirrors, an interference signal can be achieved in the reflected light. Once the desired interference signal is achieved, the capillary and fibre are bonded with high-temperature adhesive, and the sensor structure is completed.

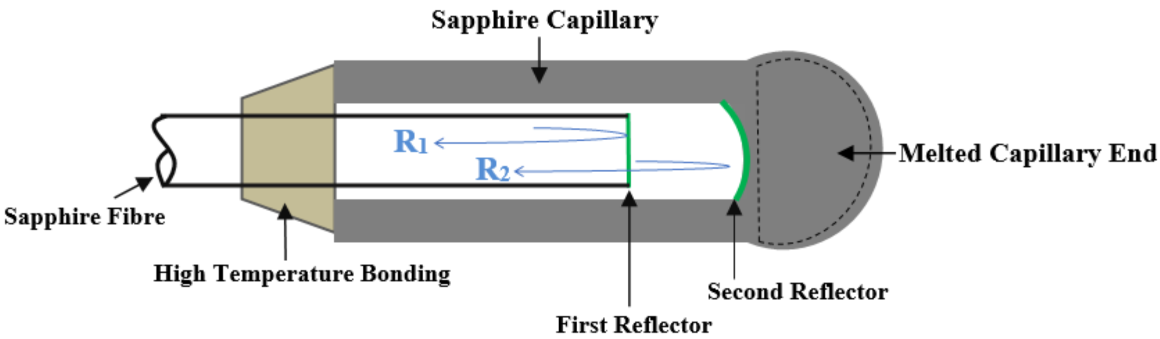

Figure 5.6. Design of the SCFPI sensor

Unlike the sapphire wafer-based FPI sensor discussed in **Chapter 3** [5.10], air-based FPI sensors have significant advantages such as low cost, enhanced functionality as the thermal expansion coefficient of air (3.4×10^{-3} at 25 °C) is much larger than sapphire (6.66×10^{-6} at 25 °C) [5.10]. Thus, compared with the wafer thickness change in high temperature, the larger and faster change of air cavity length provides the FPI sensor higher sensitivity and wider dynamic range in temperature measurement [5.11]. Besides, the in-line structure of the air-based FPI sensors makes them an ideal candidate for multipoint sensing applications. Compared with the zirconia tube air-based sensor [5.11], the SCFPI sensor has two significant improvements. Firstly, the SCFPI sensor only needs sapphire while the zirconia tube air-based sensor consists of two different materials in one sensor: zirconia and sapphire. This material advantage can be highlighted when the sensor is exposed to a harsh environment, especially a high-temperature environment: the difference in thermal properties of two materials becomes larger due to larger temperature changes, which can lead to separation of the sensor parts made of two different materials; also, thermal stressing of different materials interact with each other at high temperature, limiting thermal cycling of the sensor. These changes can further influence the sensing accuracy and sensor durability in practical use. However, using only sapphire to fabricate the sensor, this issue can be avoided. Secondly, the SCFPI also has the advantage of uniformity from its unique way of creating the mirror as a monolithic structure. The zirconia tube FPI requires the use of high-temperature bonding adhesive at both ends of the tube to fix the sapphire fibre, while the SCFPI only needs to bond the sapphire fibre and capillary at one point as one mirror is already a part of the capillary itself. This simplifies sensor structure and reduces the quantity of adhesive material used, which can reduce the possibility of error or failure caused by using adhesive as a different material in high temperature sensing, improving sensor stability and longevity.

5.2.2 Fabrication of sapphire capillary FPI sensor

To successfully fabricate an SCFPI sensor, the most challenging task is to make sure that the melted end of the capillary can work effectively as a second mirror to adequately reflect the light, not just in terms of its reflectivity and surface smoothness but also in terms of its shape. To achieve this, ideally the inner surface of the melted end should have the characteristics of a flat smooth fully reflective mirror in various aspects such as shape, surface quality and angle. Therefore, two methods were used to fabricate the second FPI and these methods compared in terms of ease of fabrication and optical performance.

5.2.2.1 Capillary melt method

In this method, a length of the sapphire capillary was mounted on the feed arm of the LHPG system in the same way as a source rod. After the initial alignment with the He-Ne laser, the CO_2 laser was focused onto the tip of the capillary end. By raising the power of the CO_2 laser, the tip of the capillary was melted, and a molten zone was formed on the capillary. Once the molten zone was formed, the end of the capillary was sealed by surface tension of the melt, and thus the inner surface was created between the molten zone and the capillary, as illustrated in Fig. 5.7 (a). However, it can be seen clearly in Fig. 5.7 (a) that the inner surface created by the molten zone was not flat or uniform in the horizontal direction. This was found to because the distribution of the CO_2 laser beam incident on the capillary was not perfectly symmetrical. Furthermore, unlike a normal source rod, the capillary was transparent and hollow, which influenced the distribution of the CO_2 laser heating on the top of the capillary. By manually manipulating the feed position in the x-, y-, and z-directions during the process, alignment to the fixed CO_2 laser spot could be adjusted to create an inner surface that was flat and parallel to the horizontal direction, shown in Fig. 5.7 (b). A picture of the entire capillary structure with the inner surface produced is shown Fig. 5.8.

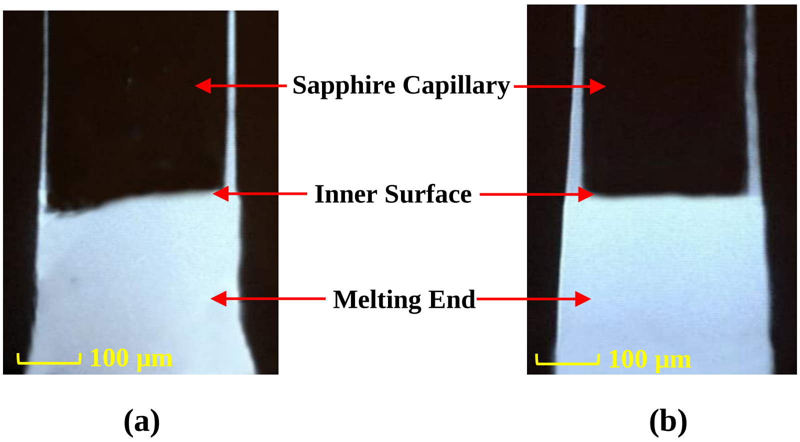

Figure 5.7. Melted capillary and formed inner surface: (a) the inner surface without manual adjustment; (b) the inner surface with manual adjustment.

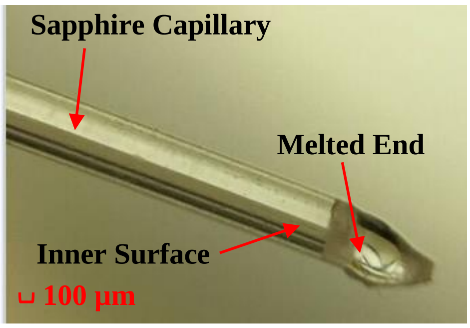

Figure 5.8. Produced sapphire capillary with an inner surface

The surface of an ideal FPI mirror should be smooth and flat, without any defects that can affect the direction and intensity of reflected light. Although the inner surface of the sample produced appeared relatively flat in the images taken externally by the viewing system and a camera, the view was from the inside of the capillary and the quality of the inner surface was still unknown. Since the flat inner surface was achieved by manual adjustment of the pull system, the quality of the inner surface should be further assessed as an FPI mirror. To obtain a better view of the inner surface, samples were polished in half along to capillary length as illustrated schematically in Fig. 5.9. To securely polish the capillary, the sample was hand-polished with a SiC grinding pad until the inner surface appeared. The reason for use of hand polishing rather than machine polishing is that it more effectively removes a larger area of sapphire. The sample was then further polished with the polishing machine using a 30 µm Al_2O_3 polishing pad to create a smooth and flat cross section for inspection. After polishing, the inner surface was exposed, and inspection can be easily achieved from the top or inclined top of the cross section.

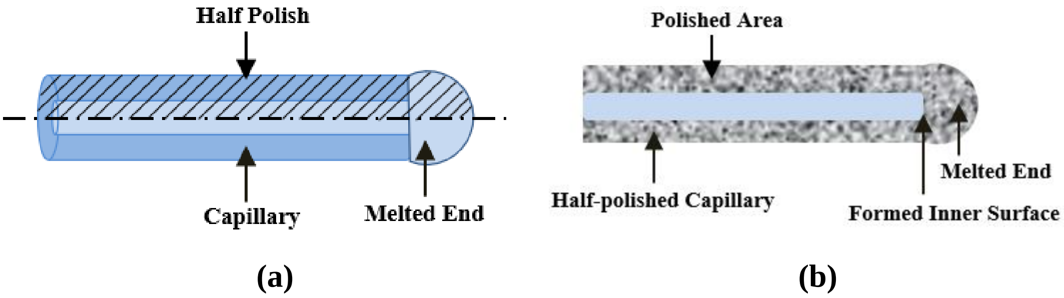

Figure 5.9. Polishing process: (a) illustration of polishing; (b) half polished sample.

Several groups of the sample were inspected under a microscope, the results showed that although the inner surface was easy to fabricate by the melting method, its quality, however, was variable and generally quite poor. Issues were apparent in several aspects including shape and roughness of the inner surface. The typical issues are shown in the images in Fig. 5.10. Image (a) indicates the issue of the poor shape of the inner surface. In this image, it can be seen that the profile of the inner surface was curved instead of flat; this is not suitable to serve as a mirror since a part of light cannot be reflected back to its original direction due to curved surface. In image (b), the microscope was focused on the formed inner surface to inspect its surface quality. As can be seen, the inner surface is rough, and the material shows a character akin to frosted glass, which can cause light scattering and reduce the proportion of light reflected. The inner surface in image (c) has a line-shaped physical structure in the middle, which can change the path of the reflected light as well. All these issues will lead to the change in direction of any reflected light as well as the loss of signal, and ultimately make it more challenging to obtain the interference signal for the FPI sensor. Due to the variability of the melt and the “unpredictable” features on the inner surface, this method was considered unsuitable for producing the internal reflective mirror for the SCFPI sensor, despite extensive efforts to control the inner surface shape by varying cooling rate, laser power, etc.

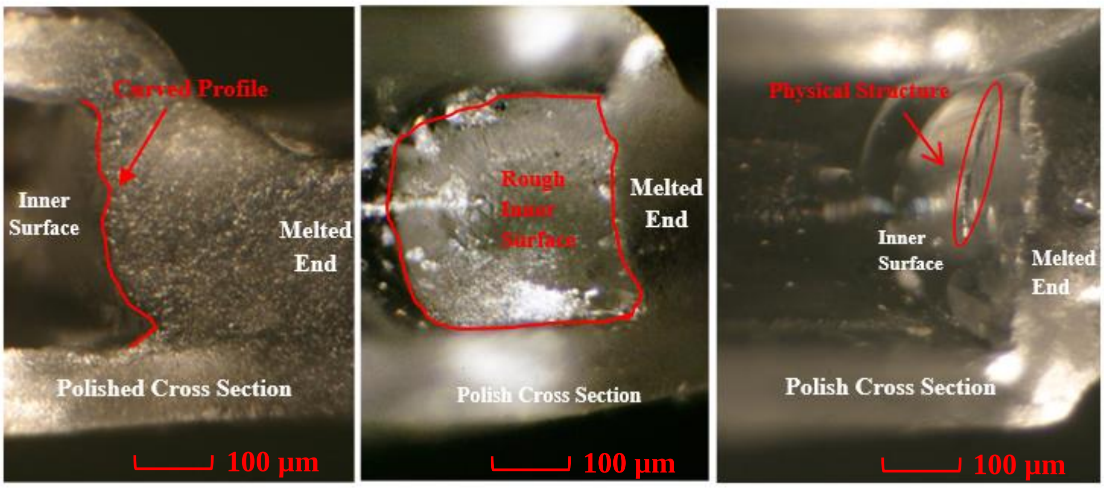

(a) (b) (c)

Figure 5.10. Inner surface inspection of half-polished samples: (a) curved profile of inner surface; (b) roughness issue; (c) line-shaped physical structure issue.

5.2.2.2 Crystal insertion method

As the initial method described above was found not to be effective, another method was devised and applied to form the inside mirror. The first step of this method was to use the LHPG system to grow a length of sapphire fibre. Then, one end of the sapphire fibre was polished and inserted to the sapphire capillary with the polished end inside. Lastly, this structure of the capillary and the inserted sapphire crystal was clamped to the feed arm, and the CO_2 laser was then used to bond them by melting the end of the crystal and sapphire capillary. As a result of the melting process, this sapphire crystal and the capillary are fused in a monolithic structure so that, the polished end of the crystal was fixed firmly inside the capillary as a mirror. Fig. 5.11 shows the sketch diagrams of the new FPI design. Since the end of the sapphire fibre grown was to be used as a mirror inside the capillary, its diameter had to be slightly smaller than the internal diameter of the capillary to ensure a smooth fit. The inside diameter of the sapphire capillary used in this experiment was 400 μm. After calculation and trials, a sapphire crystal with the diameter of 320 μm was successfully grown from a 1 mm diameter source rod with a pull/feed rate of 0.6/0.15 mm/min and laser power of 30%. A sketch diagram of the cross-section of the capillary and inserted crystal is shown in Fig. 5.12 (a) below. At the end of the crystal growing process, the pull rate was lowered from 0.6 mm/min to 0.4 mm/min while the feed rate was kept constant, which led to the diameter of the fibre increasing to 530 μm. With this growth setting, the crystal was then grown a further 3 mm to finalise the growth. With this additional 3 mm of growth, the end part of this fibre had a slightly larger diameter (530 μm) than the inside diameter of the capillary (400 µm), which let the fibre securely stuck onto the capillary and thus help the bonding/melting process. Fig. 5.12 (b) shows the sketch diagram of the grown crystal.

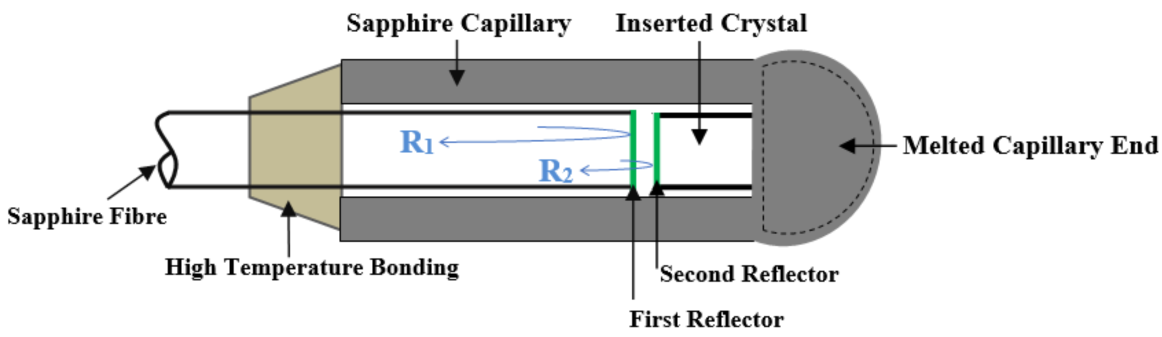

Figure 5.11. Design of the new SCFPI sensor

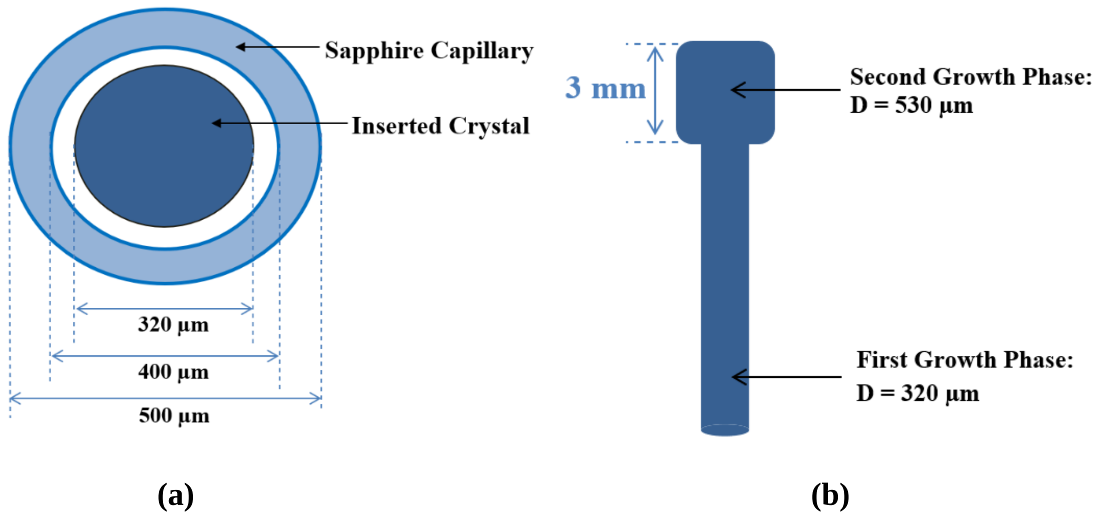

Figure 5.12. Schematics of the capillary and the inserted crystal: (a) cross sections of capillary and inserted crystal; (b) growth of the inserted crystal.

After growth, the 320 µm diameter end of the crystal was polished using 30 µm, 12 µm, 3 µm and 1 µm Al_2O_3 pad in order, and then inspected. Fig. 5.13 shows the images of “mirrors” produced by the previous method and the new method, respectively. Clearly, compared with the previous method, the quality of the new flat surface had been significantly improved to a new level; its smoother and clearer surface could readily perform the necessary function of reflective mirror. Once the polishing process was finished, the crystal was inserted into the capillary with the polished end first. Then the whole structure was mounted to the feed arm, and the CO_2 laser was applied to bond the crystal and capillary by melting their ends, as illustrated in Fig. 5.14.

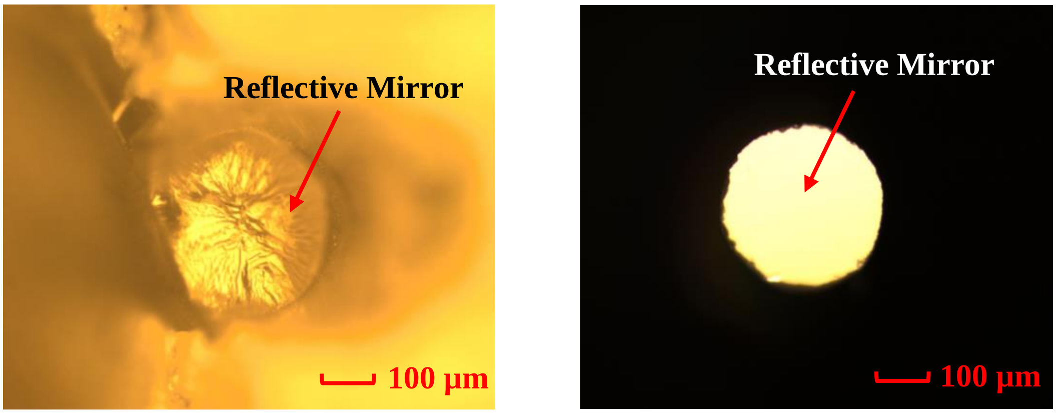

(a) (b)

Figure 5.13. Comparison of reflective mirrors produced by two methods: (a) original capillary end melt method; (b) new crystal insert method.

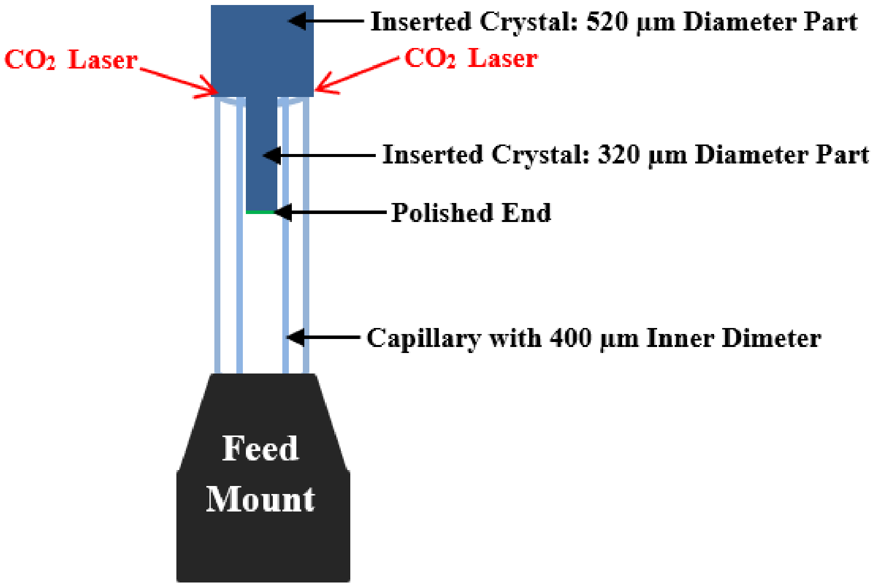

Figure 5.14. Bonding the inserted crystal and the capillary

After the melting/bonding process was complete, a length of sapphire fibre with a polished end was inserted from the other end of the capillary to act as the other FPI mirror. Once the interference signal is achieved, the sapphire fibre was then fixed in place and bonded with the capillary by high-temperature bonding adhesive. Therefore, the new FPI structure was completed. Moreover, as it can be seen from Fig. 5.15, the shape and the outside surface of the capillary melted end was irregular and rough, this prevented any other reflection from the outside surface acting as a pseudo-third mirror and affecting the sensor performance.

With this new method, a higher quality mirror could be produced inside the capillary, and the characteristics of this mirror such as size and quality could be manually controlled. At the same time, the advantages of the original SCFPI design over other sensors was retained.

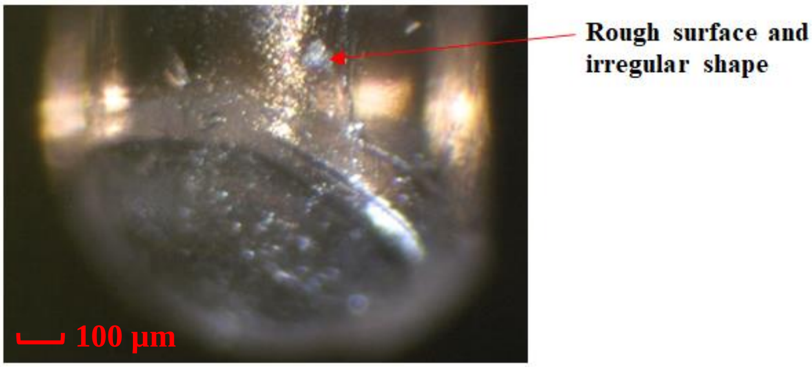

Figure 5.15. Outside surface of the melted capillary end

5.3 Sapphire Fibre Long-Period Grating Sensor

5.3.1 Design of sapphire fibre LPG sensor

The design of the LPSFG sensor is based on standard LPFG structures. Periodic modulation of the sapphire fibre diameter was achieving using the mechanical speed variant (MSV) technique during the LHPG process. As its name suggests, this technique introduces a modulation in diameter along the length of the fibre during growth by modulating the speed of pull/feed movement. With a periodically changing growth speed, the grating structure is formed along the fibre, schematically shown in Fig. 5.16. This process was controlled using the LabVIEW software detailed in **Chapter 4**. This allows users to set the desired grating parameters such as length, period, and fractional amplitude modulation (FAM) as the three principal settings. It is necessary to note that FAM of an LPG is the parameter which determines the difference between the maximum and minimum diameter of the gratings relative to the initial fibre diameter, as illustrated by Fig. 5.16 and Eq. 5.1 below. Therefore, a larger value of FAM indicates a larger difference between the maximum and minimum diameter of the grating, resulting a more visible and obvious grating structure.

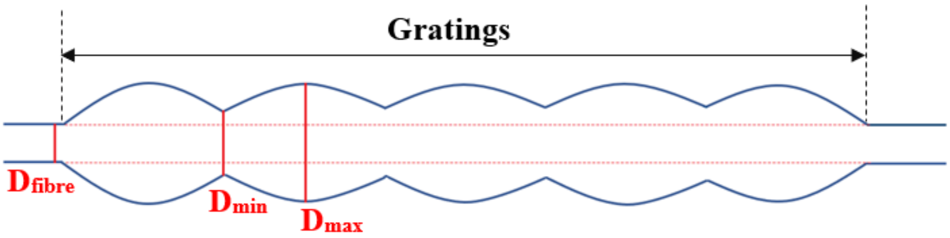

Figure 5.16. Schematic of LPFG produced by the MSV method

$$FAM = \frac{\frac{D_{max} - D_{min}}{2}}{D_{fibre}} \tag{5.1}$$

The inherent advantages of this LPSFG sensor originates from its unique fabrication technique. Compared with the physical dicing method explained in **Chapter 3** [5.8], the distinct advantages of LPSFG sensors fabricated by the MSV technique can be summarized with the following points. Firstly, the procedure of the MSV technique is simple, and this grating fabrication method is flexible. By inputting different grating parameters in the LabVIEW software, the desired grating fibre can be grown automatically; the diameter, length, and period of the grating fibre can be manipulated before and during the growth; also, it is easy to produce multiple gratings in a single fibre during fabrication. By contrast, in the dicing method, gratings need to be diced on a commercial sapphire fibre, so the parameters of the grating fibre are fixed and entirely depend on the product purchased. Secondly, not only sapphire, but different single-crystal materials or innovative doped materials can be used to fabricate LPG by changing the source rod for the MSV technique, which significantly expands the possibilities of creating grating sensors with various functions. Thirdly, due to the physical nature of dicing, the grating fibres are significantly more fragile and likely to be broken by vibrations during the fabrication or in use, especially when the diameter of the sapphire fibre is small; the quality of the gratings also highly depends on the quality of the diamond blade; however, with the MSV method, the gratings and fibres are fabricated together as one, and the quality of the gratings is only dependant on growth conditions; once a high-quality fibre can be grown with the LHPG system, smooth and clean grating structures can easily be produced as well. Fourthly, dicing along the fibre can only be unilateral [4.8], while the more obvious axially symmetric grating structure can be produced along the fibre by the MSV technique; with the more obvious grating structure, the grating effect can be improved, which could further increase the sensitivity of the sensor. Fifthly, because the dicing blade has its own thickness (60 μm in [5.8]), the minimum grating period (150 μm in [5.8]) that can be fabricated using this method is limited by blade thickness, and it is also difficult to fabricate more complicated microstructures besides gratings; while with the MSV technique, smaller periods of gratings and more complex fibre structures can be fabricated. Lastly but most importantly, financially speaking, to create the grating structure, a second difficult fabrication step is needed (dicing); while using the MSV method, all of the sapphire material is used to produce the grating structure in "as-grown" fibres without wasting any material. To summarise, compared with grating fabricated with the previous methods, this newly designed LPSFG has advantages in production flexibility and efficiency, the potential sensor performance, and cost due to its unique fabrication method.

5.3.2 Fabrication of sapphire fibre LPG sensor

5.3.2.1 Calibration of grating growth

To grow fibre gratings with the LHPG software, the choice of grating parameters was selected in the "growth options" panel. Then the period, length, and FAM of grating can be set with the desired values. When all the parameters are set, the growth can be started. The software is programmed to grow a length of straight fibre before and after gratings as the transmitting part of the LPSFG sensor. Once the desired length of straight fibre is grown, the user can initiate the grating growth by pressing the start button in the grating section. When the grating growth is finished, the system is set to grow another length of straight fibre automatically until stopped by the user. With a uniform initial alignment of the CO_2 laser on the source rod, gratings can be fabricated successfully. Fig. 5.17 shows the examples of the grating structure grown by the system.

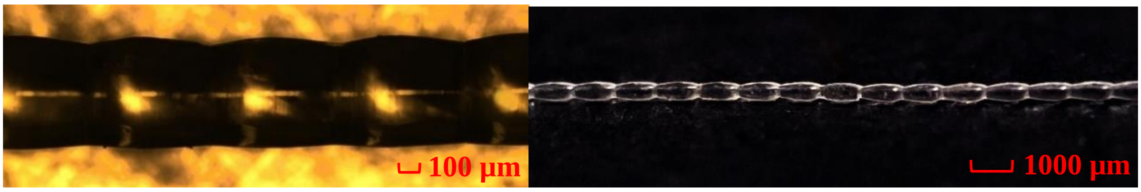

(a) (b)

Figure 5.17. Grating structure grown by MSV method: (a) microscope image; (b) camera image.

To help profile the gratings, microscope software (SPOT) was used to measure and examine the grating parameters. Upon investigation of several groups of grating, the length of the grown gratings was consistent with the original setting. However, a large inconsistency was found in the grating period and FAM between the actual grown gratings and original settings due to errors (the constant diameter setting of source rod and seed crystal) in the LabVIEW program. To fix this inconsistency error, a calibration procedure was conducted. In this procedure, the grating period and FAM were calibrated respectively to investigate the relationship between the original settings and the actual growth.

Two fibres were grown with different groups of gratings along each of them. For the first fibre, seven groups of gratings were grown along it, separated by five intermediate sections of 3 mm straight growth. The only difference between each group of gratings was the grating period, which means they have the same settings of pull/feed rate (0.5/0.25 mm/min), grating length (3 cm), FAM (0.5), and laser power (35%). Seven different periods values were used, from 200 µm to 800 µm, with a step of 100 µm. Fig. 5.18 shows an example of a length of sapphire fibre with different groups of gratings. Likewise, to study the inconsistency of FAM, the same settings of pull/feed rate (0.5/0.25 mm/min), grating length (3 cm), grating period (500 µm) and laser power (35%) were used to grow six groups of gratings on the second fibre with the only difference being the FAM setting (from 0.5 to 1 with a step of 0.1). The reason that the FAM value was not set from 0 but 0.5 was because there were no obviously visible diameter changes on the fibre if the value was set below 0.5, thus making measurement difficult and imprecise; hence, the measurement of the minimum and maximum diameter of the grating structures for calculating the FAM value was not as reliable. To analyse the result, once each fibre was grown, the corresponding physical parameter of the gratings in each group were measured and recorded to obtain the values of the period and FAM. The result of the relationship between growth value and original setting is presented in Fig. 5.19. As the line graphs show, the linearity of both relationships is excellent, this indicates the inconsistency arises from systematic parameter errors in the LabVIEW program. The relationships between the original setting and the actual growth data can be fitted using linear fitting equations. These two equations were then used as the new standard for the calibrated grating growth system. To check the accuracy of the calibrated system, a new fibre grating with a period of 1000 µm and 0.7 FAM was set as the growth setting. After the growth, the period and the FAM value of the grown grating were measured as 992 µm and 0.67, respectively. This indicated an accuracy of 99.2% for period and 95.7% for FAM; this was far more acceptable compared with the large inconsistency in the previous system with the accuracy of 90% for period and 2% for FAM.

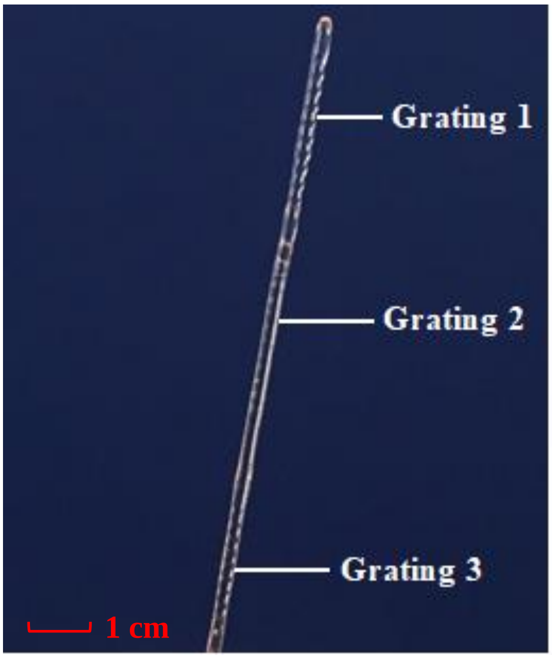

Figure 5.18. A length of sapphire fibre with different groups of gratings

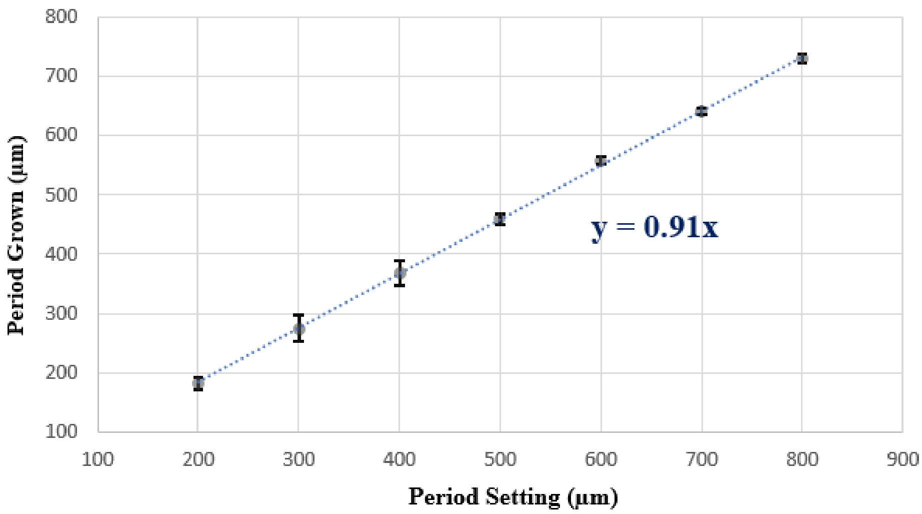

(a)

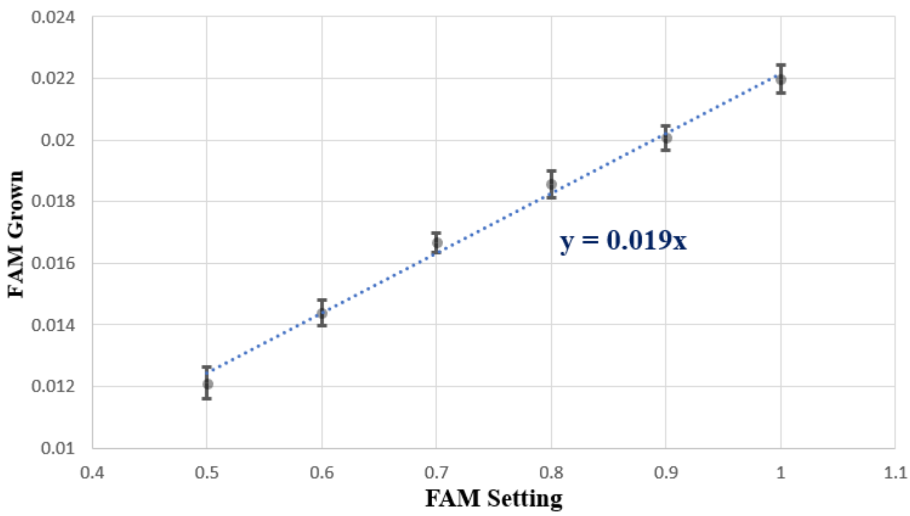

(b)

Figure 5.19. Result of the calibration: (a) period calibration; (b) FAM calibration

5.3.2.2 Fabrication of minimum period grating

As Eq. (4) in **Chapter 3** illustrated, the effective index of a sapphire fibre is fixed, when the effective index of the cladding is also fixed, the grating period is the only physical parameter that determines the resonant wavelength of an LPFG sensor. Thus, determining the minimum grating period that can be produced by the MSV technique is vital to locate the resonant wavelength in a practical sensing experiment. For example, in the same system, a grating sensor with a larger grating period produces a larger the resonance wavelength compared to the one with a smaller grating period. With knowledge of the estimated resonant wavelength, a suitable detection system can be selected to obtain the resonance wavelength and study the performance of the LPFG sensor. Therefore, an experiment to determine the minimum period grating that can be produced by the system was conducted.

Since gratings with periods of hundreds of micrometres had been successfully grown and inspected during the calibration process, the experiment to determine the minimum period grating was conducted in steps of tens of micrometres. The process was to grow four groups of gratings with different periods, in order of period size on the same sapphire fibre. The same growth settings (pull/feed rate of 0.6/0.2 mm/min, laser power of 25%, FAM of 0.02), excepting the grating period, were used to grow the gratings. Gratings with a period of 10 µm, 20 µm, 30 µm, and 40 µm had been grown, each with a length of 3 cm, on a single sapphire fibre, separated by 3 mm of straight growth between each grating. The as-grown fibre with the 4 groups of gratings was then inspected. As is shown in Fig. 5.20 below, the 10 µm grating part showed no grating structure along the fibre even in the enlarged view; also, the edge of the fibre was flat and showed no evidence of diameter change. As is presented in Fig. 5.21, by increasing the period to 20 µm, 30 µm, and 40 µm, the grating trace became more and more evident in both shape and visibility; for the 20 µm and 30 µm gratings, the grating trace is not clear and consistent, which could affect the periodicity of the grating and further impact the success of sensor production; the grating trace became regular and consistent in clarity along the fibre when the grating period was increased to 40 µm; also, in the enlarged view, the edge of the sapphire fibre of the 40 µm period grating started showing the typical periodic change in shape and diameter, presented in Fig. 5.21 (d). With its clear grating structure and good periodicity, the 40 µm period grating was considered as the eligible candidate for sensing tests. Therefore, to produce a clear grating structure, the minimum grating period should be set above 40 µm. Compared with the minimum grating period (150 µm) fabricated by the dicing method, the use of the MSV technique permits the production of a resonant wavelength in a lower wavelength range under same condition, providing a wider wavelength selection for the light source and signal analyser. With the grating growth system calibrated and the effective minimum grating period found, gratings with periods ranging from 40 µm to 1000 µm could readily be fabricated on sapphire fibres in the lab.

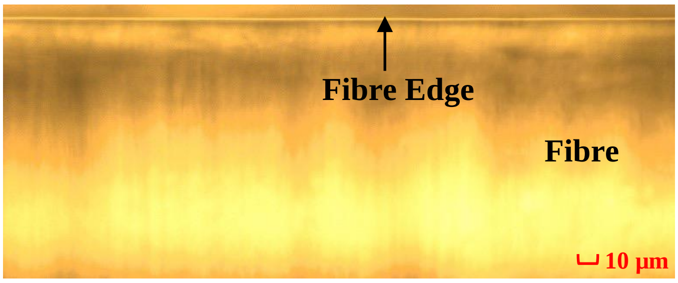

Figure 5.20. The fibre edge of the 10 μm gratings

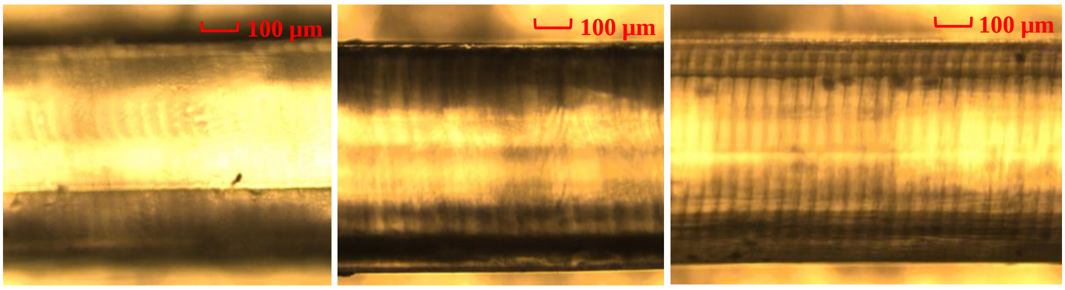

(a) **(b)** **(c)**

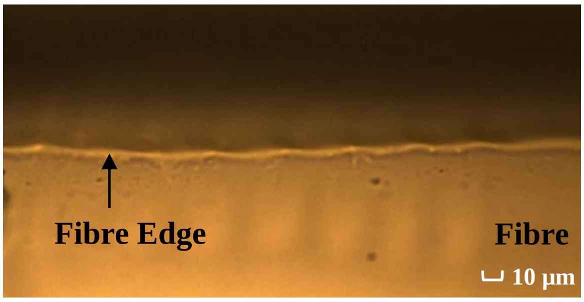

(d)

Figure 5.21. Images of gratings with different period on the fibre: (a) 20 μm period grating; (b) 30 μm period grating; (c) 40 μm period grating; (d) the enlarged view of the fibre edge of the 40 μm period grating.

5.4 References to Chapter 5

[5.1] Y. Zhu, Z. Huang, F. Shen and A. Wang, "Sapphire-fibre-based white-light interferometric sensor for high-temperature measurements," *Optics letter*, vol. 30, pp. 711-713, 2005.

[5.2] M. Jones and D. Barker, "Use of blackbody optical fiber thermometers in high temperature environment*," Journal of Thermophysics and Heat Transfer*, vol. 16, pp. 1-16, 2002.

[5.3] The Accuratus staff writers, "Silicon Carbide, SiC Ceramic Properties," *Accuratus*, 2013. [online]. Available: http://accuratus.com/silicar.html [date last accessed: 17/4/2016]

[5.4] Y. Zhu, Z. Huang, F. Shen and A. Wang, "Sapphire-fiber-based white-light interferometric sensor for high-temperature measurements," *Optics letter*, vol. 30, pp. 711-713, 2005.

[5.5] J. Wang and B. Dong, "Multiplexed high temperature sensing with sapphire fibre air gap-based extrinsic Fabry-Perot interferometers," *Optics letters*, vol. 5, pp. 619-621, 2010.

[5.6] S. Grice, "Optical fibre sensor and their applications in the industrial weighing and aerospace industries," *PhD thesis*, Aston University, 2010.

[5.7] A. Kos, J. Chen, W. Bock, and P. Mikulic, "Tapered long-period grating (TLPG) with teflon AF coating for pressure sensing application, "in *2008 Canadian Conference on Electrical and Computer Engineering*, Niagara Falls, 2008, pp. 861-866. doi: 10.1109/CCECE.2008.4564658.

[5.8] S. Nam, C. Zhun, and S. Yin, "Recent advances on fabricating in-fiber gratings in single crystal sapphire fibre," in: *Conference on Photorefractive Fiber and Crystal Devices Materials, Optical Properties and Applications X*, Denver, 2004, pp 147-155. doi: 10.1117/12.558656

Chapter 6 – Sapphire Capillary Blackbody Radiation and Fabry-Perot Interferometer Sensors

Chapter 6 – Sapphire Capillary Blackbody Radiation and Fabry-Perot Interferometer Sensors

As three proposed potential sensors, SCBBR, SCFPI, and LPSFG, were designed and successfully fabricated, the next step was to choose the most suitable sensor for sensing experiments and further development. Based on the components and devices currently available in the lab, initial tests were conducted to select the applicable parts for experiment systems for each sensor. As a result, among the three sensors, LPSFG showed the highest potential, producing the most positive results and breakthroughs. Thus, it was targeted as the sensor for further development in this thesis, which is detailed in **Chapter 7**. However, although the initial tests on components and equipment for SCBBR and SCFPI experiment were not entirely positive, the test results of components with sensors, and whole system building procedure provides valuable information and guidance for building sapphire fibre-based sensor systems. Thus, this chapter is dedicated to the investigation in building the sensing system of SCBBR and SCFPI sensors.

6.1 Design and Setup of SCBBR Experiment System

6.1.1 Design and setup

As the SCBBR sensor was fabricated, the next step is to test the performance of the sapphire capillary blackbody cavities. The basic design of the BBR sensing system consists of three parts: a signal transducer, a signal transmission medium, and a signal detector, shown in Fig. 6.1 below.

Figure 6.1. Basic design of BBR sensing system

The signal transducer of the BBR sensor consists of a blackbody cavity and an external heating source. As the blackbody cavity was fabricated and discussed in **Chapter 5**, the main task is to choose a suitable heating source that can provide a stable heating from room temperature to 1000 °C, which can either be furnace or the flame heating [6.1, 6.2]. For the transmission medium to the detector, a fibre transmission method was proposed. As the temperature of the heating source is high, high-temperature fibres are required for tests. The signal detector is used to receive radiation signal and transfer it into electrical signal for study and analysis. In the next section, different choices of components in the system are tested and analysed to select the most suitable components for the SCBBR sensing system.

6.1.2 Tests on system components

6.1.2.1 Heating sources

To provide a stable heating source for testing the BCBBR sensor, the temperature of the heating source should be able to reach at least 500 to 1000 °C range to provide an effective radiation signal for a BBR sensor [6.2]. Also, the temperature of the heating source needs be able to be held for at least 5-10 minutes at each 100 °C for data acquisition. With these two standards, the tests of two heating sources, flame heating and furnace heating, were conducted.

A refillable *BRS* butane gas flame was used and tested as the flame heating. A testing system is shown in Fig. 6.2. In this system, a *Hilka* 125 K-type digital thermometer was used to measure the temperature of the outer flame. For the furnace heating, shown in Fig. 6.3, a *GRD* B410 tube furnace and the same thermometer were used. The length of the heating tube of is 32 cm and the tip of the thermocouple wire was positioned at the middle point of the furnace tube (16 cm) from one side. After that, both sides of the tube were blocked tightly with ceramic fibre to preserve the heat. The temperature of the furnace can be controlled by changing the power of the furnace in the control panel. The target of the test is to measure the time that the heat sources needs to reach 1000 °C. In the flame test, as the flame temperature rises almost instantly in the air, and the fact that the size of the capillary head is quite small (~0.45 mm^3), the temperature change of the capillary in the flame is directly estimated by that of the thermocouple. Due to the natural high temperature of the flame, the temperature rise is rapid, so the temperature was recorded every minute. In the furnace heating tests, the temperature of the furnace was set to 1000 °C at the beginning for continuous heating and the temperature was recorded every 15 minutes.

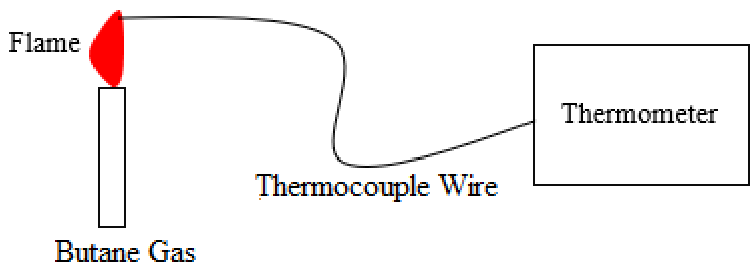

Figure 6.2. Flame heating testing system

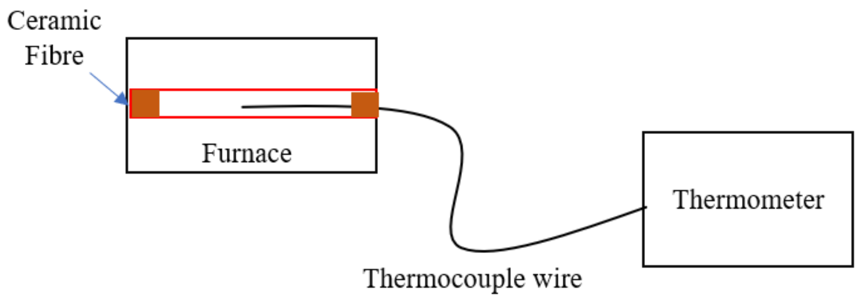

Figure 6.3. Furnace testing system

The tests result of two heating methods is shown in Fig. 6.4. For flame heating, it can be seen that the temperature rose from room temperature (23 °C) to 986 °C in only 5 minutes; it only took 1 minute for the temperature rising from room temperature to 294 °C. In the furnace test, the temperature rises to 420 °C in the first hour steadily. In the second hour, the speed of temperature increase becomes slower, only reaching 710 °C at the end of second hour. In third and fourth hour, the temperature increases much slower, only reaching 760 °C at the end of the fourth hour. After that, the temperature of the furnace stops increasing and staying in the range of 758 °C to 761 °C even when the temperature of the furnace was set to 1000 °C.

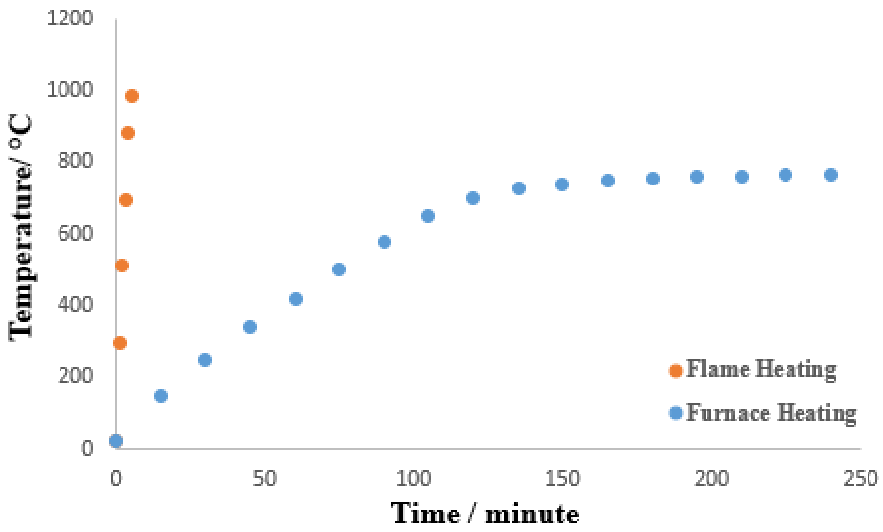

Figure 6.4. Temperature test of the two heating sources

Compared with furnace heating, the flame heating can reach the working temperature easily in a short time period in the air without requiring any components to preserve its heat. However, since the temperature rises quickly (~ 5 mins to 1000 °C), the radiation from the BCBBR sensor at each hundred temperature cannot be easily scanned and recorded properly, even using middle or inner zone of the flame to heat or changing the distance between flame and thermocouple. The unstable nature of the flame led to large variations in temperature. Depending on the step settings, each spectral scan usually takes about 5 to 10 minutes with the monochromator system in the lab. However, the only stable radiation the BCBBR sensor can provide is at its highest temperature (~1000 °C). This makes it difficult to study the relationship between the radiation spectrum and temperature change. For furnace heating, the temperature of the furnace can be easily controlled by the power control at a desired number with error of ±2 °C. Nevertheless, the maximum working temperature that this furnace could achieve was only about 750 °C in the hottest point, taking 4 hours to reach.

In terms of the whole sensing system, comparatively speaking, furnace heating is more suitable since its step heating function provides enough time for the blackbody spectra to be scanned properly. Also, in flame heating, the light from the flame itself can be easily picked up by the transmission system and becomes a large unwanted interference signal when scanning the spectra from the blackbody cavity. Even so, furnace heating has two obvious shortcomings. One is that the maximum working temperature (750 °C) limits the data that can be obtained in the experiment, especially in this case, the radiation signal source is the blackbody cavity which performs better at high temperatures (above 500 °C) than low temperatures. The other shortcoming is that due to the long length of the furnace heating tube (32 cm of this furnace), a high-temperature coupling fibre is required to collect the radiation signal produced by the blackbody cavity out of the furnace from its middle point for further transmission and analysis. Overall, if the maximum temperature of the furnace can be raised to 1000 °C, it would become an ideal heating source for the SCBBR sensing system.

6.1.2.2 Transmission medium

As the furnace heating was considered as the suitable heating method for the system, the next step is to find the right transmission medium to deliver the radiation signal to the detector. A length of high-temperature fibre is required to collect the radiation signal from the furnace for further transmission and analysis. Two components had been considered to be used as the high-temperature fibre, one is the commercial multimode high-temperature fibre, such as the silica core gold cladded high-temperature fibre; the other is to grow a long sapphire fibre with LHPG system as the high-temperature fibre. As the sapphire fibre can be grown with a large diameter core (300-500 µm) in the lab, to collect more radiation signal from the blackbody cavity, it was selected as the high-temperature fibre.

The longest sapphire wafer slice (1 mm diameter and 6.4 cm length) slice in the lab was selected as the source rod and a c-axis sapphire fibre (300 µm diameter and 2 cm length) was used as the seed. The pull/feed rate of 0.6/0.18 mm/min and CO_2 laser power of 25% were used to start the growth. A 14 cm length, 360 µm diameter fibre was grown. The both ends of the long fibre were polished to 1 µm. Although the length of the sapphire fibre is slightly shorter than the half length of the heating tube (16 cm), it can deliver the signal from the hottest point of the furnace to a lower temperature point where the glass fibre can be used to further transmit the signal. To test the transmission ability of the long sapphire fibre, a broadband light transmission system was built, shown in Fig. 6.5.

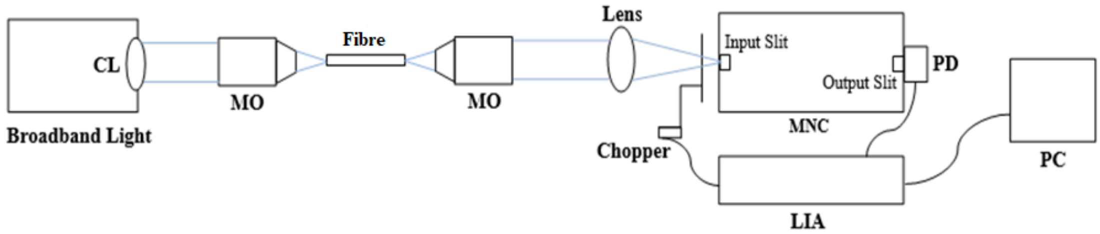

Figure 6.5. Broadband light transmission system

In the system, A broadband light, Schott KLT-1500-T lamp was selected and used as the light source. The light signal from the light source was coupled into the long fibre through an optical transmission system. A collimating lens (CL) outside the lamp transfers the light into a × 20 microscope objective (MO) which then focuses the light onto one end of the long sapphire fibre. The light exiting from the other end of the fibre was collected by another ×20 MO and then focused onto the entrance of the signal analysis system via another lens. The signal analysis system consists of four parts: a DK480 series monochromator (MNC) from *CVI Laser Corporation*, an ET-2030 silicon PIN photodetector (PD) from *Electro-Optics Technology Inc*., a SR 530 lock-in-amplifier (LIA) from *Sci-Tech*, and a computer-controlled data acquisition system. The MNC with minimum resolution of 0.06 nm was used to receive the output light from the fibre. The motorised input and output slits of the MNC has a step of 1 μm, which can provide a quick and accurate adjustment for different light inputs. At the entrance slit of the MNC, an optical chopper was placed to modulate the output signal from the LPSFG and used as the reference signal for the linked LIA. At the output slit of the MNC, the photodetector was installed for detection of the selected wavelengths. For a given sensitivity in LIA (e.g. 10 mv, 3 mv or 1000 μv as used in this case), it produced ±5 V output at full scale deflection. After being amplified by the LIA and the output voltage transformed into a digital signal, the computer-controlled data acquisition system was used to plot a spectrum of intensity in arbitrary units versus wavelength.

A shorter sapphire fibre (3 cm length) with same diameter (360 μm) and same polishing ends (to 1 μm) was grown and used as the reference to compare with the long sapphire fibre (14 cm). Fig. 6.6 (a) shows the spectrum of the output light from the short sapphire fibre, which is the same as the spectrum directly from the light source, peaking at two wavelengths, 750 nm and 950 nm. When the output light from the long sapphire fibre was scanned using the same system and settings, however, very little signal but much noise could be detected by the system, shown in Fig. 6.6 (b), even when higher sensitivity setting was used for the LIA. This is because of the transmission and coupling losses in the long sapphire fibre were so high that amount of the output light from the end of fibre was very small such that it could not be detected by the system. This can also be observed directly from the fibre itself in the system; for the 3 cm length sapphire fibre, when the light was input into one end, the fibre itself was bright and a light spot was clearly visible at the output end too; however, when the same amount of light was input into the 14 cm length fibre, the brightness decreased along its length and finally faded out in the middle of the fibre. The output end of fibre showed no visible illumination, indicating little light was transmitted through the whole length of fibre. The illustration of the light transmission along two fibres is shown in Fig. 6.7. Both transmission spectra were scanned with same LIA settings (sensitivity of 3 mv and time constant of 1 s). As it can be seen from the spectra and illustration graph, most of the light was lost during the transmission in the fibre. There are mainly three reasons for this issue. Firstly, unlike normal fibres with cladding, the sapphire fibres do not have claddings to help guide and transmit the light in the core, therefore, a large amount of light can be lost at the core-air interface. Secondly, since the loss of sapphire fibres is larger than conventional fibres with cladding, the longer a sapphire fibre is, the larger amount of light the fibre will be lost. The length of the sapphire fibre is too long to deliver the same amount of light that a short length of sapphire fibre (3 cm) can deliver. Thirdly, although the LHPG system was calibrated, defects can still be observed along the length of the long fibre, such as small diameter changes, which can cause loss as well. For these reasons, the long sapphire fibre grown is not suitable to transmit light signal in this system.

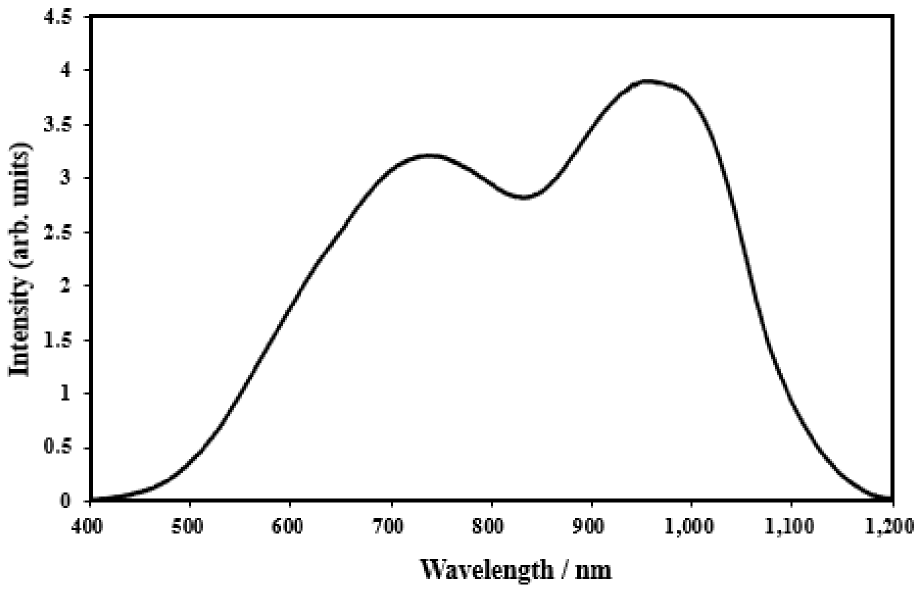

Figure 6.6. (a) Spectrum of the transmitted light from 3 cm sapphire fibre

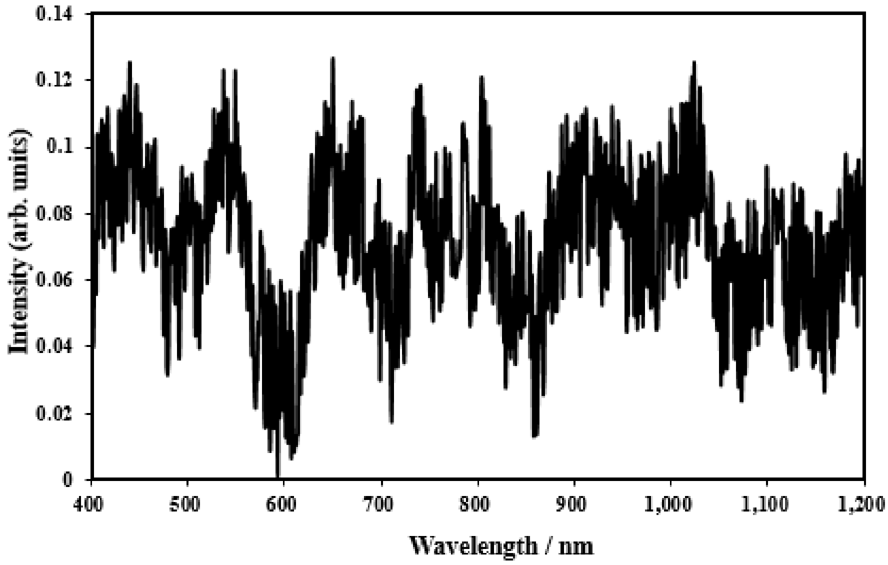

Figure 6.6. (b) Spectrum of the output light from 14 cm sapphire fibre

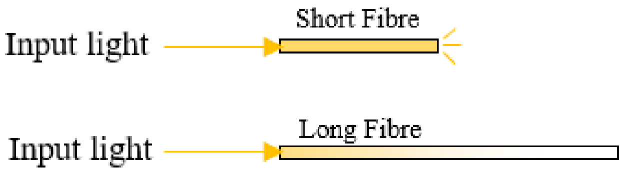

Figure 6.7. Illustration of light transmission of two fibres

6.1.3 Improvements and future work

With the help of these initial tests on heating sources and transmission medium, the improved design can be made to build an ideal SCBBR testing system in future work. First, the furnace heating should be used instead of flame heating to provide a stable and accurate temperature rise. The highest working temperature of the furnace should be at least 1000 °C to provide enough temperature range to obtain the corresponding radiation signals from the sensor. As the size of common high-temperature furnaces are large, to deliver the radiation signal generated by the sensor head, high temperature fibres should be used. Sapphire fibres with high temperature cladding can be used in this situation to prevent large losses [6.3, 6.4]. The other option is to use a small length of sapphire fibre to deliver the signal from the hottest point of the furnace, and then using a high-temperature fibre for further transmission. Sapphire fibres and high temperature fibres can be bonded by direct material bonding or fusion splice [6.4]. In this way, the advantages of both sapphire fibre and high-temperature fibre can be used at the same time. The large core of sapphire fibre can help receive more radiation signal from the blackbody cavity at a higher temperature, and the high temperature fibre can then deliver the radiation with little loss at a relatively lower temperature. Once the signal is delivered out of the furnace, it can be further transmitted to the detector to study the performance of the sensor.

In order to develop the BBR prototype to a working sensor, two avenues of work would need to be pursued. In terms of sensing structure, the size of the sensing head and the amount of SiC doping in the sapphire sensing head need to be investigated in order to optimise BBR spectral characteristics (in terms of ideal BBR spectral) at a high temperature environment (500 to 1000 °C). After this optimisation is complete, the end of the BBR capillary should be sealed with the CO2 laser to bond the sensing head to a transmission sapphire fibre. In this way, the head of the transmission sapphire fibre can be protected by the capillary and the radiation signal can be steadily transmitted outside of the high-temperature zone for further analysis. In terms of data analysis, the colorimetric method detailed in [6.5, 6.6, 6.7], can be used as the temperature measurement method, which uses the radiation power ratio from the measured object at two wavelengths as an indicator of temperature. In this way, the errors caused by the changes of optical signal loss during transmission, coupling, insertion, and also changes in emissivity at different temperature can be compensated [6.5]. Thus, the temperature can be measured with improved accuracy and the influence of environment and emission rate can also be eliminated.

6.2 Design and Setup of SCFPI Experiment System

6.2.1 Design and setup

To test the feasibility of the SCFPI, two designs of the SCFPI experiment system were proposed: coupler-based FPI system and splitter-based FPI system. The light source and detecting system used in both systems are same as that in the SCBBR system: a broadband light and a monochromator detecting system. The coupler-based FPI system has been widely used in FPI sensors studies for decades [6.8, 6.9, 6.10]. Since the signals are all transmitted in the cladded fibre with coating, the signal loss is small so the weak reflected signal can be detected. The splitter-based FPI system is the FPI system developed for the monochromator system as it uses slits to receive the signal instead of fibre connectors. For the coupler-based FPI system, as illustrated in Fig. 6.8, a TM105 1 × 2 multimode fibre optic coupler with 105 μm core diameter and 50:50 split ratio from *Thorlab* was used. As is shown, the light source was first coupled into arm 1 of the coupler by a × 20 microscope objective (MO); then, the input light transmits to the arm 2 on the other side of the coupler to interact with the FPI sensor. At arm 2, the light in the coupler fibre was first coupled into a straight sapphire fibre (7 cm length, 380 μm diameter, both end polished to 1 μm), then it was further delivered to the inner surface of the capillary fabricated by the inserted crystal method discussed in **Chapter 5**; ideally, the end of the straight fibre in the capillary forms the first reflector of FPI and the inner surface of the capillary forms the second. With the appropriate gap between two reflectors, the interference signal can be generated in the reflected signal and then transmitted back to the arm 3 and detected by the signal analysis system. It is necessary to note that all the transmission spectra reported in following part of this chapter were scanned with same LIA settings (sensitivity of 3 mv and time constant of 1 s) for the only comparison in terms of sensing structures.

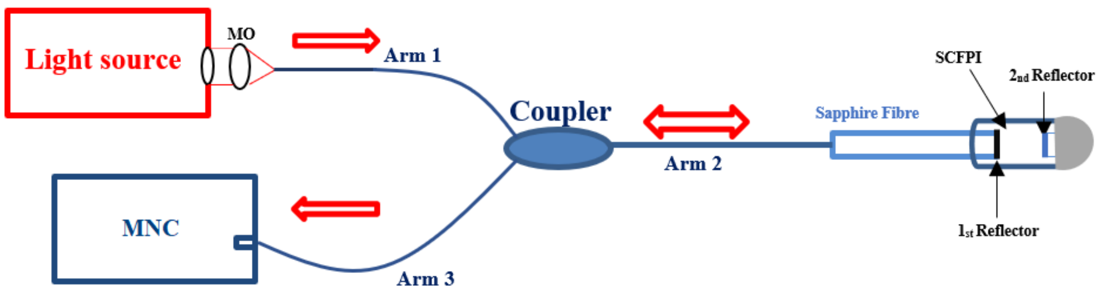

Figure 6.8. Coupler-based FPI system

In the splitter-based FPI system, a beam splitter was used instead of fibre coupler to split the transmission and reflection light. A 50R optical beam splitter plate from *Design Optics*, a *RS* 850 cube beam splitter, a BP145 pellicle beam splitter form *Thorlab* were selected. The first design of the splitter-based FPI was shown in Fig. 6.9 (a). In the system, a beam splitter was positioned in the front of the lamp; a part of light transmits through the beam splitter and is coupled into the straight sapphire fibre by a MO; then, same as the coupler-based system, the light in the sapphire fibre is delivered to the SCFPI sensor head and the reflected back by both reflectors; the reflected light is then transmitted to the surface of the beam splitter through the MO, which is then reflected onto a lens and focused into the input slits of the MNC; lastly, the reflected light is analysed by the MNC. The second design of the splitter-based FPI system was shown in Fig. 6.9 (b). Compared with the former design, the MO was positioned between light source and the beam splitter. In this way the reflected light from the sensor can be directly transmitted to the beam splitter, avoiding the light loss created by the MO due to scattering and reflection on the its surface.

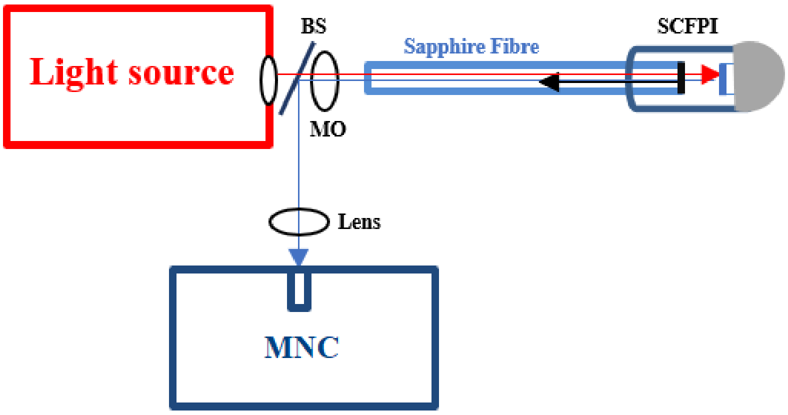

Fig. 6.9. (a) First Splitter-based FPI system design

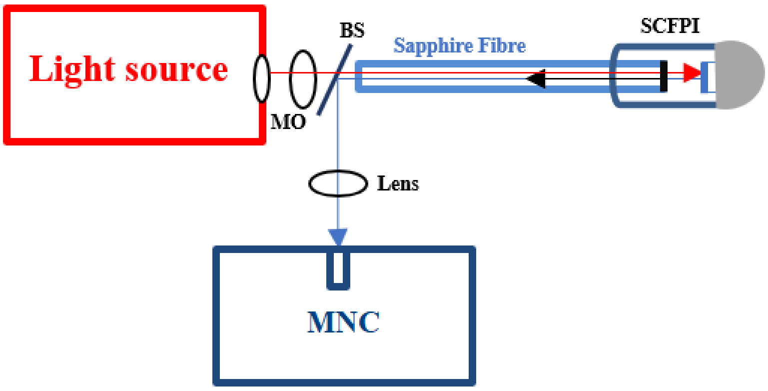

Figure 6.9. (b) Second splitter-based FPI system design

6.2.2 Tests on system components

6.2.2.1 Coupler-based FPI system

In the test of coupler-based FPI system, two main challenges arose. The first challenge is the connection issue between the fibre coupler arm and sapphire fibre. As is shown in Fig. 6.10, originally, the desired reflections should come from only two sources, one is the 1st reflector which is the end of the straight fibre in the capillary, and the other is the 2nd reflector which is the inner surface of the capillary. Due to the fact that the end of the coupler arm 2 was directly connected to the end of the sapphire fibre without any fibre bonding techniques, these two ends also acted as the 3rd and 4th reflectors in the system. Therefore, the reflected lights from the 3rd and 4th reflectors, as well as 1st and 2nd reflectors, are all transmitted to the MNC. However, the reflections from 3rd and 4th reflector can become large interference or noise signals which can easily influence or change the reflection/interference spectrum generated by the 1st and 2nd reflectors of SCFPI, making study of the signal coming only from the SCFPI sensor unachievable. To solve this issue, the fusion splice technique, which is widely used in the different FPI studies, can be applied to combine the core of coupler fibre and sapphire fibre together to eliminate any reflections from fibre ends at the connection point. Originally, the fusion splice technique was used for combining conventional fibres with similar core diameter [6.11], however, in the recent decades, it has been used to combine conventional fibres to fibres with different core diameters and different materials [6.4, 6.9, 6.12], including SCFs. Besides, anti-reflective (AR) coating or connectors could also be used for eliminating the reflection from the ends of coupler fibre and sapphire fibre.

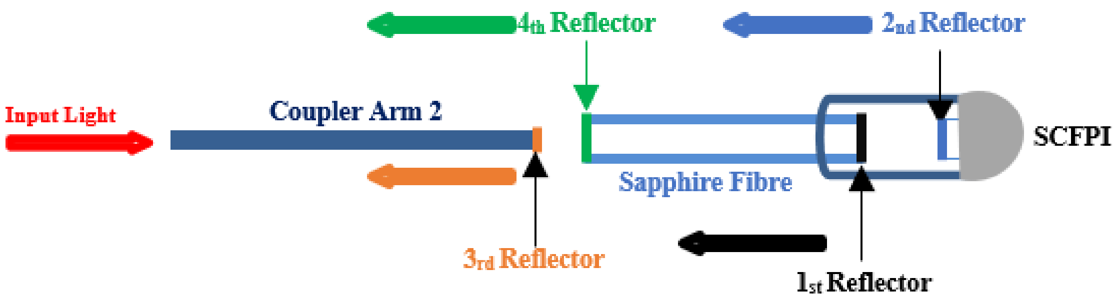

Figure 6.10. Schematic of the 4 reflectors in the coupler-based system

The second challenge was found in the investigation of testing the influence of each reflector on the entire reflected light. To discuss this issue clearly, the number of the reflectors are renamed from left to right, which is also the order of reflections happened in practice, as shown in Fig. 6.11 below. For example, when the light is transmitted from the coupler to the sapphire fibre, the first surface that is regarded as the reflector is the fibre end of the coupler arm 2, therefore it is named 1st reflector, and so on.

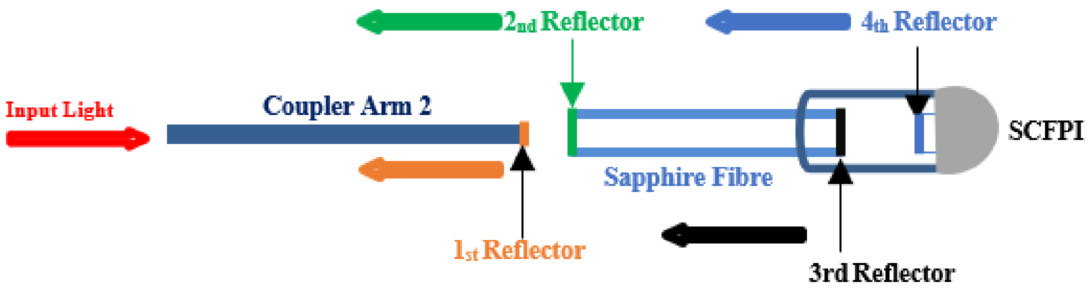

Figure 6.11. Names of the 4 reflectors

Since the reflections from both 1st reflector and 2nd reflector is regarded as the disturbance for the sensing system, it is necessary to test the influence of their reflections on the entire reflected signal. To begin with, only the 1st reflector was tested without adding the sapphire fibre and SCFPI, shown in Fig. 6.12.

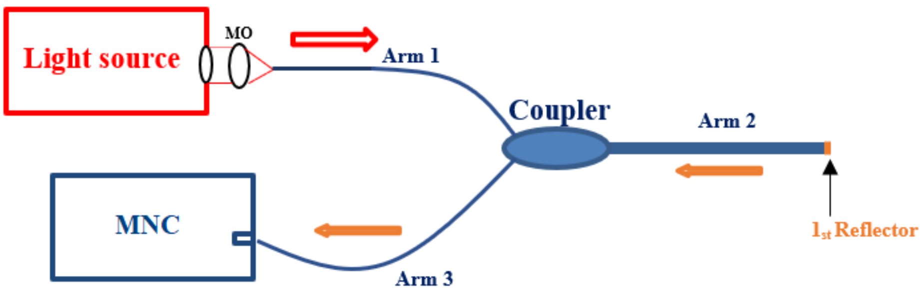

Figure 6.12. Testing system for the 1st reflector

At first, no signal but only noise can be detected by the MNC as the reflected light at the 1st reflector to MNC is small. Compared with sapphire fibres fabricated by LHPG method, the diameter of coupler fibre core is quite small (105 μm), so limited light from the white light lamp can be coupled into coupler arm 1; also, at the end of fibre arm 2, only a small part of the light can be reflected back with a large amount of light lost in the environment; plus, at the connection point of three arms, only half of the reflected light in arm 2 can be delivered to arm 3 due to 50:50 split ratio of the coupler; lastly, since monochromator receives signals with slits instead of fibre connectors, some light is lost to the environment whether by directly putting fibre end towards the slits or using lenses for focusing. To solve this problem, the test was conducted in the extremely dark environment, and the whole system was covered by a black enclosure to prevent disturbance from scattered light from the light source and computer monitors. In this dark environment, the weak reflection from the 1st reflector can be detected, plotted in Fig. 6.13. Although the signal is small (with maximum intensity of

0.85 at 950 nm) and the spectrum has lots of noise compared with Fig. 6.6. (a) (with maximum intensity 3.8 of at 950 nm), it shows the basic shape of the spectrum.

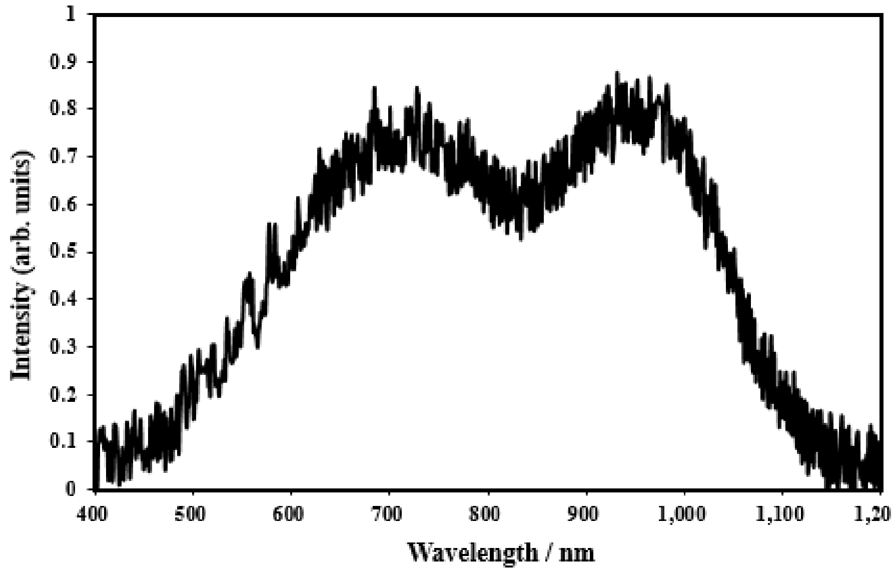

Figure 6.13. Spectrum of the reflected signal from 1st reflector

As the spectrum of reflected light from 1$_{st}$ reflector was obtained, the next step is to test the spectrum when the sapphire fibre is added to the system. A straight sapphire fibre (7 cm length, 380 µm diameter, both side polished to 1 µm) was positioned and aligned to the end of the coupler arm 2. The new testing system is shown Fig. 6.14, it can be seen that when the sapphire fibre was added to the system, the reflected signal delivered to the MNC is a combination of reflections from 3 reflectors, 1st, 2nd and 3rd reflectors. Without changing any other components or setting, the reflected light was scanned again, presented in Fig. 6.15 with the comparison of the reflection spectrum of the 1st reflector (Fig. 6.12).

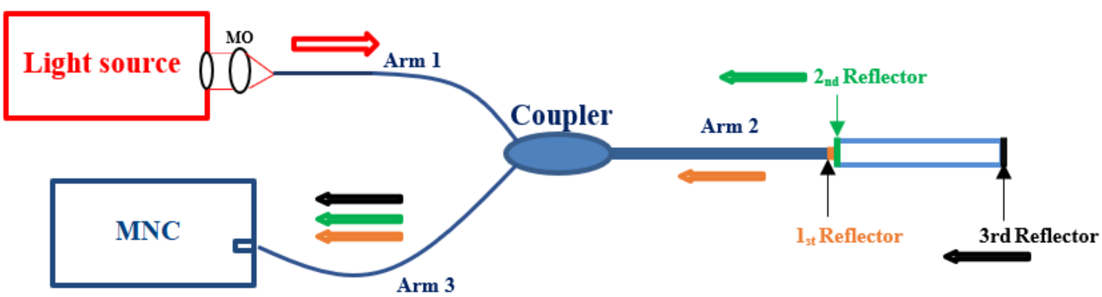

Figure 6.14. Testing system for 1st reflector and sapphire fibre (2nd and 3rd reflector)

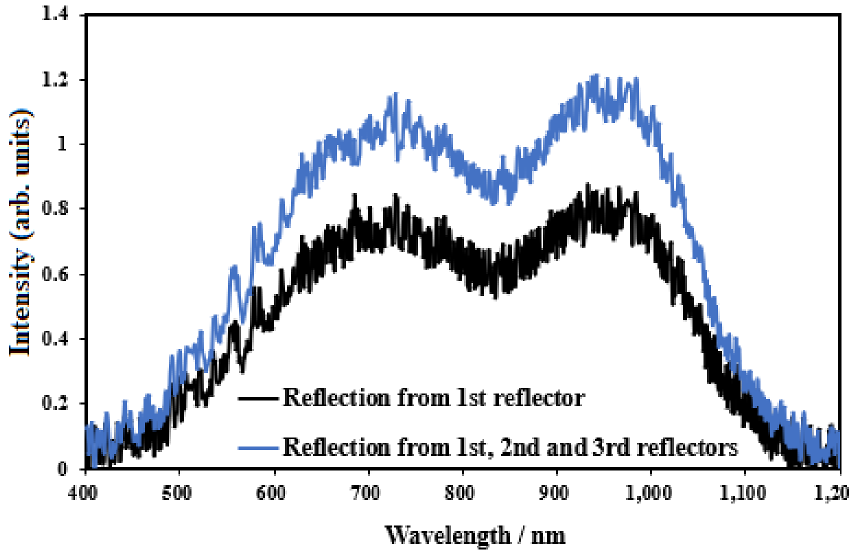

Figure 6.15. Spectra comparison between the reflection from only 1st reflector (black) and reflection from 1st, 2nd and 3rd reflectors (blue)

As expected, although the signal is still small, the amplitude of the spectrum of reflections from three reflectors was increased compared with the spectrum of the reflection only from the 1st reflector. This is because the part of light that originally lost at the surface of the 1st reflector had been reflected back by the 2nd and 3rd reflectors when the sapphire fibre was added. However, as this amplitude increase was generated by both 2nd and 3rd reflectors, to test the influence of the 2nd reflector only, the systems in Fig. 6.16 was designed and built. As is illustrated in Fig. 6.16, two methods were both applied to stop light reflecting back at the 3rd reflector. The first method in Fig. 6.16 (a) is to immerse the fibre end into a high index (1.78 RI) oil. A length of glass capillary was used to fill the oil and the silicone was used to seal each end of the capillary. The second method shown in Fig. 6.16 (b) is to break the polished end of the fibre (3rd reflector), creating a very irregular and random shaped end. Both methods can effectively stop the fibre end reflecting light back. With no other components and system settings changed, the both systems were scanned. Theoretically, the spectrum amplitude of the reflection from 1st and 2nd reflectors should be smaller than that of the reflection from three reflectors (1st, 2nd, and 3rd reflectors), but larger than that of the reflection from one reflector (1st reflector). However, the result shows that the spectrum of the reflection of 1st and 2nd reflectors is exactly same as the spectrum of reflection from 1st, 2nd and 3rd reflectors in former test, with no change in the amplitude or the shape of the spectrum, as shown in Fig. 6.17 below.

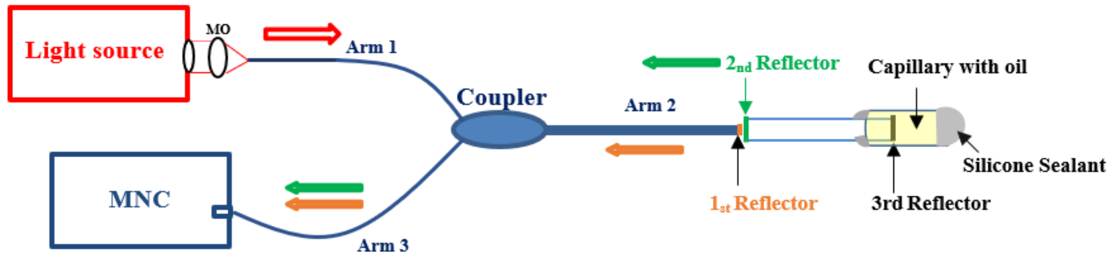

Figure 6.16. (a) Testing systems for 1st and 2nd reflectors: index oil method

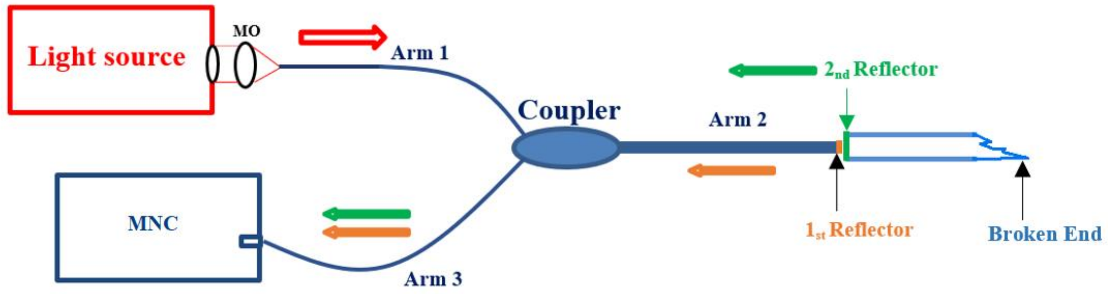

(b)

Fig. 6.16. (b) Testing systems for 1st and 2nd reflectors: broken end method

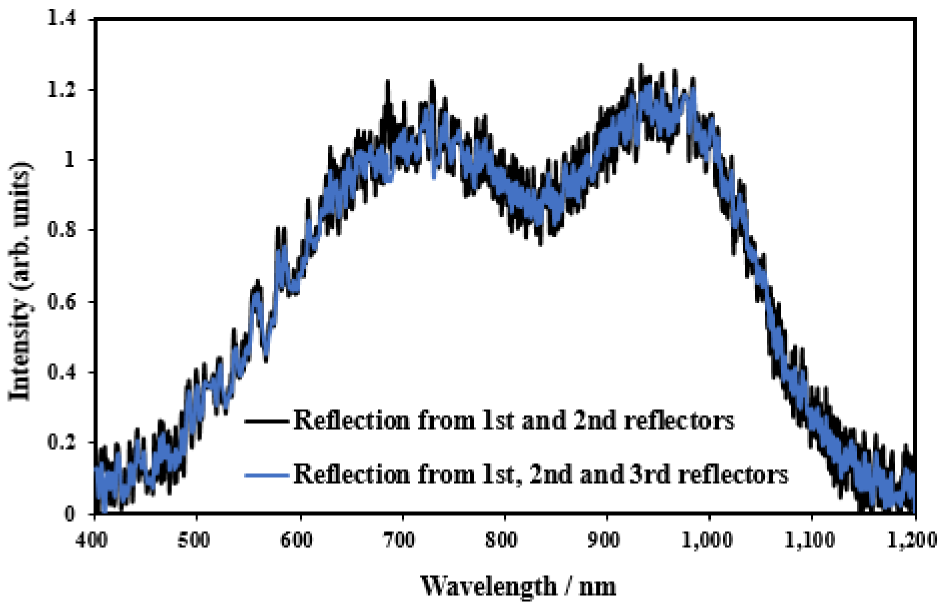

Figure 6.17. Spectra comparison between the reflection from 1st and 2nd reflectors (black) and reflection from 1st, 2nd and 3rd reflector (blue).

By comparing the result in Fig. 6.15 and Fig. 6.17, it can be found that there was very little reflection coming from the 3rd reflector so that the reflection spectrum of 1st and 2nd reflectors is the same as that from 1st, 2nd and 3rd reflector; if not, the amplitude of the reflection spectrum of 1st and 2nd reflectors will be smaller than that of the 3 reflectors due to the insufficient 3rd reflector. This caused an issue because if the reflection from 3rd reflector is too small to make any difference on the spectrum; it is not possible to detect the reflection from the 4th reflector as the light transmitted to 4th reflector becomes even smaller than that to the 3rd reflector. Although studying the behaviour of the reflections from 3rd and 4th reflector is the main target, their reflections were too small to be detected by this system. Thus, the reflection information of them cannot be properly studied whether the interference was generated or not.

The cause of this issue can be analysed from two aspects. On the one hand, the overall signal transmitting in the system was small due to the small core diameter, loss along the sapphire fibre, coupling between light source and coupler, and coupler and MNC; thus, after the small amount of light being reflected twice at the first two reflectors, the transmitted light reached the 3rd and 4th reflectors was too small to be detected by the system, let alone their reflection lights. On the other hand, the large core cross section area difference between the coupler fibre (8.654×10^3 μm^2) and the sapphire fibre (1.13×10^5 μm^2) is likely to have caused the majority of reflection light (from the 3rd and 4th reflectors) lost to the environment. For the reflection at 2nd reflector, the influence is not that large since the diameter of the 2nd reflector is larger than the 1st reflector. But for 3rd and 4th reflectors, whose reflection lights are transmitted back along the sapphire fibre and picked up by the coupler fibre with a smaller core diameter, this influence can be dominant.

As the light reflected by the 4th reflector had not been received and analysed, the quality of the inner surface of the SCFPI sensor after melt bonding process in crystal insertion method is unknown. To test the quality of the inner surface fabricated, the coupler arm 2 was directly inserted to the capillary without the sapphire fibre, shown in Fig. 6.18. The spectrum was scanned twice with and without the SCFPI capillary, plotted in Fig. 6.19. The result of this test is similar as that in Fig. 6.15, the spectrum of reflection signal with the capillary has the larger amplitude than that without the capillary, indicating the 4th reflector fabricated with crystal insertion method can be regarded as an adequate “mirror” in the FPI sensor.

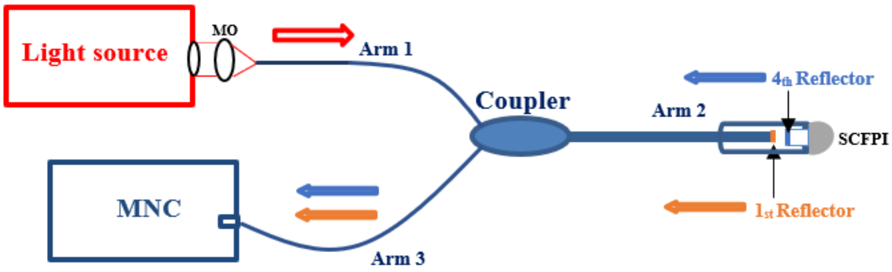

Figure 6.18. Testing systems for 4th reflector

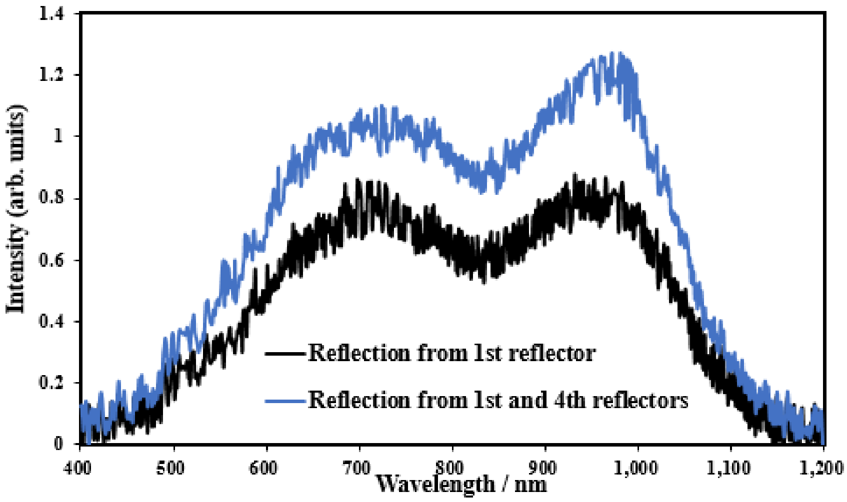

Figure 6.19. Spectra comparison between the reflection from 1st reflector (black) and reflections from 1st and 4th reflectors (blue).

6.2.2.2 Splitter-based FPI system

In the investigation of the two proposed splitter-based FPI systems, two main issues have occurred for both systems. The first issue is a light scattering problem. As the two reflectors in the SCFPI sensor have a small diameter (300-400 µm), the reflected light signal from these surfaces is small as well. Therefore, eliminating light noise in the testing environment is crucial. However, unlike coupler-based FPI system, which transmits light within the fibre and can be covered with an enclosure to work in an extremely dark environment, the components in splitter-based FPI system are all in the same environment and white light is transmitted by lenses and the splitter. As the input signal to the MNC is through lenses and MNC slits, scattered light from every object is coupled into the slits through the lenses, which generates a large amount noise and makes the small reflected signal from SCFPI undetectable. This caused much unwanted light being coupled into the MNC, for example, the scattering light from MO, beam splitter, sample, PC monitor and last but not least the light source, as shown with the purple dashed lines in Fig. 6.20.

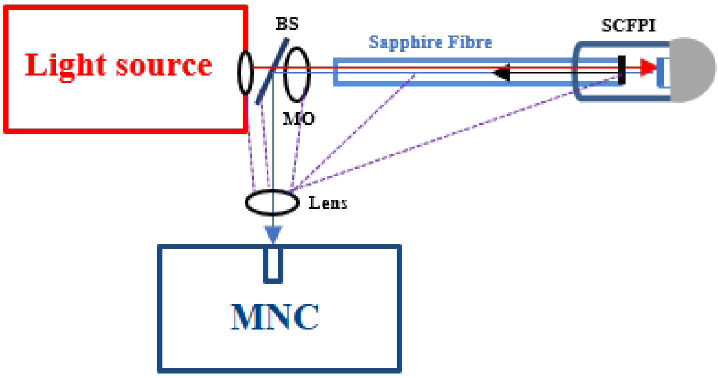

Figure 6.20. Illustration of the scattering light in the splitter-based FPI system

The other issue of the splitter-based FPI system comes from the beam splitter. As the MO, which has a very short focal length (~3 mm for ×20 MO), was used to couple the white light into the sapphire fibre, positioning beam splitter between components with the right angle can be difficult as the size of the beam splitters are usually large, such as the cube beam splitter and plate splitter. Only the pellicle beam can be used in this case. However, the using the such thin splitter to split white light can cause interference signal pattern in 400 to 1200 nm. In the tests, the BP145 pellicle beam splitter was used and the output spectrum was shown in Fig. 6.21.

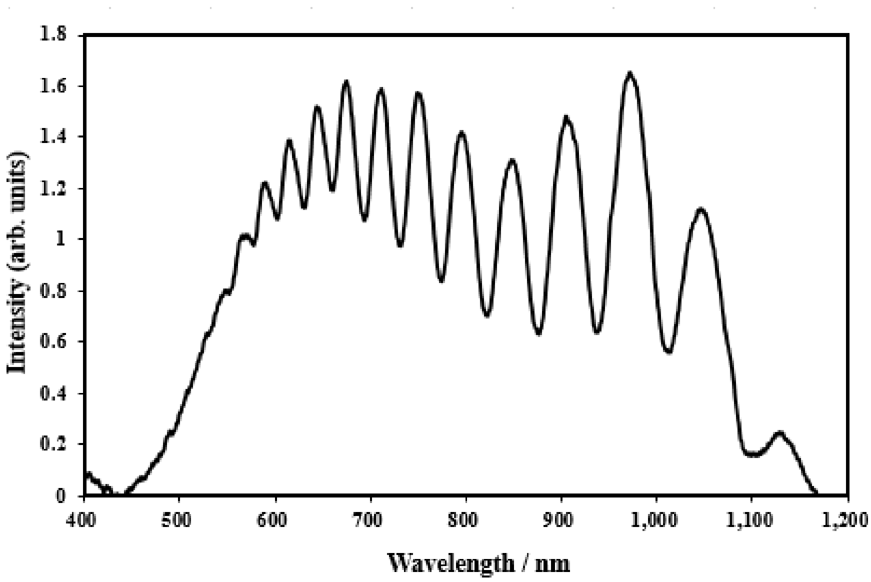

Figure 6.21. Output spectrum of using pellicle beam splitter

The likely cause of the interference signal comes from the pellicle beam splitter itself. However, the interference signal created by the pellicle beam splitter is evidently much larger than the reflection from sensor reflectors due to its larger reflecting surface. This prevents the detection of the only reflected light from the sensor reflectors.

6.2.3 Laser reflection test

Due to the issues in the two FPI testing systems, to prevent the scattering loss, a He-Ne laser-based system was built to study the reflections and interference from the SCFPI, shown in Fig. 6.22.

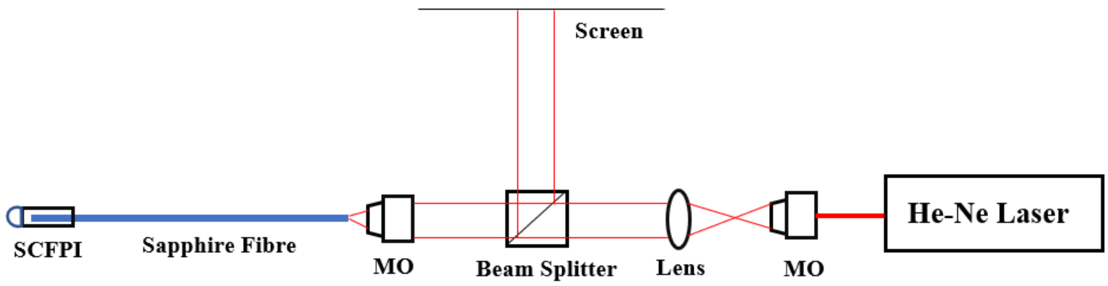

Figure 6.22. The Initial interference test system

As is shown, the He-Ne laser beam was first expanded by a MO and delivered to a beam splitter through a lens. The transmitted light from beam splitter was then coupled to a commercial sapphire fibre (length of 15 cm and diameter of 380 µm) by a MO. One end of the sapphire fibre was inserted in the SCFPI cap with two reflectors aligned parallelly by the capillary. Ideally, when the He-Ne laser is on, the light will transmit to the two reflectors of SCFPI through beam guiding optics and sapphire fibre, and then reflects back and transmits to the screen through the MO and beam splitter, presenting a magnified image of the fibre end including a large area with the shape of fibre end and a small bright spot in the middle on the screen in the far field; the large spot is the reflection from two reflectors of the BCFPI and the small spot is the reflection from the input end of the sapphire fibre, However, in practice, the larger reflection spot was displayed, only the bright small reflection spot was shown on the screen. The illustration of the expected result and practical result was shown in Fig. 6.23. The cause for this result is most likely due to the amount of light reflected by the two the reflectors of SCFPI being quite small and largely lost to the environment during the back-transmission along the sapphire fibre. To further verify this cause, the FPI capillary was removed from the fibre end and an optical flat mirror was positioned by a 3-axis aligner against the fibre end to provide the stronger reflection, as illustrated in Fig. 6.24.

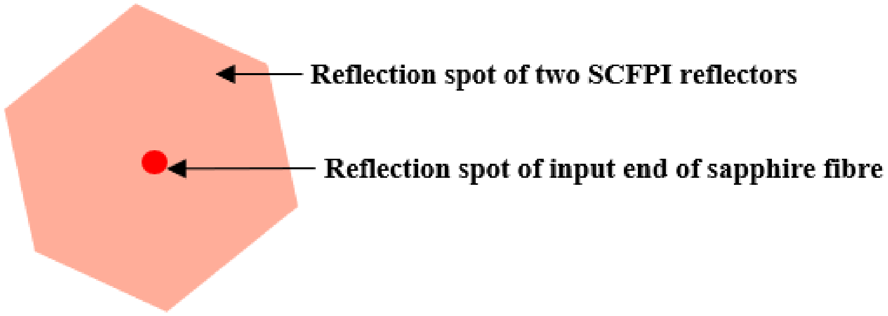

Figure 6.23. (a) Expected result on the screen

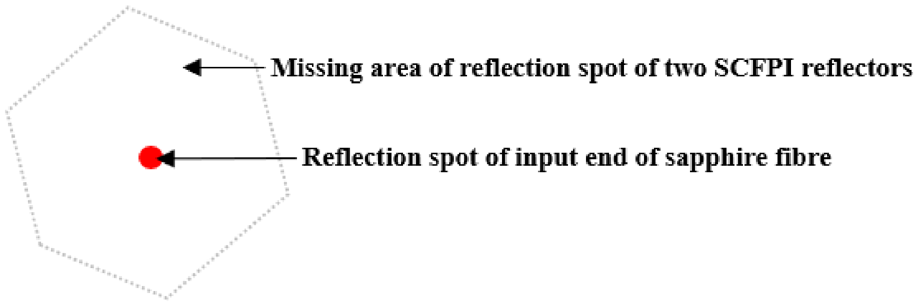

Fig. 6.23. (b) Practical result on the screen

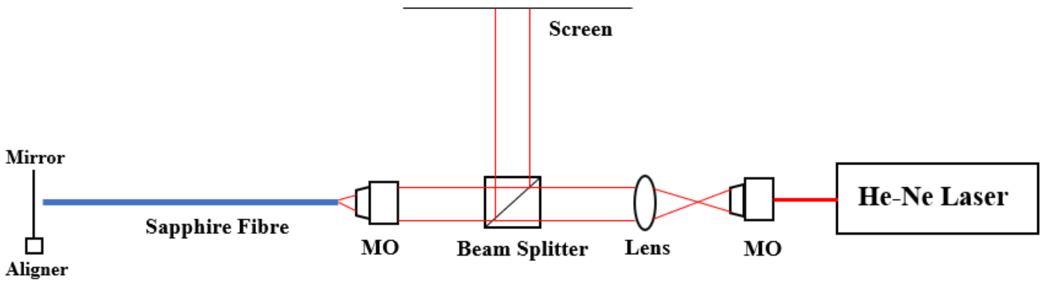

Figure 6.24. Reflection testing system with mirror

With the mirror added into the system, a stronger reflection should be generated, reflected back, and eventually projected to the screen. As expected, when the He-Ne laser was on, the large spot of reflected light was presented on the screen in a shape of the end of the sapphire fibre, shown in Fig. 6.25. By changing the relative angle and distance between the mirror and the end of sapphire fibre, the brightness and the pattern of the reflection light spot can be changed.

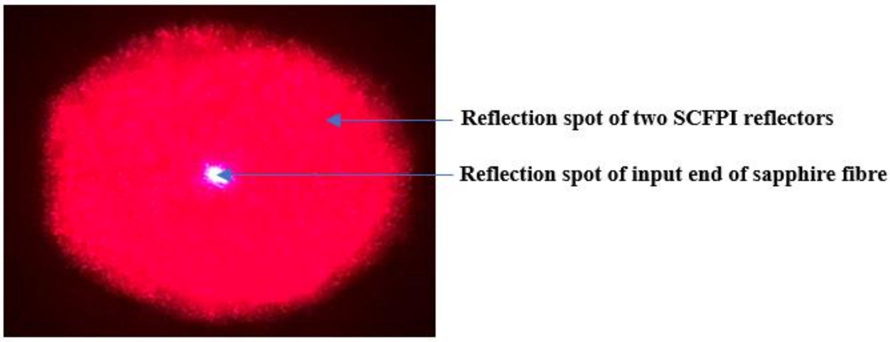

Figure 6.25. The reflection spots on the screen

From this experiment, it can be seen that even when a laser source was used, the reflection signal of the SCFPI is still small. Besides, because of the unclad and long length of the sapphire fibre, the small amount of reflection light generated by the SCFPI was lost during the back-transmission loss. This can be also observed from the outside of the sapphire fibre when as shown in Fig. 6.26, where the entire sapphire fibre is illuminated red due to scattering losses of the laser beam.

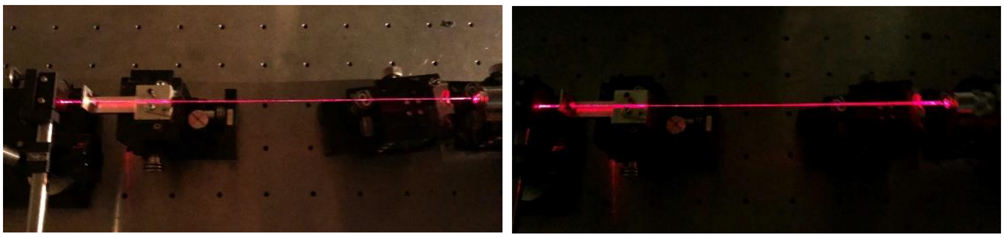

(a) (b)

Figure 6.26. The scattering effect of sapphire fibre while transmitting He-Ne laser beam in (a) bright environment (b) dark environment.

6.2.4 Improvements and future work

With the result of above initial tests on different SCFPI systems, the requirement of an effective FPI sensing system was concluded, which can be applied to build an improved system in the future work. As the small reflection signal from SCFPI was the key characteristic to be considered in the system build, the new system should be focused on increasing the reflection signal as well as avoiding the signal loss during the transmission. A high-power white light source or tuneable diode laser can be used as the light source to provide an efficient input signal. The coupler-based FPI system should be applied rather than a beam-splitter based FPI system as the light can be transmitted in the fibres with cladding and coating, decreasing loss in transmission. A multimode fibre coupler with larger core diameter (200-300 µm) is preferred for coupling more light into the system. A short length of sapphire fibre (or a long length of cladded sapphire fibre) with the similar diameter as the coupler can be used to connect with the coupler arm to reduce the loss of the reflected signals. To bond the coupler and sapphire fibre, fusion splicing or anti-reflection coating should be used to avoid any unwanted reflection signals. Lastly, an optical spectrum analyser could be connected to the coupler with a fibre connector and used to detect the small reflection signal. With these improvements, the noise and light loss in the system could be reduced dramatically. In this way, reflections from two reflectors of SCFPI could be detected and studied for a suitable interference pattern.

In addition to the above work on the sensing structure and equipment, the interference pattern generation process and data analysis method must also be considered to develop the SCFPI as a working sensor. To generate the interference pattern, a precision aligner/autocollimator (with a minimum pitch between 50 and 100 µm) needs to be used to control the distance between two reflectors. Once the interference pattern is generated, the sapphire fibre can be bonded to the capillary using the CO_2 laser or a high-temperature adhesive. To analyse the change of interference spectra, the optical path difference (OPD) of the interference spectra can be used as the temperature indicator for the FPI sensor, which can be achieved by fast Fourier transform (FFT) of the spectral fringes, fully described in [6.10, 6.11]. Finally, by determining the relationship between OPD and temperature change, the SCFPI temperature sensor can be built.

6.3 References to Chapter 6

[6.1] R. Dils, "High-temperature optical fiber thermometer," J. Appl. Phys., vol. 54, pp. 1198-1202, 1983.

[6.2] X. Hao, S. Tao and H. Zhou, "Research on Characteristic Parameter of Ta-Zro2 Fiber Blackbody Cavity Temperature Sensor," International Journal of Signal Processing, vol. 9, pp. 287-296, 2016.

[6.3] H. Chen, "Review and perspective: Sapphire optical fiber cladding development for harsh environment sensing," Appl. Phys., vol. 5, pp. 1-19, 2017.

[6.4] S. Bera and P. Ohodnicki, "Fabrication and evaluation of sapphire fiber cladding via magnesium aluminate spinel sol-gel based approaches," Proc. SPIE 11000, Fiber Optic Sensors and Applications XVI, 2019. doi: 10.1117/12.2518506

[6.5] G. Zhao and X. Tong, "research progress and development of sapphire fibre sensor," sensors and transducers, vol. 174, pp. 8-13, 2014.

[6.6] B. Li, "Study of high-temperature sensor based on black vacuum," PhD thesis, Wuhan University of Technology, 2006.

[6.7] T. Cui, X. Hao and H. Zhou, "Design of the fiber-optic temperature sensor based on colorimetry," *Measurement and Testing Technology*, vol. 37, pp. 33-35, 2010.

[6.8] G. Ivanov, "Fabry-Perot sapphire temperature sensor for use in Coal Gasification," PhD thesis, Virginia Polytechnic Institute and State University, 2011.

[6.9] J. Wang, B. Dong, E. Lally and A. Wang, "Multiplexed high temperature sensing with sapphire fiber air gap-based extrinsic Fabry–Perot interferometers," Optics Letters, vol. 35, pp. 619-620, 2010.

[6.10] Y. Zhu and Z. Huang, "Sapphire-fiber-based white-light interferometric sensor for high-temperature measurements," Optics Letters, vol. 30, pp. 711-713, 2005.

[6.11] M. Shao, "Hybrid long-period fiber grating with multimode fiber core for refractive index measurement," Chinese Phys. Lett., vol. 34, pp. 205-209, 2017.

[6.12] H. Cheng, "Growth and characterisation of the single crystal fibre for sensing applications," PhD thesis, University of Glasgow, 2001.

[6.13] F. Shen, A. Wang, "Frequency-estimation-based signal-processing algorithm for white-light optical fibre Fabry-Perot interferometer," *Applied Optics*, vol. 44, pp. 5206-5214, 2005.

Chapter 7 – Long-period Sapphire Fibre Grating Sensor

Chapter 7 – Long-period Sapphire Fibre Grating Sensor

7.1 Design and Setup of Experiment System

The design and components of the LPSFG testing system are the same as the transmission testing system in Fig. 6.5 of **Chapter 6** with only testing fibre changed, which is recalled in Fig. 7.1 below. It consists of four main parts: a light source, an optical transmission system, a sensing element, and a signal analysis system. As the cut-off wavelength of the silicon photodetector in the signal analysis system is 1200 nm, the working wavelength of this broadband light in the experiment ranges from 400 to 1200 nm. Compared to a laser light source, a broadband light source is not only more economical, but also, the highly multimode sapphire fibres used in these experiments are suitable to receive broadband light as they have large unclad cores (~350 µm in diameter) [7.1, 7.2]. More importantly, a broadband light source produces light over a wider range of wavelengths than a laser, which allows the investigation of the resonant wavelength (RW) across a wider range of wavelength. The light signal from the light source was coupled into the sensing element through the optical transmission system, as explained in **Chapter 3**, it then interacts with the LPG, leading to a change in the output spectrum. By comparing the original light source spectrum to the output spectrum, the performance of the LPSFG can be studied.

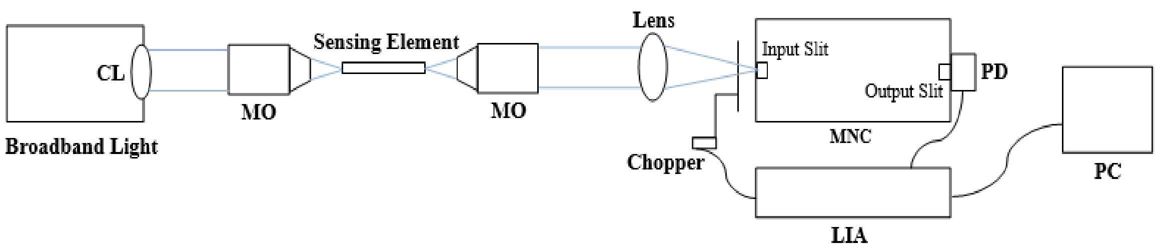

Figure 7.1. Schematic of LPSFG experiment system

As for preparing the sensing element, the most significant procedure is to clad the fibre grating. According to the basic LPG formula, Eq. (4) in **Chapter 3**, the RW depends upon grating period and the difference between the effective index of fibre core and cladding. In LPG studies, the effective index of core and cladding is often estimated to be equal to their respective refractive index (RI) [7.5, 7.6, 7.7, 7.8]; due to the unclad nature and high RI (1.760) of the sapphire fibres; if the experiment is conducted in the air (RI of 1), the difference between the RI of the sapphire core and the air cladding is relatively large compared with conventional fibres with claddings; since the period is fixed for a fibre grating, this large difference of RI makes the corresponding RW appear only at very long wavelengths (over 76,000 nm if period is 100 μm), which is outside the wavelengths that the system can generate and detect. Therefore, of course, locating the RW in the wavelength region produced by the light source is a precondition of the LPG study. Thus, the bare sapphire fibre needs to be clad with a higher RI material than air. To achieve this, for the purpose of grating characterisation, liquids with different RI values were used to clad the grating fibre. Incorporating this, the grating fibre was put into a small capillary filled with index matching liquid, leaving the two ends of the fibre protruding outside the capillary to facilitate light coupling. The fabrication of the two designs was carried out in the lab, shown in Fig. 7.2.

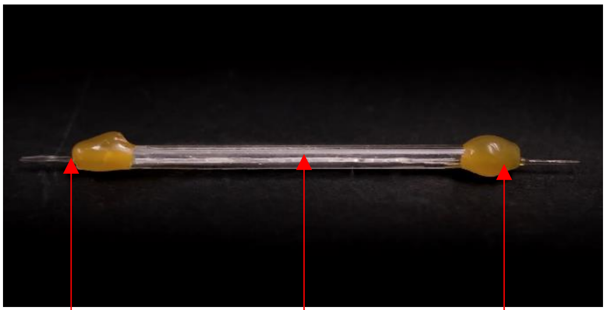

Sapphire Fibre

Glass Capillary

Wax Quartz

(a)

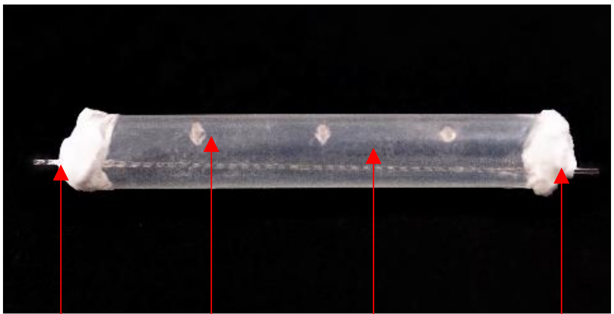

Sapphire Fibre

Syringe Barrel

Silicone

Oil Inlet Hole

(b)

Figure 7.2. Fabrications of the sensing element: (a) the original wax and glass capillary design; (b) the improved silicone and syringe barrel design;

As shown in Fig. 7.2 (a), the original design was to use a length of 1 mm diameter glass capillary as a small chamber; the prepared fibre was set inside the capillary and secured by melting a piece of quartz wax at one end; the glass capillary was then filled with index liquid at the other end using a syringe. After that, the other end was sealed by wax as well. There were found to be three drawbacks to this design; firstly, the wax needs to be melted to seal the glass capillary. When heating the wax, the heat is also transferred to the index liquid inside the capillary, this can change the RI permanently for some materials, and also the melted wax can be a contaminant to the index liquid. Secondly, the syringe needle needs to be long enough (at least 3.5 cm) and thin enough (at most 350 μm) to have the liquid fill the glass capillary from its deepest point. Otherwise, the liquid became stuck in the middle of the capillary with many trapped air bubbles. Lastly, using this system it is inconvenient to perform optical tests both with and without index liquid; when the capillary needs to be filled, the sample has to be moved from the experiment bench, which unavoidably alters the original alignment between optics and sample, introducing unwanted variables in the experiment; furthermore, the high index liquid is not reusable after handling with wax and heating a few times.

To solve these problems, an improved design was implemented, as shown in Fig. 7.2 (b). In this design, the 4 mm diameter syringe barrel was cut from a syringe and used as the fibre surround instead of the glass capillary, and silicone was used instead of wax as the sealant. The syringe barrel is made of polypropylene, a material that is insoluble in water and has a stable chemical property. Unlike wax, silicone can be used to seal the syringe barrel without a heating process, which avoids the index liquid reacting to higher temperatures. To remove the silicone, a simple mechanical method can be applied with the help of tweezers, the removed silicone material still in one piece: it did not dissolve or react with the high index liquid, helping to preserve liquid purity and allow it to be reused. Three parallel holes were made in the syringe barrel. This facilitated adding liquid through the holes using a syringe without moving the sample, providing a better comparison of the spectra with and without the high index liquid in place. In addition, with a larger diameter tube and the vent holes, the trapped air in the tube during the filling process can be easily released, avoiding unwanted air bubbles being trapped inside the tube. This new design has completely solved the problems encountered in the previous design and became the basis of all subsequent experiments.

7.2 Long-period Sapphire Fibre Grating Experiments

As the experimental system had been designed and built, LPSFG experiments were conducted to examine grating behavioural response. The experiments were divided into three main categories. To begin, some initial grating measurements were taken as a reference and comparison groups. Then, high RI liquid was used to clad the LPSFG to get the RW in the detectable range of the light source (400 nm to 1200 nm). Lastly, further experiments were conducted to study the response of the RW to variations in the cladding index using a range of discrete RI steps.

7.2.1 LPSFG initial experiments

7.2.1.1 Experiments

The expected response of the LPSFG is the appearance of RW coupling loss in the transmission spectrum. This presents itself in the form of a drop in the transmission spectrum at certain specific wavelengths [7.7, 7.8, 7.9], which illustrates that coupling has occurred between core and cladding modes. Therefore, studying the spectral shape of the light output is important for investigating the grating effect. Two initial experiments were conducted for the purposes of testing the experimental system and providing a reference spectrum.

The first experiment was to obtain the spectrum of light passing through the bare grating with no cladding; by comparing this spectrum with the original source spectrum, the influence of un-clad grating on the original spectrum could be studied. The emission spectrum of the light source was scanned first using the optical arrangement discussed above but without the grating fibre in the system; after that, with the same settings (LIA sensitivity of 3 mv and time constant of 1 s) and optics in Fig. 7.1, the spectrum was scanned with a grating fibre added into the system, positioned between the two × 20 microscopes shown in the LPSFG experimental system. The structure of the grating fibre is schematically shown in Fig. 7.3, which had a 3.5 cm grating length, 0.01 FAM and 90 μm period grating section in the middle, and two sections, 1 cm in length, 350 μm in diameter of straight growth at each end of the fibre grating. The two ends of the fibre had been polished to 1μm to provide adequate coupling.

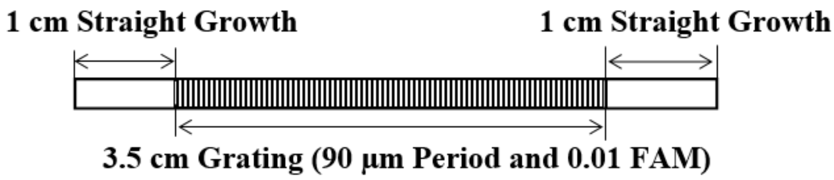

(a)

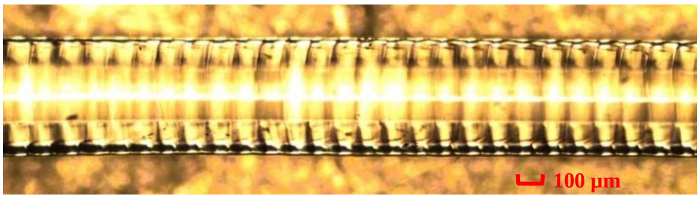

(b)

Figure 7.3. Structure of the grating fibre: (a) schematic of grating fibre; (b) microscope image of the grating section.

The second experiment was to use refractive index liquids to clad the grating fibre. The purpose was to investigate the influence of the index liquids on the spectrum of the grating fibre. The two index liquids used were cinnamon oil with an RI of 1.53 and cassia oil with an RI of 1.60; relatively speaking, these two oils have high RI values among general liquids; however, the values were still low compared with the RI of single-crystal sapphire (1.76). To provide a clear comparison with the bare grating, the same 90 µm period grating fibre was used in the system. The grating fibre was put into the index chamber first without any index liquid, after scanning the spectrum, the cinnamon oil was then carefully added into the chamber without moving other setups, and the spectrum was scanned again for a comparison. Similarly, the output spectra were scanned and compared before and after adding the cassia oil. The structure of the sensing element in the experiment is shown in Fig. 7.4 below.

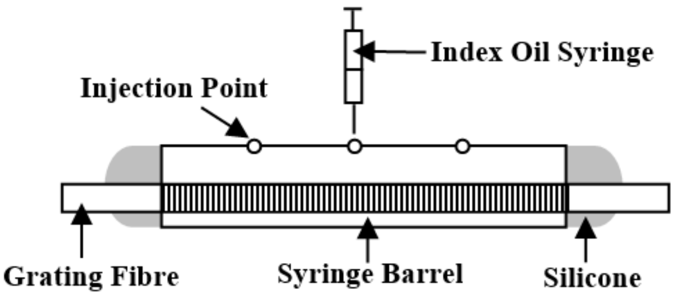

Figure 7.4. Structure of the sensing element

7.2.1.2 Results and Discussion

The spectra of the original light source and the 90 µm bare grating were measured, as plotted in Fig. 7.5. As can be seen from Fig. 7.5, the spectrum of the original light source has two peaks, which are at 750 nm and 950 nm. Compared with the spectrum of the original light source, the spectrum of the bare grating has the same shape and location of peaks, with the only difference being in the value of amplitude. The overall drop of amplitude in the spectrum of the bare grating is due to two main reasons. The first reason is the coupling loss between the optics and the fibre; in practice, as the coupling efficiency of the optics and the grating fibre cannot be 100%, some light will not be coupled into the fibre and lost to the environment. The second reason is the fibre loss due to the unclad nature of the sapphire fibre, which increases the amount of light that scatters to the environment and causes loss [7.10]. However, apart from the overall voltage drop of the entire spectrum, there were no observed changes to spectrum shape, illustrating that there was no RWs from the grating at these wavelengths. This test indicated that the bare fibre grating does not change the transmission spectrum but could cause light loss due to the coupling and scattering losses. Also, it confirms that due to the large difference between the refractive index of the air and the sapphire, no RW should appear in this region based on basic principle of LPG. The spectrum of the light source can thereafter be used as the reference spectrum for the further studies of gratings.

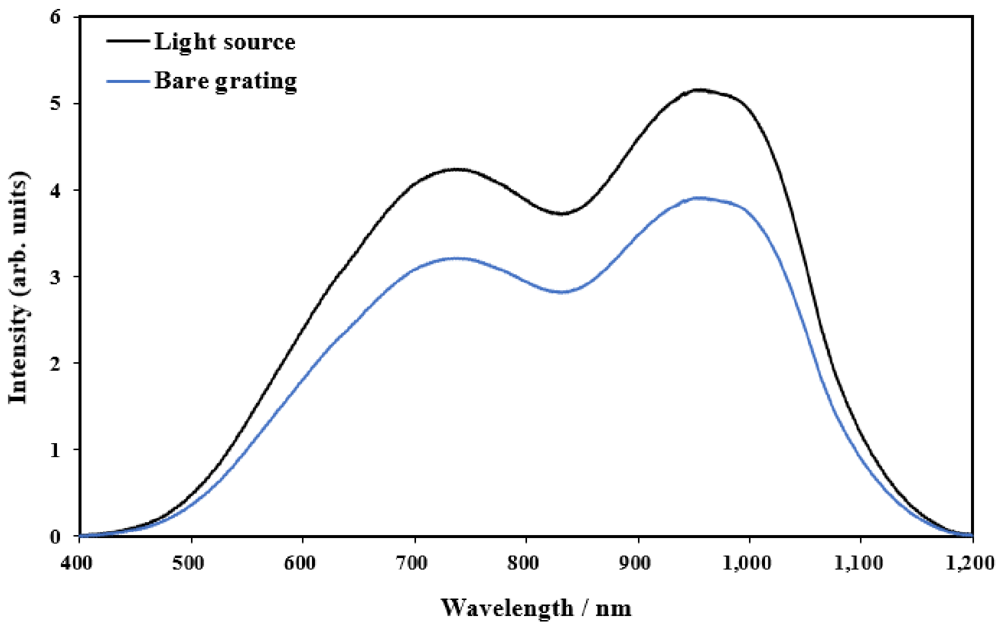

Figure 7.5. Comparison of spectrums of light source and grating fibre

The result of the second experiment is shown in Fig. 7.6. In the figure, the spectrum of the bare grating and spectra of gratings cladded by cinnamon and cassia oil are overlapped. As the shape and amplitude of the three spectra are almost identical at each wavelength, it indicates that there is no sign of resonant coupling in the 400 to 1200 nm waveband even with the addition of the index oil. Again, this agrees the result of the predicted value of RW using the basic LPG formula in Eq. (4), indicating the RW of a 90 μm period grating should not appear in 400 to 1200 nm waveband, but 14000 to 20000 nm when the RI liquids of 1.53 and 1.6 are used as cladding. Since there was no additional significant light loss in the 400 to 1200 nm waveband for the tests, this experiment can also demonstrate the practicality, repeatability and reproducibility of the measurement system used. In order to study the RW appearance in the waveband of the light source (400 to 1200 nm), higher RI liquids or smaller period fibre gratings should be used.

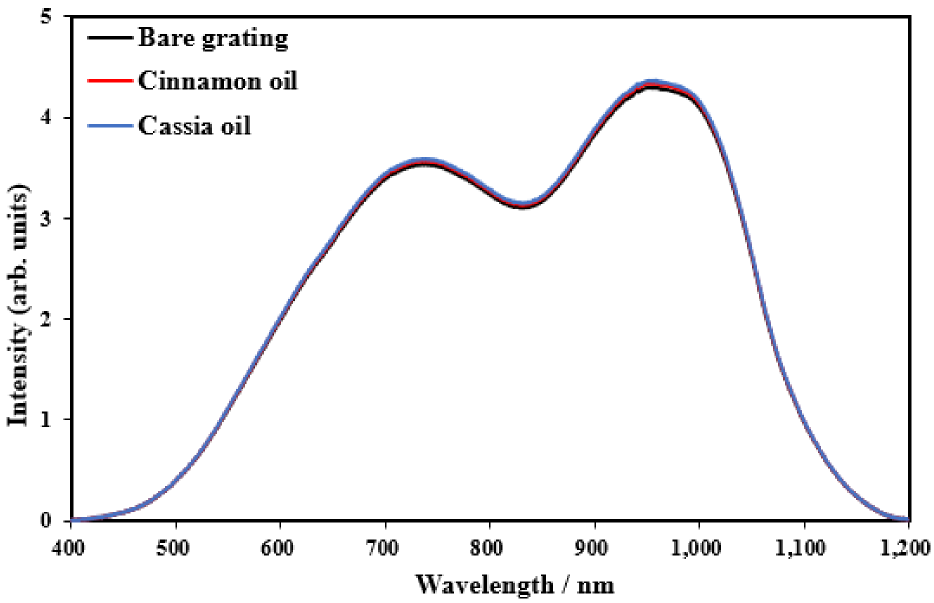

Figure 7.6. Spectra of bare grating and oil-clad grating

7.2.2 LPSFG with cladding of high refractive index

7.2.2.1 Experiments

To demonstrate and assess grating performance and response, higher index liquids from *Cargille* Inc. were used to clad the grating. To allow the RW to appear in 400 to 1200 nm waveband, M series index oil liquids with RI from 1.745 to 1.780, with a step of 0.005 ±0.0002, have been selected as the test cladding to investigate the best result for the cladding in practical use. The experiment setup was the same as previous experiments, the same optical system and grating fibre were used. Index oil with 1.755 RI was used to clad the previous 90 µm grating fibre. Once again, with the same system setting (LIA sensitivity of 3 mv and time constant of 1 s) and optics, the experiment was done in two main steps: first the reference spectrum of output light from the bare grating was scanned without the index oil; then after adding the index oil, the spectrum was scanned again for comparison. According to calculation based on LPG Eq. 3.4 discussed in **Chapter 3**, the RW should appear within the light source wavelengths between 400 to 1200 nm in this experiment.

7.2.2.2 Results and Discussion

The result of the high RI grating experiment is shown in Fig. 7.7 (a). Compared with the spectrum of the bare grating, a clear amplitude drop can be seen in the spectrum of the oil-clad grating. This distinct drop led to a clear change of shape in the spectrum as well. The amplitude of the first peak at 750 nm dropped from by approximately 80% relative to the second peak. Above 670 nm, the drop becomes smaller and finally ends around 1000 nm. This indicated that the light transmitted in the fibre had been successfully coupled via the grating and partially lost into the environment through cladding at the RWs. To show this change more clearly, the ratio of spectra (with and without index oil) at every wavelength were calculated and plotted in Fig. 7.7 (b). It can be seen clearly in the figure that the RWs were in the wavelength region of 500 to 670 nm.

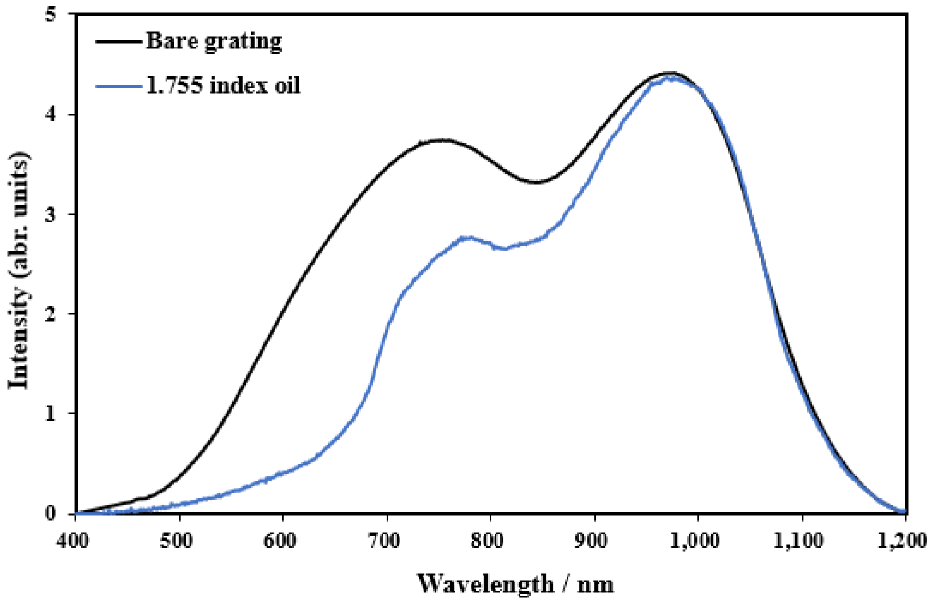

Figure 7.7. (a) spectra comparison before and after adding 1.755 index oil

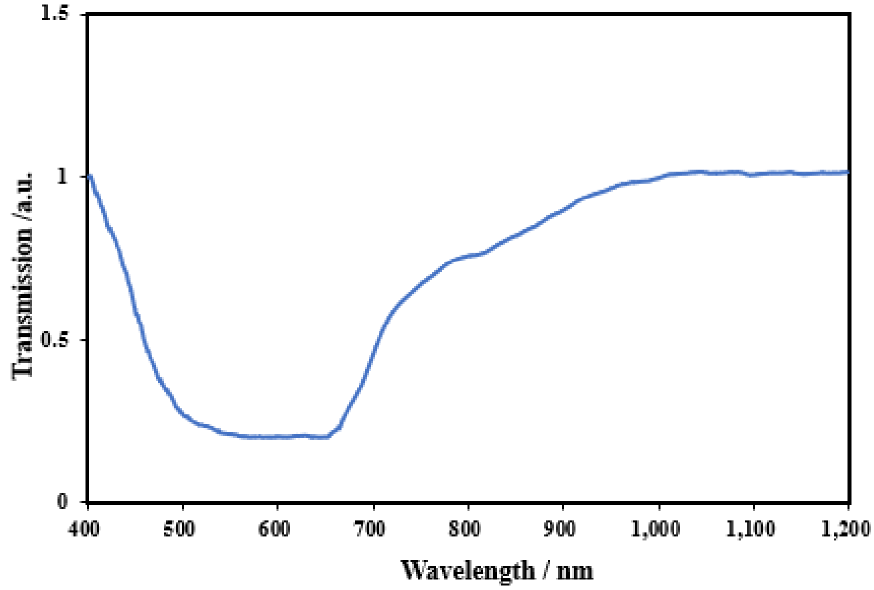

Figure 7.7. (b) ratio of spectra with and without index oil

Unlike conventional single-mode LPG in glass or plastic fibres [7.11, 7.12], which usually have the RW across a relatively narrow wavelength range, the appearance of the RW in LPSFG is in broader range, in this case, from about 500 to 670 nm. It is due to the large core diameter and multimode characteristics of the single-crystal sapphire fibres. This brings both advantages and disadvantages to the LPSFG sensor. The advantage is that since the loss at the resonant wavelength region (RWR) is large, it is very obvious and therefore easy to locate the RWR in the spectrum. The disadvantages also come from the appearance of the RWR. Firstly, unlike FBG sensors that usually exploit a narrowband reflective light at RW as the sensing indicator, the LPG sensors use the attenuated, transmitted light at the RW as the sensing indicator; plus, in this case, as an even larger portion of light is lost at the RWR of LPSFG, the strength of the transmitted light signal received by the photodetector can become quite small. If the signal received is too small, the resolution of the spectrum can be influenced, and thus the resolution of the sensor. Secondly, since the RW in a single-mode LPG is at a precisely defined wavelength, it is easy to locate the RW and track its wavelength shift during the sensing procedure; however, in LPSFG case, the RW is a broad region instead of a certain specific wavelength, thus, it is difficult to set and track precisely one characteristic wavelength, representing the average, for example, of the RWR. This can influence the accuracy of the sensor if the reference point is not set properly. Although there are few shortcomings of the LPSFG, this experiment had successfully shown that the resonant wavelength in spectrum of LPSFG for the first time, which illustrates the coupling has occurred between the core and the cladding mode of the LPSFG, and also proves the feasibility of the LPSFG.

7.2.3 LPSFG with cladding of varying refractive index

7.2.3.1 Experiments

The working principle of LPG sensors is to determine the change of measurands through the change the RW. Therefore, for an LPG to be a practical sensor, its RW should be sensitive to a change in the measurand. Based on this, an experiment using a range of liquids of varying RI was conducted, as illustrated in Fig. 7.8. To ensure the consistency, the same 90 μm fibre grating was used as the sensing grating; the experimental system was also the same as the previous setups and settings (LIA sensitivity of 3 mv and time constant of 1 s), and again, only change is the index liquid. In this experiment, 1.5 ml of 1.755 RI oil was first added into the grating chamber; then, after recording the spectrum, the following experiments can be divided into two steps. In the first step, 0.75 ml of 1.760 RI oil was added into the same chamber without removing the previous 1.755 RI liquid; after that, the spectrum was scanned continuously every 15 minutes to record any changes of RW until there were no further changes detected. In the second step, 0.75 ml of 1.765 RI oil was also added into the same chamber which had been previously filled with two volumes of 1.755 and 1.760 RI index liquids. Similarly, after adding the oil, the spectrum was scanned every 15 minutes to record any changes of RW until there were no further changes detected. Since there is no means to actively mix the RI oils in the chamber, mixing progressed via normal diffusive mixing. In this way, the RI of the mixed liquids in the chamber can be altered. The illustration of the experiment procedure is shown in Fig. 7.8. As the components comprising this series of index liquids are the same, the RI of the liquid mixture inside the chamber should have increased over time when the higher RI liquids were added. According to the basic principle of LPG, the RW should move to longer wavelengths. To verify this experimentally, the spectra at different stages of the experiment were plotted and compared at the end.

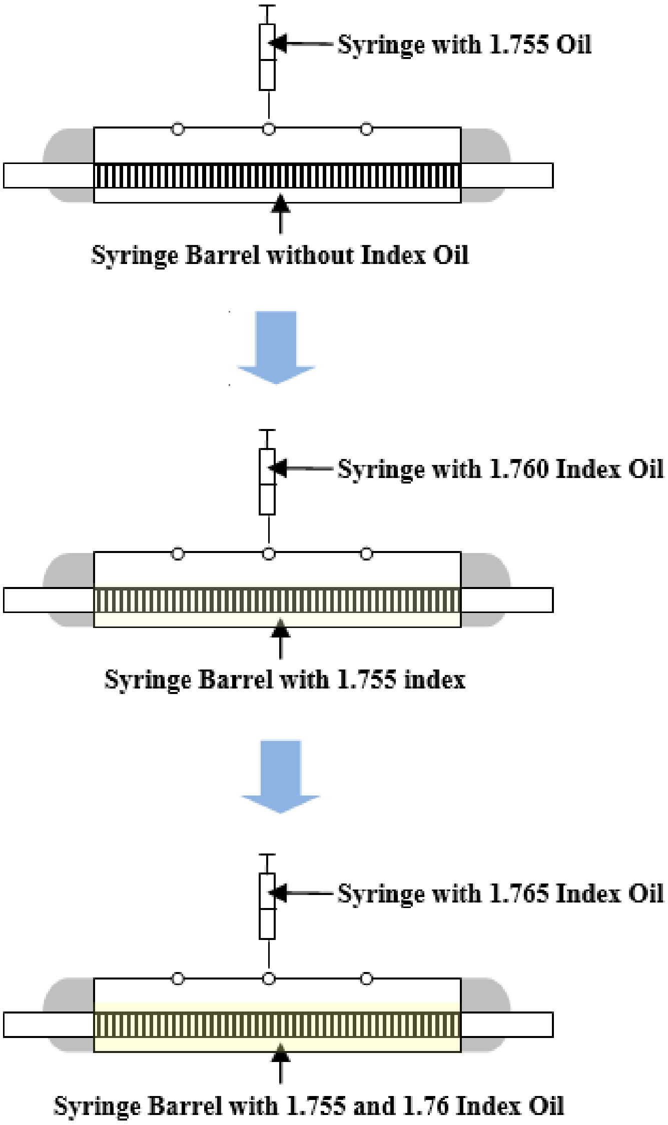

Figure 7.8. Illustration of variant refractive index experiment

7.2.3.2 Results and Discussion

The result of the experiment is shown in Fig. 7.9. In Fig. 7.9 (a), the spectra of the output light before and after adding the 1.755 RI oil is shown, which have similar amplitude and shape as with the previous result in Fig. 7.7 (a). Fig. 7.9 (b) shows spectra comparison before and after adding 1.760 and 1.765 index oil at different stages. As is shown, 15 minutes after adding 1.760 RI index oil, a drop appeared in the 650 nm to 850 nm waveband compared with the previous spectrum with 1.755 index oil, which can be seen from the green spectrum in Fig. 7.9 (b). No further change was seen after 15 minutes. Since the change in spectrum was confirmed to have stopped, the 1.765 RI oil was then added into the chamber to further increase the RI. This leads to the amplitude drop in the 750 nm to 850 nm waveband, causing distinct changes in shape of the spectra. The spectra at 15 minutes and 30 minutes after adding the 1.765 RI oil are presented with the brown (at 15min) and red (at 30 min) spectra in Fig. 7.9 (b), respectively. The scan was stopped as there is no further change detected after 30 minutes. Evidently, after adding the 1.760 and 1.765 RI oils, the 750 nm peak in the original spectrum had gradually diminished, illustrating the RWs had changed. Fig. 7.9 (c) also shows the ratio of spectra of the output light at different stages after adding the index liquids and spectrum of the bare grating. Same spectrum colours were used to indicate the corresponding spectrum in Fig. 7.9 (b). The RWRs of 1.755, 1.760 (15 mins), 1.765 (15 mins), 1.765 (30 mins) expanded from a shorter wavelength to longer wavelengths with the longest wavelengths of 670 nm, 740 nm, 780 nm, and 820 nm, respectively. As the expected, clear responses of RW to measurand changes had been seen, which further proves the sensing feasibility of the LPSFG.

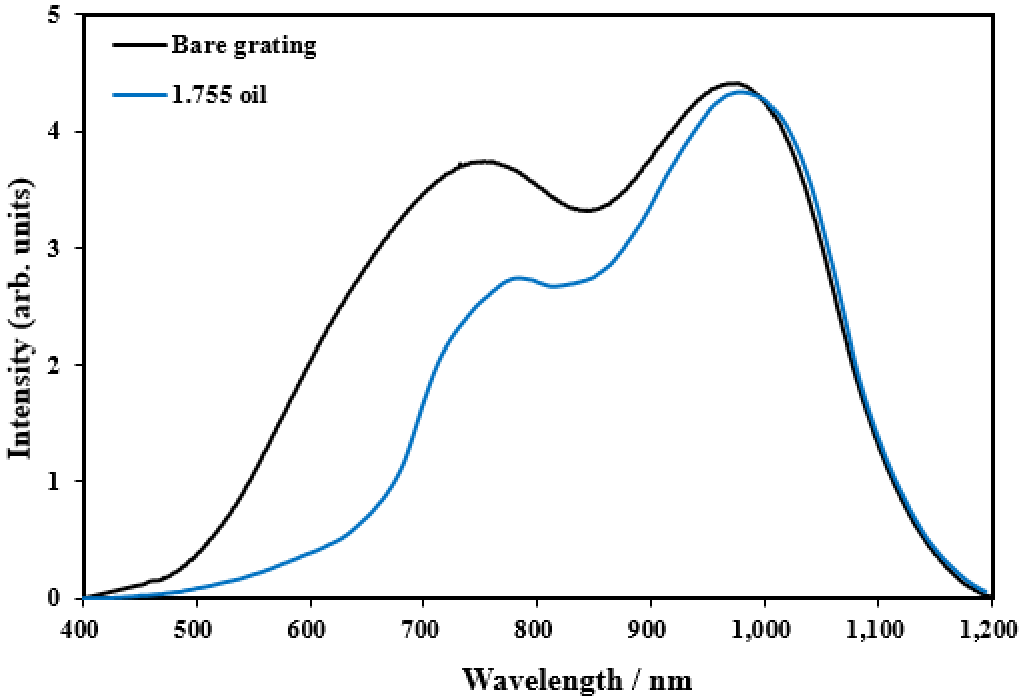

Figure 7.9. (a) spectra comparison before and after adding 1.755 index oil

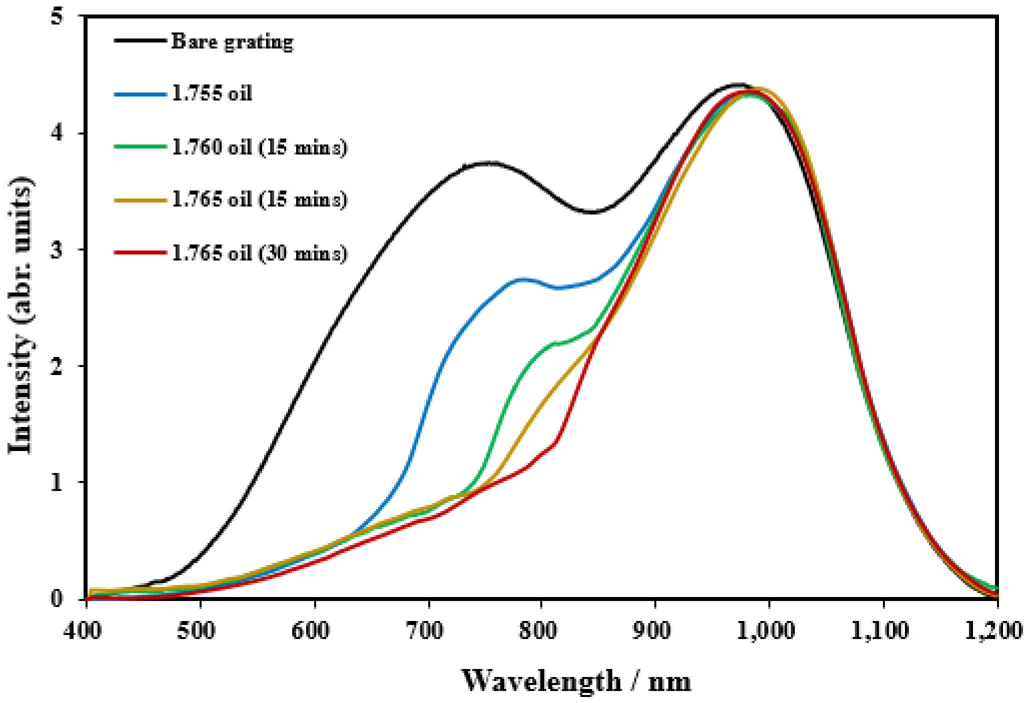

Figure 7.9. (b) spectra comparison before and after adding 1.760 and 1.765 index oil

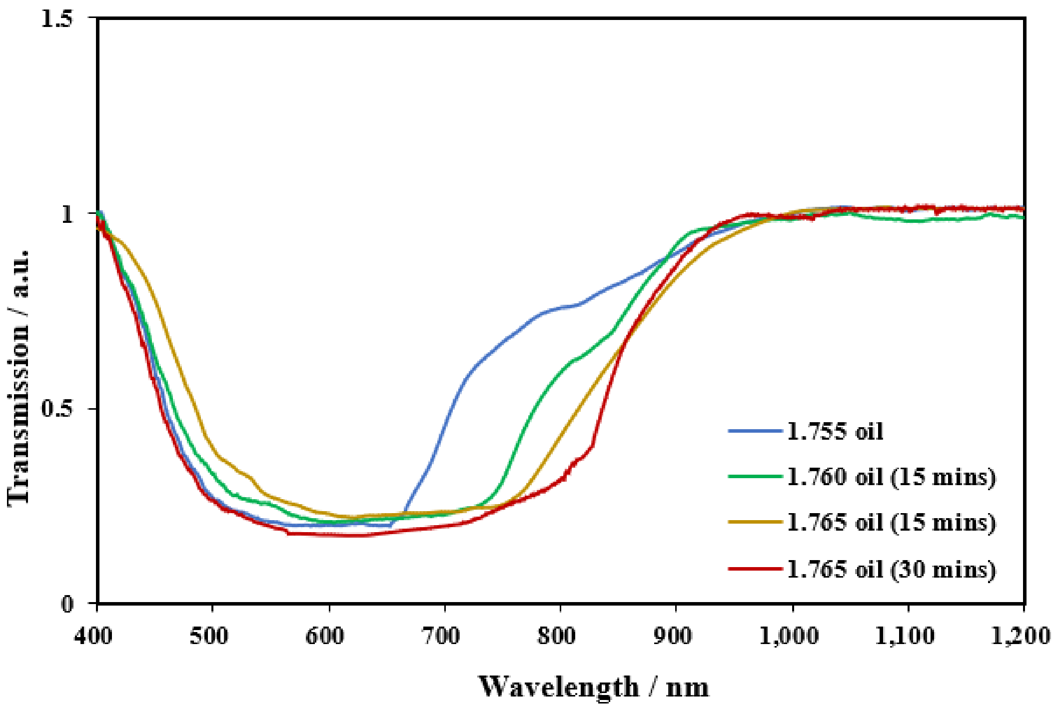

Figure 7.9. (c) spectra ratio before and after adding 1.760 and 1.765 index oil

7.3 Improvements and potential applications

In this experiment of LPSFG in high RI cladding, the grating effect was experimentally observed by the clear appearance of the RWR on the spectrum. Compared with the results of the change in the reflected specklegram pattern in the diced long-period grating experiment in [7.13], the results in this experiment indicated the appearance of RWs clearly and showed the loss at RWs in a more direct way, proving the grating effect of the LPSFG in a straightforward fashion. The success of the combination of the MSV technique and the LHPG technique has created an innovative LPSFG with many advantages over LPSFG produced by the dicing method, functionally and financially. In this experiment of LPSFG in variant RI cladding, the change of the RWR of LPSFGs was first observed and reported, which has also proved the sensing ability of LPSFG by showing its optical response to refractive index change in the material around the fibre grating. The appearance and shift of the RWR has also provided a new perspective to assess pros and cons of the LPSFG sensors, which may result in a new generation of sapphire fibre sensors.

7.4 References to Chapter 7

[7.1] P. Wang, H. Zhao and G. Brambilla, "Long period grating inscribed in multimode fibre interferometer and its application in refractive index sensing," in *24th International Conference on Optical Fibre Sensors*, 2015, vol. 9634, pp. 1-4. doi: 10.1117/12.2191126

[7.2] S. Lee, "Long period gratings in multimode optical fibers: application in chemical sensing," *Optics Communications*, vol. 224, pp. 237-241, 2003.

[7.3] H. C. Seat, "Growth and characterisation of single-crystal fibres for sensing applications," Doctoral dissertation, Dept. Mech. Eng., Gla. Uni., Glasgow, UK, 2001.

[7.4] M. Pulido and J. Alvarez, "Optical fiber torsion sensor with mechanically induced long period fibre gratings in rare-earth doped fibres," *Optics and Photonics Journal*, vol. 4, pp. 129-135, 2014.

[7.5] D. Grobnic and S. Mihailov, "Sapphire fibre bragg grating sensor made using femtosecond laser radiation for ultrahigh temperature applications," *Photonics Technology Letters*, vol. 16, pp. 2505-2507, 2004.

[7.6] S. James, S. Khaliq, and R. Tatam, "Enhanced sensitivity fibre optic period grating temperature sensor," in *15th Optical Fiber Sensors Conference*, 2002, doi: 10.1109/OFS.2002.1000521

[7.7] A. Kersey and M. Davis, "Fiber grating sensors," *Journal of Lightwave Technology*, vol. 15, pp. 1442-1463, 1997.

[7.8] P. Kumar, "Long-period grating in multimode fibre for ammonia gas detection," in *Asia-Pacific Optical and Wireless Communications*, 2003, vol. 5279, pp. 330-335, doi: 10.1117/12.520559.

[7.9] F. Zhou, Y. Liu, and S. Zhu. "Temperature sensitivity enhancement of the nano-film coated long-period fibre grating," *IEEE Sensors Journal*, vol. 16, pp. 2460-2464, 2016.

[7.10] L. Su and K. Chiang, "CO_2-Laser-induced long-period gratings in graded-index multimode fibre for sensor applications," IEEE Photonics Technology Letters, vol. 18, pp. 190-192, 2006.

[7.11] M. Nespereira, J. Coelho, M. Abreu, and J. Manuel, "Ultrashort long-period fibre grating sensors inscribed on a single mode fibre using CO_2 laser radiation," *Journal of Sensors*, vol. 2017, pp. 9, 2017.

[7.12] P. Xue, F. Yu, Y. Cao and J. Zheng, "Long period gratings imprinted on the commercial plastic optical fibers for refractive index sensing," in *Advanced Sensor Systems and Applications*, 2018, vol. 10821. doi: 10.1117/12.2500242

[7.13] S. Nam, C. Zhun, and S. Yin, "Recent advances on fabricating in-fiber gratings in single crystal sapphire fibre," in: *Conference on Photorefractive Fiber and Crystal Devices - Materials, Optical Properties and Applications*, Denver, 2004, pp 147-155. doi: 10.1117/12.558656

Chapter 8 – Sapphire Fibre LPG Back Coupling Sensors

Chapter 8 – Sapphire Fibre LPG Back Coupling Sensors

With the successful fabrication of LPSFG, gratings with different growth parameters have been grown and shown good consistency and repeatability in resonant wavelength experiments. In the process of growing and testing fibre gratings with different growth parameters, for the first time, a back coupling (BC) effect was found in LPSFGs; this could greatly improve the performance of LPSFG sensors. The unique optical properties of back coupling gratings (BCG) have also opened the door to the large potential of developing other optical sensing technologies, as well as future lasers. In this chapter, the generation of, experiments with, and potential applications of BCGs are reported.

8.1 Sapphire Fibre LPG Back Coupling

Usually, in LPFG sensors, light coupling occurs between core modes and the cladding modes, which results in the light loss at RWs in the transmission spectrum. However, when the length and strength of the LPFG exceeds a certain value, a portion of that light that is originally lost from the fibre core to the cladding can be coupled back into the core [8.1, 8.2, 8.3]: the so-called back coupling phenomena in LPG. As the generation of the BC effect requires an especially greater length ($\geq$ 4.5 cm) of fibre grating, there are limited studies of BC in conventional fibres. Moreover, there are no studies of BCGs in SCFs. Most studies of LPG have been based on using different techniques to fabricate or improve new LPGs in traditional commercial fibres. In the most recent study, the BC effect was investigated for developing biological applications [8.3]. In this paper [8.3], the LPG with BC effect was fabricated using a commercial plastic fibre by a point-by-point laser method. The back-coupling effect was shown at the RW with the amplitude of the light signal increasing. It was proposed that this effect could be used to couple a proportion of light into the fibre initially, transmit this into its cladding and then back couple into the core for further transmission up to a detector with little attenuation. With knowledge of the emission spectra of the target biological object, the period of LPG could be chosen, so as to selectively couple the corresponding emitted light from the target into the fibre core, realising biological sensing for the objective of interest.

In this project, the BC effect was first found in the optical experiments of LPSFGs fabricated by the MSV technique. The setup of the experimental system was the same as for the LPSFG system shown in Fig. 7.1 in **Chapter 6**, with only the grating features and corresponding index oil changed. In the experiment, the bare grating without index oil was first scanned to obtain the reference spectrum, then without disturbing any components or settings, the index oil was carefully added into the chamber using a syringe. Subsequently, the output signal was scanned again to get the response spectrum. The BC effect was found in three fibre gratings. These gratings have same grating length of 4.5 cm, same diameter of 350 μm, same FAM of 0.02 and different grating periods of 700 μm, 800 μm, and 900 μm, respectively. Compared with the grating with 3.5 cm length, 90 μm period and 0.01 FAM, these three gratings not only have longer length and periods but also possess more obvious grating structures with a perceptible diameter change; in other words, the difference between the largest diameter and smallest diameter of each single grating is larger. The longer length, period and larger FAM value of the grating form the basis of the generation of the LPG BC effect. In the experiment investigating these three gratings, the spectrum of each grating was scanned before and after adding the corresponding index oil, respectively. The results are shown in Fig. 8.1 to Fig. 8.3 below, both original scan spectra and ratio spectra are shown for each grating. It is worth to note that the system setup (Fig. 7.1) and setting (LIA sensitivity of 3 mv and time constant of 1s) are the same for each scan.

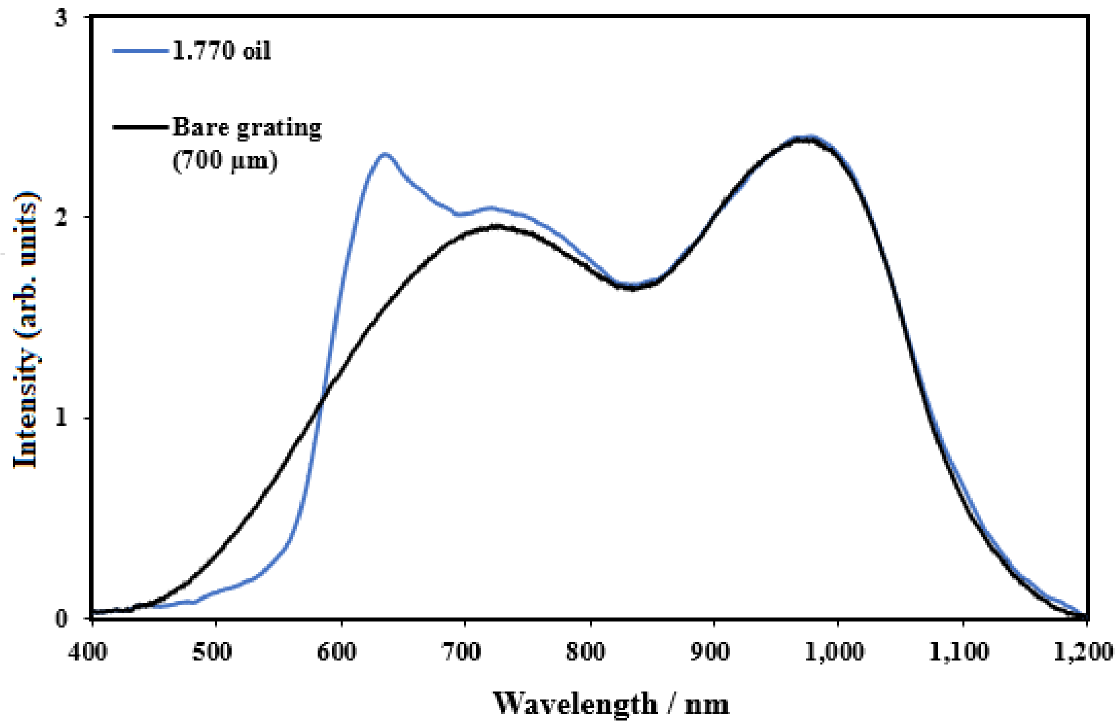

Figure 8.1. (a) BC spectrum of LPSFG with 700 μm period

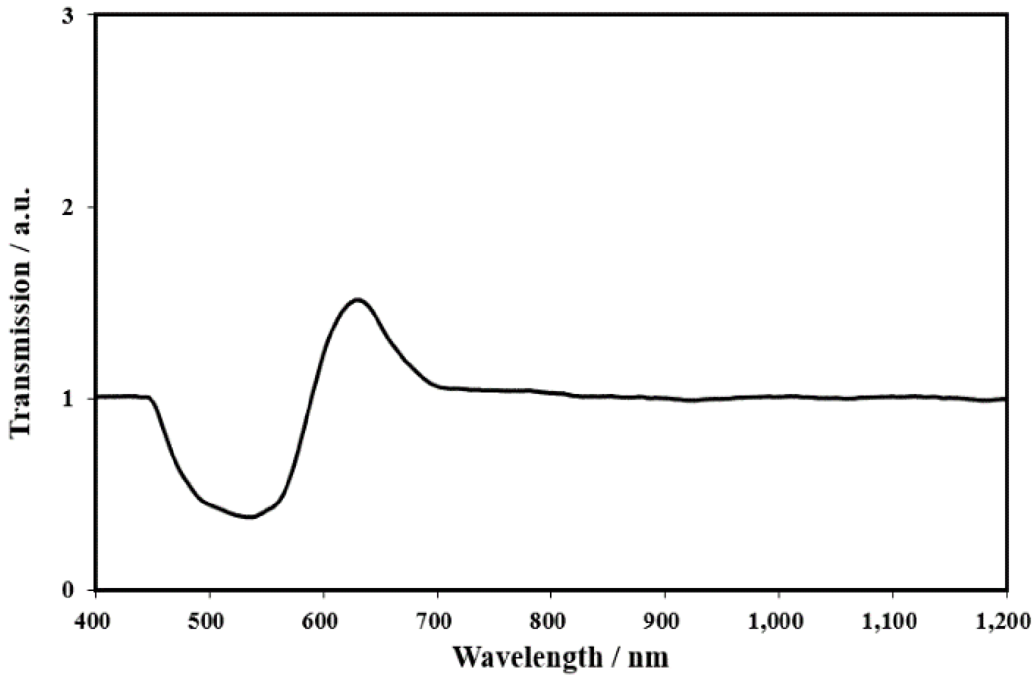

Fig. 8.1. (b) BC ratio spectrum of LPSFG with 700 µm period

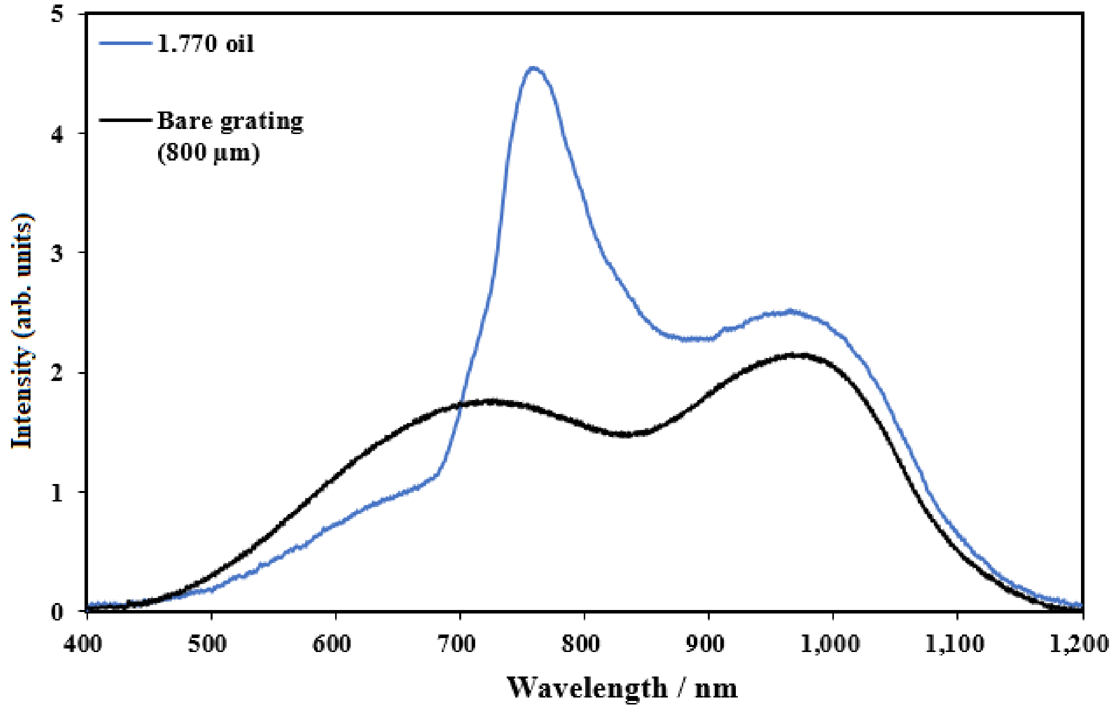

Figure 8.2. (a) BC spectrum of LPSFG with 800 µm period

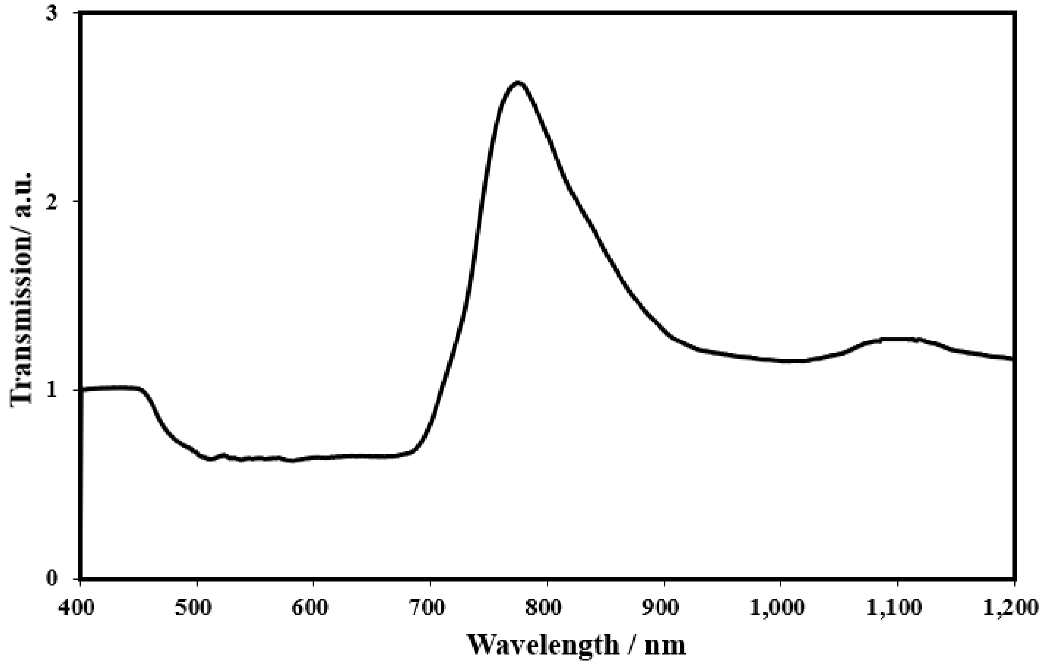

Fig. 8.2. (b) BC ratio spectrum of LPSFG with 800 µm period

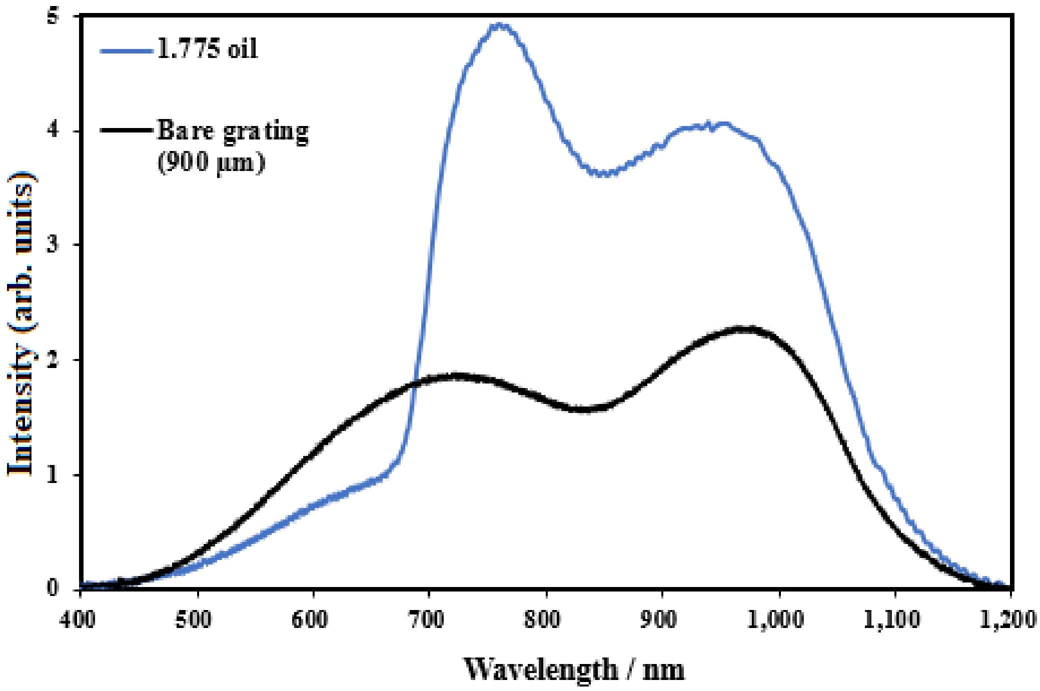

Figure 8.3 (a) BC effect of LPSFG with 900 µm period

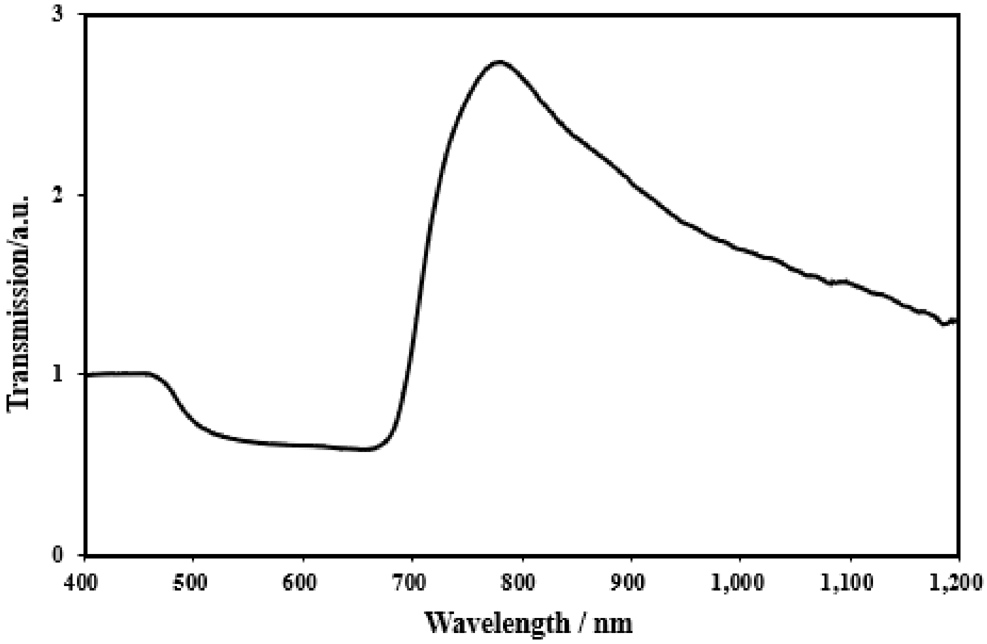

Fig. 8.3. (b) BC ratio spectrum of LPSFG with 900 μm period

From the BC spectra it can be seen that the spectrum of each bare grating has the same shape as the original light source. However, with the addition of the corresponding index liquids, the change of spectra is significant different from the previous LPSFG results in two main aspects. Firstly, instead of producing a large loss in RWR like normal LPSFG described in **Chapter 6**, the spectrum of the BCG has a typical rise in amplitude with a distinct peak at a wavelength in the RWR. The peaks in each spectrum can be directly distinguished in Fig. 8.1 (a), Fig. 8. 2 (a) and Fig. 8.3 (a), which are at 636 nm, 759 nm, and 762 nm, respectively in each figure. This peak at the RW or the "resonant peak (RP)" in the spectrum of the BCG was generated by the portion of the light that was originally lost at the RWs but coupled back into the fibre core from the cladding, causing the amplitude rise at RWs. Secondly, by comparing the three graphs, it can be seen that when the grating period increases, the signal amplitude at longer wavelengths (850 nm to 1150 nm in this case) also doubled with the original spectrum shape unchanged. Since the shape at the longer wavelengths remains the same, the RP can still be easily distinguished. These two unique features of BCGs can provide significant advantages for LPSFG sensors.

Unlike FBG sensors that use the enhanced reflective light at RWs as the indicator, the nature of conventional LPFG sensors is to use the attenuated transmission light at RWs as the indicator. Therefore, the output sensing signal is relatively lower for LPFG, particularly in the case of LPSFG, when the grating fibre has no cladding. The large core, lack of cladding, and highly multimode characteristics cause the LPSFG to lose a larger portion of light at RWR than LPFG in normal fibres, as shown in the results in **Chapter 7**. If the amount of the lost light is large, the output light received by the photodetector can become very small, with implications for the resolution and accuracy of the sensor. Also, the RW of LPSFG is a broad range of wavelengths rather than a particular wavelength that has a clear, precise signature in the spectrum. This could potentially introduce uncertainty when the basic shape of the RWR changes. These two obvious drawbacks would make LPSFG less competitive in the optical sensing field. However, with BC effect, transmission signal can be strengthened, and a clear RP can be exploited as a sensing indicator. In this way, the drawbacks of LPSFG can be solved by the combination of LPSFGs and the BC effect. Therefore, in the following sections, the sensing abilities of BCGs are tested in terms of refractive index and temperature.

8.2 BCG Sensing Experiments

8.2.1 Refractive index sensing experiment

8.2.1.1 Experiments

The experimental arrangement for refractive index sensing using BCGs is same as that used for LPSFG. The main objective is to change the RI value of the cladding by adding small amounts of higher RI oil to see if there is any change of the RW. By means of adding index liquids of different RI value, the RI value of the liquid in the chamber of the sensing element can be manipulated, and so should the RW. The 700 μm period grating is used in this experiment. Initially, the 700 μm grating was placed in the chamber without the addition of any index liquid. After obtaining the spectrum of the bare grating as the reference spectrum, 1.5 ml of index oil with 1.770 RI was added into the chamber to generate its BC spectrum. Once the spectrum with the corresponding RP was obtained, 0.75 ml of index oil with 1.775 RI was added into the chamber; after adding the oil, the spectrum was scanned every 10 mins to record any changes in the RP until the spectrum became stable. The reason that the short time period (10 mins) between each scan was used here is that unlike the RWR which changes slowly as an entire waveband, the RP can be located at one particular wavelength in RWR and it can exhibit a larger and more noticeable change than the whole RWR, when the ambient RI changes. Once the spectrum had stabilised, 0.75 ml of index oil with 1.780 RI was added into the same chamber; similarly, the spectrum was scanned every 10 min until the change of spectrum stopped. The illustration of the whole experimental procedure was the same as in Fig. 7.8 with only the grating and index oil changed. Intuitively, with higher index liquids added into the chamber, the RI of the cladding increased with time; therefore, the RP, should move to longer wavelengths with time. To test this theory, the spectra at different stages of the entire experiment were scanned in the same system with same settings (LIA sensitivity of 3 mv and time constant of 1s) and plotted in the same graph for comparison at the end.

8.2.1.2. Results and discussion

The result discussion of the BCG RI sensing experiment can be divided into three parts. The first part is the comparison between the spectra of the 700 µm bare grating and after it was added by the 1.770 RI oil, which is shown in Fig. 8.4 (a). The result spectrum is same as the spectrum in Fig. 8.1 (a): the spectrum shape of the bare grating is the same as the original light source, and after adding the index oil, the BC effect occurred at around 636 nm with an evident peak in the spectrum.

The second part is the result of adding the first higher RI index oil (1.775), as shown in Fig. 8.4 (b). In the figure, it can be seen that the RP has moved to longer wavelengths as expected, with steps at wavelengths 660 nm, 671 nm, and 676 nm, at 10 mins, 20 mins, and 30 mins respectively, after adding the index oil. After 35 minutes, no further change was observed.

The third part is the result of adding the second, higher RI oil (1.780), as shown in Fig. 8.4 (c) with the result of the second part can still be observed in the same spectrum. Clearly, after adding 1.780 RI oil, the RP continued shifting to longer wavelengths in the next 30 mins, with steps at wavelengths of 704 nm, 723 nm, and 730 nm, at 10 mins, 20 mins, and 30 mins, respectively. After 35 minutes, no further change was observed.

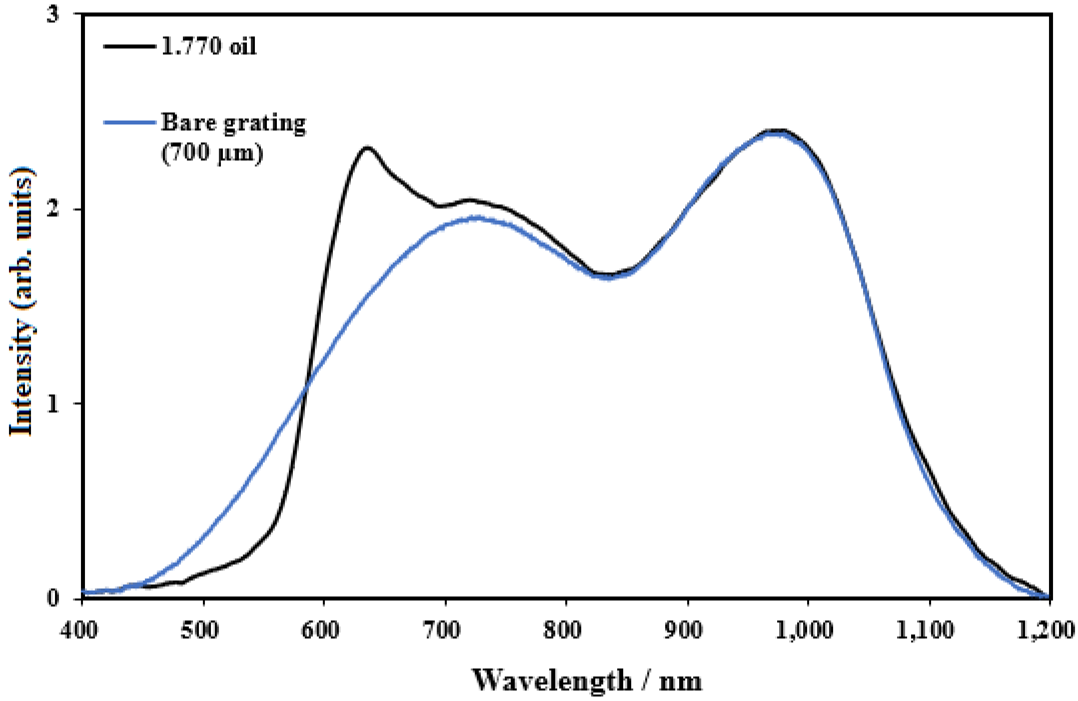

Figure 8.4. (a) 700 µm BCG after adding 1.770 oil

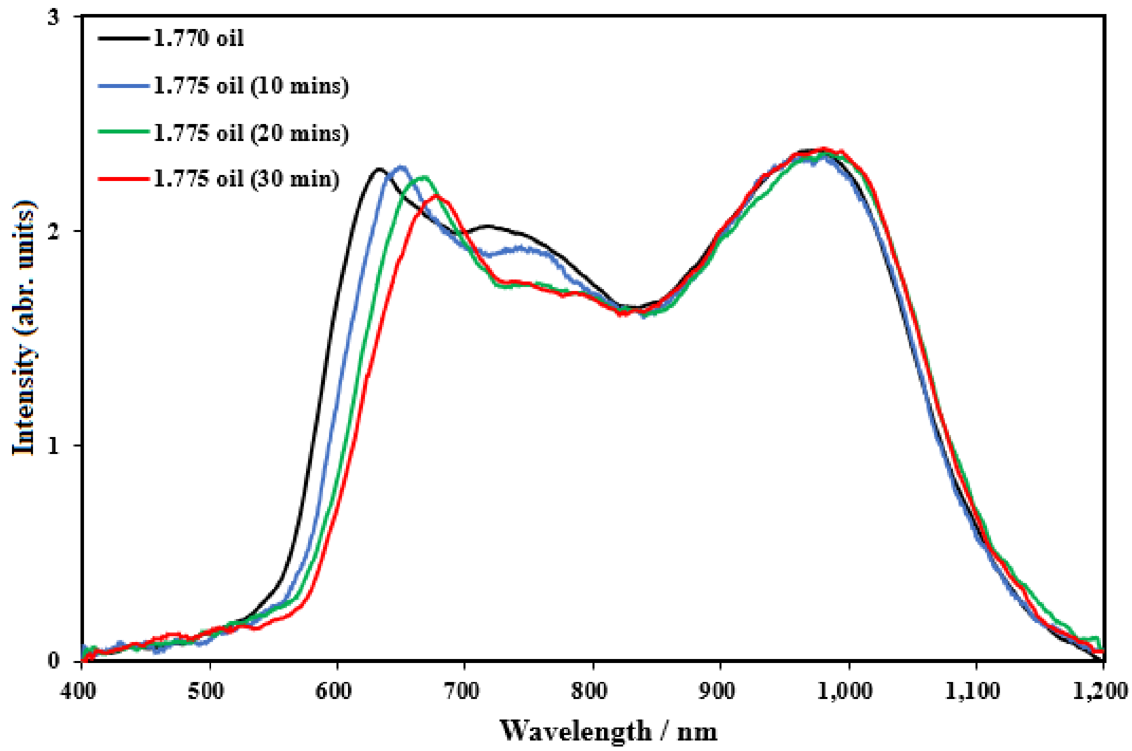

Figure 8.4. (b) spectrum change after adding 1.775 oil

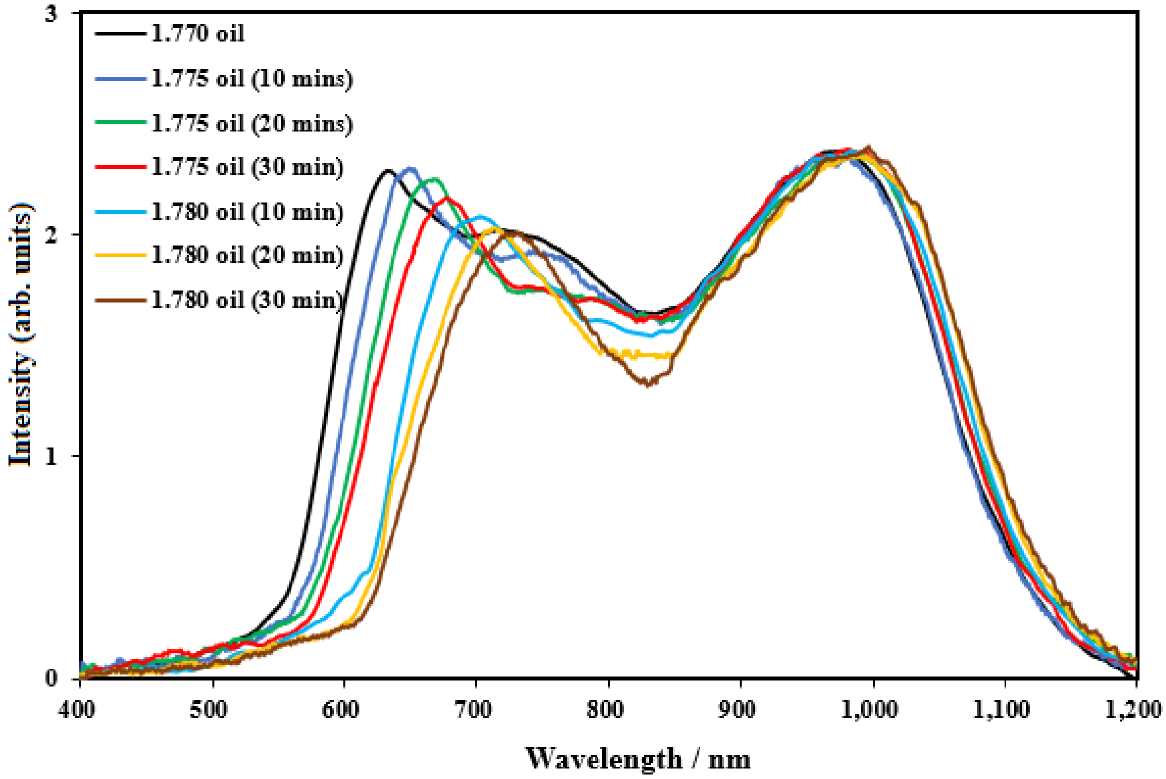

Figure 8.4. (c) spectrum change after adding 1.780 oil

The above results show that when the external RI changes, the wavelength of the RP of the BCG measurably changes. This proves the feasibility of using the RP generated by the BC effect for LPSFG sensors. Therefore, the original LPSFG fabricated by the MSV technique can be developed by utilising the BC effect. Thanks to BC effect, the drawbacks of LPSFG can be compensated. On the one hand, instead of losing light signal, the BC effect raises the relative total strength of the output signal with respect to that of the bare fibres, which not only increases the transmission efficiency, but also provides a strong and clean output signal for detection, increasing the sensing resolution at the same time. Additionally, rather than generating an RWR, the evident and relatively sharp appearance of the RP generated by BCGs greatly helps users to locate the RW and set a reference point for sensing applications, which could improve the accuracy when tracking the change of the reference point, and thus improve the accuracy of the sensor system.

8.2.2 Temperature sensing experiment

8.2.2.1 Experiment

As the RI sensing experiment was successful, to further examine the sensing ability of BCGs, a temperature sensing experiment was conducted and will be discussed in this section. Compared with the previous system, the only change in the temperature sensing system is to the structure of the sensing element. The specially designed structure of the sensing element allows the test of the response of the RP of BCGs to temperature. Fig. 8.5 shows the schematic and a photograph of the sensing element.

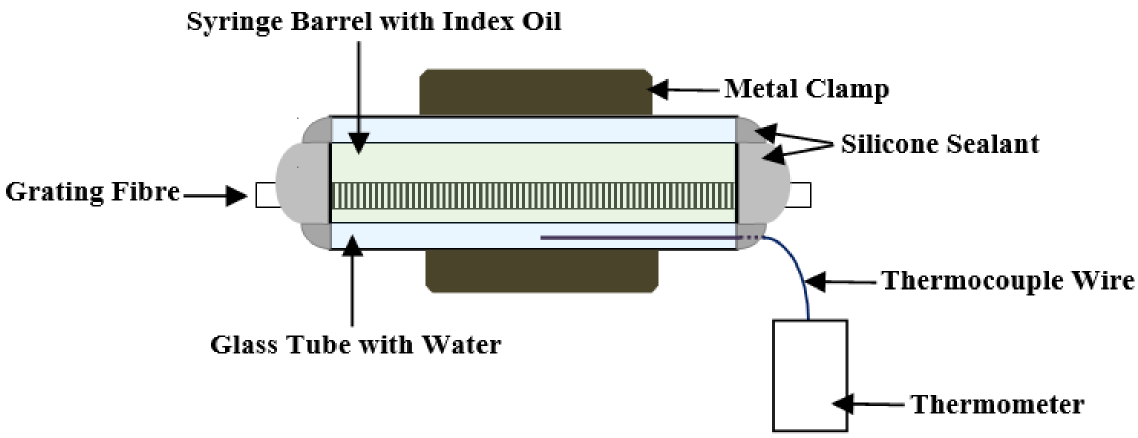

(a)

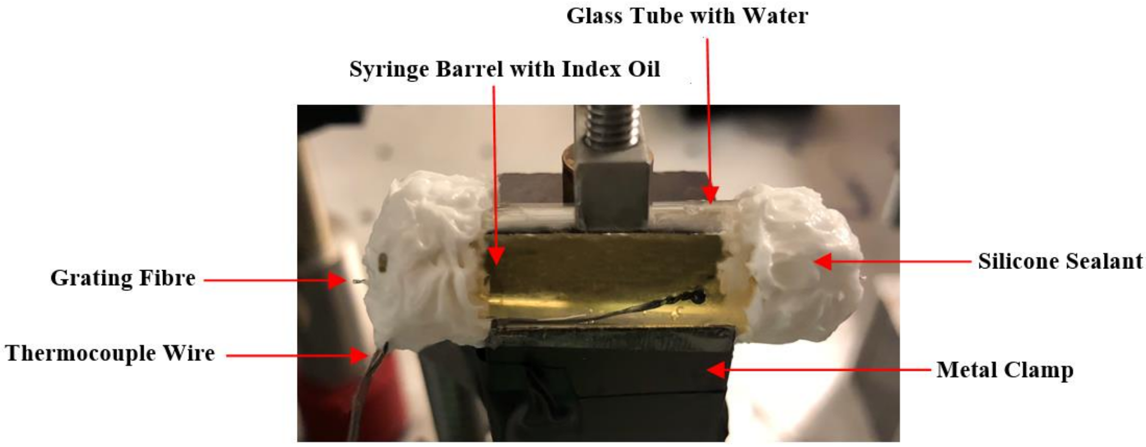

(b)

Figure 8.5. Structure of the sensing element for the temperature sensing experiment: (a) schematic diagram; (b) photograph of setup.

The structure of this sensing element comprised of two principle components: internal and external. The internal component has the same structure as the sensing element for the previous, RI experiment, which consists of a length of syringe barrel, a grating fibre, a volume of index oil, and silicon sealant. Like the previous sensing element, the index oil, which acted as the cladding of the fibre, was injected into the syringe barrel, which held a fibre grating in the centre. Both ends of the syringe barrel, as well as the lateral injection holes, were then sealed by silicone sealant to prevent any leaking.

The external component consists of a length of glass test tube, a thermocouple wire, silicone sealant, and water. The glass tube was diced from a standard chemical test tube, and the two ends of the diced tube had been polished by polishing machine to get rid of jagged edges before the fabrication of the sensor. Since the diameter of the glass tube (1.5 cm) is larger than that of syringe barrel (8 mm), the internal component can be contained wholly within the glass tube. One end of the glass tube was sealed together with one end of the completed internal component (the syringe barrel) using silicone sealant, leaving the end of grating fibre protruding outside of the structure. The glass tube was then filled with water from the other, open end, along with a thermocouple wire to record the water temperature. After that, the open end of the glass tube was sealed together with the other end of the syringe, using the silicone sealant, holding it in place, leaving the fibre end protruding, along with the thermocouple wire.

As the two ends of the fibre both remained outside of the glass tube and sealant, light could still be easily coupled into the grating and transmitted to the analysis system. The entire structure of the sensing element was fixed in place and held with a metal clamp. By heating the metal clamp underneath, the assembly heating temperature can be set. Insulated by the metal and glass of the surrounding structure, the rate of heat transfer to the grating can be rather slow; and the water inside of the glass tube helps to distribute the heat uniformly, as well as limit the temperature to a maximum of 100 °C. The outer structure can effectively protect the syringe barrel and index oil from direct rapid heating, and also sufficiently prolongs the heating time to easily obtain the spectrum at different temperature ranges. The thermocouple wire set in the water was linked to a multi-function infrared thermometer for direct temperature measurement as a reference.

In this experiment, the 900 µm period BCG fibre and the corresponding index oil with 1.775 RI were used for temperature sensing. With the same experimental system setup and a new sensing element, the spectrum of the sensing element was scanned first at room temperature (20 °C) to ensure the grating fibre exhibited a BC response. Then the temperature was raised with a step of 10 °C until reaching close to 100 °C by controlling the heat source. The corresponding spectra were scanned with the same settings (LIA sensitivity of 3 mv and time constant of 1s) and recorded at each temperature range for further analysis.

8.2.2.2 Results and discussion

The result of this experiment is shown in Fig. 8.6. The BC spectrum of the grating at room temperature is shown in Fig. 8.6 (a), which is the same as shown in Fig. 8.3 (a). The distinct grating effect was apparent in the spectrum with a clear RP at 768 nm. When heat was applied, and the temperature of the sensing element raised, the spectra recorded at each temperature are presented in Fig. 8.6 (b). From the figure, it can be seen that the RP of each spectrum moved to shorter wavelengths with the increase of temperature. The wavelengths of the RP at different temperatures were recorded and plotted in Fig. 8.6 (c). It can be seen that the wavelength of RP approximately follows a linear relationship with temperature change at different stages, especially in the temperature range between 30 °C to 80 °C. At the same time, the amplitude of each spectrum decreased as temperature increased as well, especially between 80 °C and 90 °C: the amplitude in this range suddenly plummeted, leading to an obvious change in the spectrum shape. This spectrum is also shown separately in Fig. 8.6 (d), where all the signal at longer wavelengths (700 nm to 1200 nm) attenuated to near zero, leaving only a sharp peak at 561 nm. This is likely due to a substantial change in chemical and physical properties of the index oil occurring at this temperature. It is worth noting that at the temperature below 80 °C, it was possible for the spectrum to revert back to its previous state if the temperature is lowered. However, once the temperature exceeds 80 °C, the change on the spectrum as Fig. 8.6 (d) is permanent and the oil breaks down; even when the temperature is lowered, the spectrum remains unchanged. As the index oil was not specially made for temperature experiments, this phenomenon is likely to be caused by irreversible chemical reactions which cause thermal decomposition of the oil, these occur rapidly only at higher temperatures when the activation energy of these reactions has been reached, leading to the permanent change of physical properties. When the temperature exceeded 90 °C, the silicone sealant became soft, which lead to some water leaking from the glass tube and the position of the grating fibre changing very slightly. This caused the alignment change, and the amplitude of the spectrum at all wavelengths dropped to near zero; the spectrum being almost entirely attenuated.

Due to these fundamental changes in the structure of the sensing element, it was concluded that the results beyond 90 °C were not reliable for analysis. Although there were some upper limitations in this experiment such as the chemical reaction of the particular index oil and the softening point of the silicone, the experiment was considered successful as RPs at each RW have shown a good linearity to temperature change, achieving a temperature sensitivity of 2.5 nm/ °C in the range of 20 °C to 100 °C. As the first temperature sensing experiment of LPSFG sensor in the field, it not only proved the temperature sensing ability of LPSFG, but also became the first critical step in developing LPSFG back coupling temperature sensors for harsh environments.

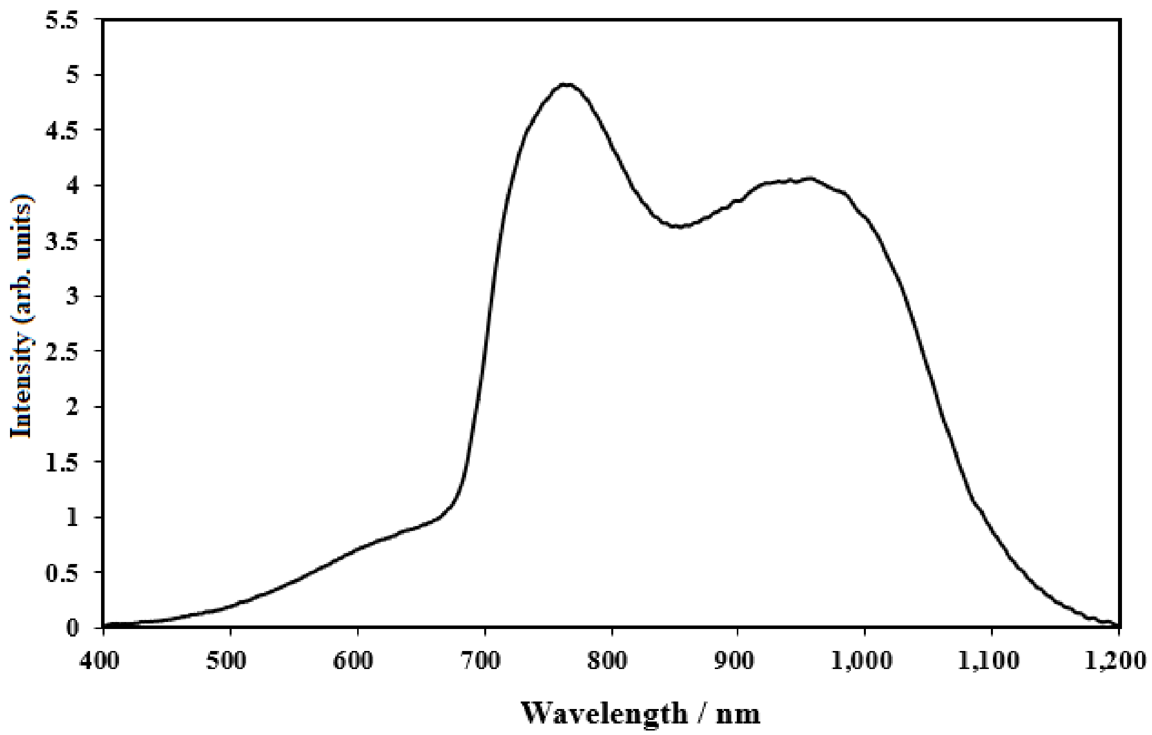

Figure 8.6. (a) BC effect of LPSFG with 900 µm period at room temperature

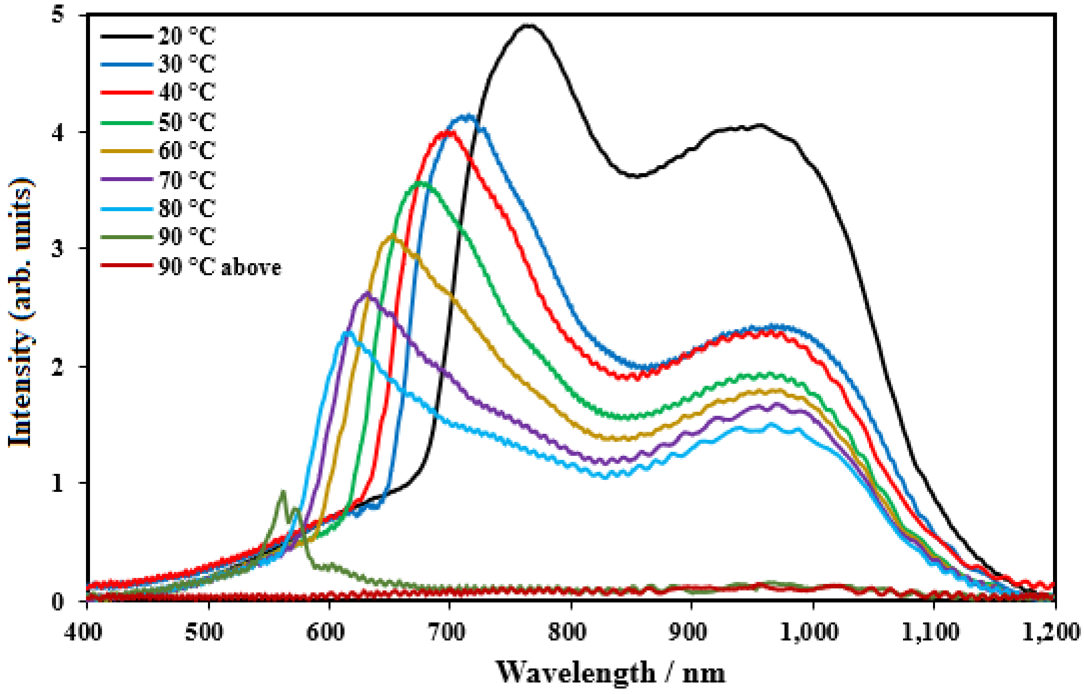

Figure 8.6. (b) BC spectra response to temperature

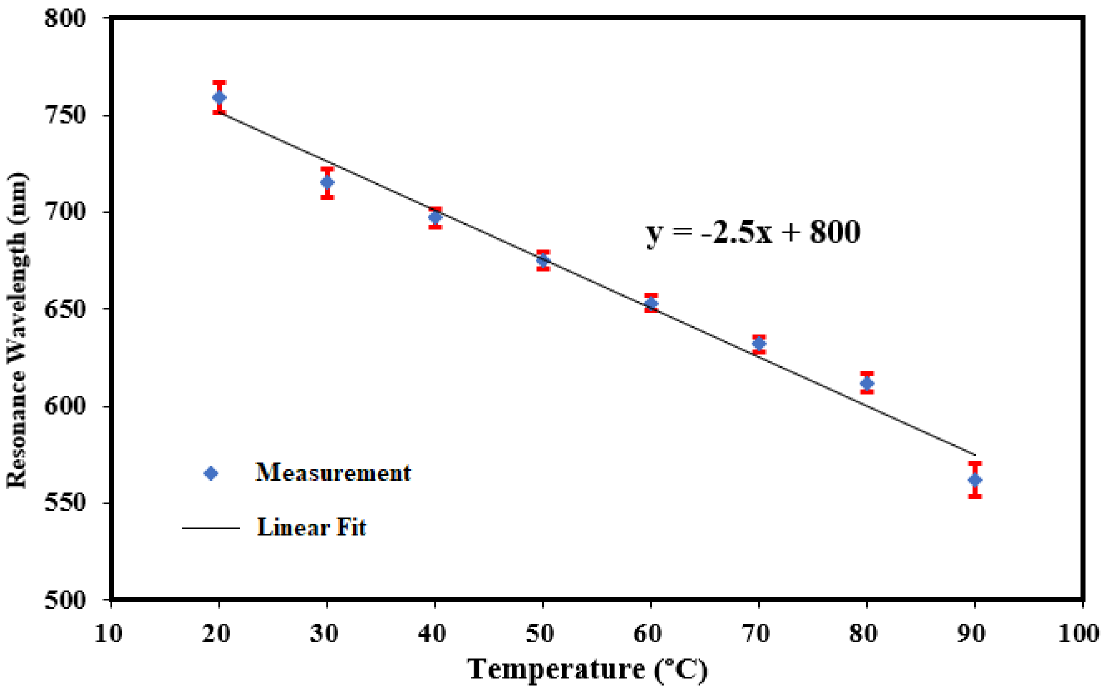

Figure 8.6. (c) RP shift with respect to temperature change

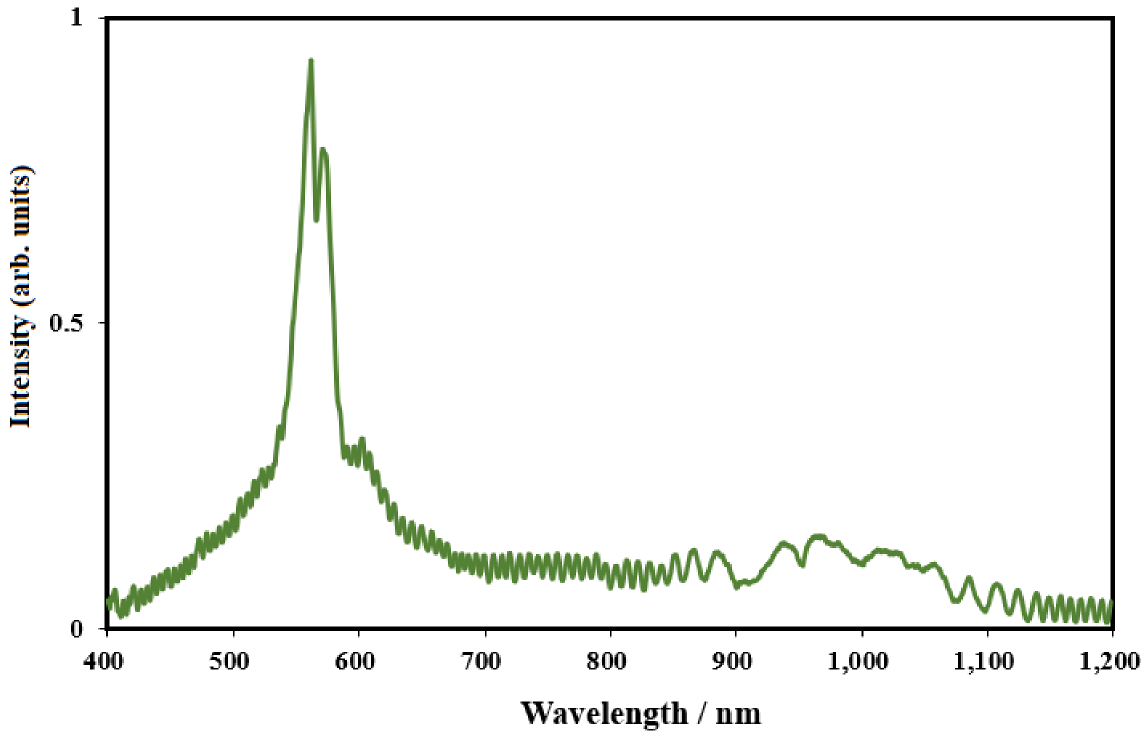

Figure 8.6. (d) BC spectrum at 80 °C

8.3 LPG Back Coupling Beam

In addition to the difference in sensing features of BC LPSFGs compared to standard LPSFGs, another special feature of the bare BCGs is the unique quality of the output light beam. Ordinary white light sources are divergent and incoherent, emitting light across a broad range of wavelength and, randomly, in all directions. Thus, the light originating from a single point, in this case output at end of a sapphire fibre, is divergent. Therefore, to transmit and collect this type of light, it is necessary to use short focal length lenses between different components, such as the light source and the fibre, and the fibre and the detector.

Unlike the ordinary light sources, the output light from the BCG fibres both with and without the index cladding exhibits some unique optical features. Instead of strongly diverging, the output light from BCG fibres is a highly collimated and concentrated light beam. Compared with the normal diffuse output light from ordinary sapphire fibres or sapphire fibre gratings without the BC effect, this particular concentrated light beam is collimated with much stronger luminance. The light beam is inherently focused to a sharp point and can be transmitted or directed without obvious attenuation for some distance. To investigate the features of the BC beam practically, preliminary tests were conducted as detailed below.

The test was designed to compare the output of bare BCG fibres and bare normal grating fibres (without BC effect) in terms of the intensity and spatial distribution of the output spot. The setup of the measuring system is schematically shown in Fig. 8.7 below. The light from the broadband light source was coupled into one end of the grating fibre through a × 20 MO; a stray light blocker, a piece of 1 mm thick black paper was set around the fibre to stop a small amount of scattered light from the MO; at the other end of the grating fibre, a *Fotec*. FM300 optic power meter was placed on a 3-axis aligner and used to receive the output light from the fibre; the aligner was installed on a positioning slideway to control the distance between the fibre end and power meter. To avoid disturbance from any other light source, the tests were conducted in a dark environment; also, to get enough light from the grating fibre for adequate detection, the outside connector of the power meter was removed with its optical sensor exposed. The 3-axis aligner was used to align the centre of the optical sensor to the fibre end during the experiment. In the test, the normal 90 µm period fibre grating without BC effect was used to compare with the 800 µm period BC grating fibre. To compare optical properties of the output signals over distance, the output power at the fibre tip was set to the same at the beginning of each test. The power meter was set at the same fixed position relative to the fibre tip, leaving 1 mm of distance between the centre of the power meter sensor and the fibre tip; after that, by controlling amount of light coupled to the MO, the output power at the fibre tip was set to the same value for each grating fibre at the beginning of their tests. In the test, the power meter was slowly moved away from the fibre tip on the slideway until the point where its power drops to 0 dB. The distance that power meter travelled, and the area illuminated by the output light from fibre tip: the "light spot", at this point were recorded and used for comparison.

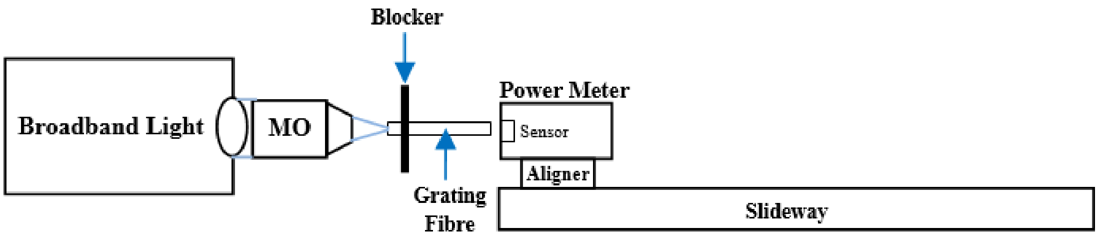

Figure 8.7. Schematic of BCG testing system

At the starting point, where the distance between the fibre tip and sensor centre was 1 mm, the output power at the fibre tip was set as 16 dB for both of samples. In the test of the normal grating, at the 13 cm point, the output power dropped to 0 dB. However, for the BCG, the power only dropped to 7.1 dB at 13 cm. An illustration of the light spots produced for both gratings at 13 cm is shown in Fig. 8.8 (a), where D_{BG} and D_{NG} indicate the diameter of the light spot of the back-coupling grating and normal grating, respectively. At 13 cm, the spot diameter of the BCG is only ~ 3.6 mm while that of the basic grating has already expanded to ~110 mm. Photographs of the two light spots at 13 cm, produced on a white background, were taken at the same position, as shown in Fig. 8.8 (b) and Fig. 8.8 (c). At distance of 25 cm, the output power of the BCG finally dropped to 0 dB while that of the normal grating was measured for -10.6 dB. In terms of the output spot, the diameter of the spot of the BCG has increased to 3.9 mm at 25 cm where the light spot of the normal grating had already become indistinguishable.

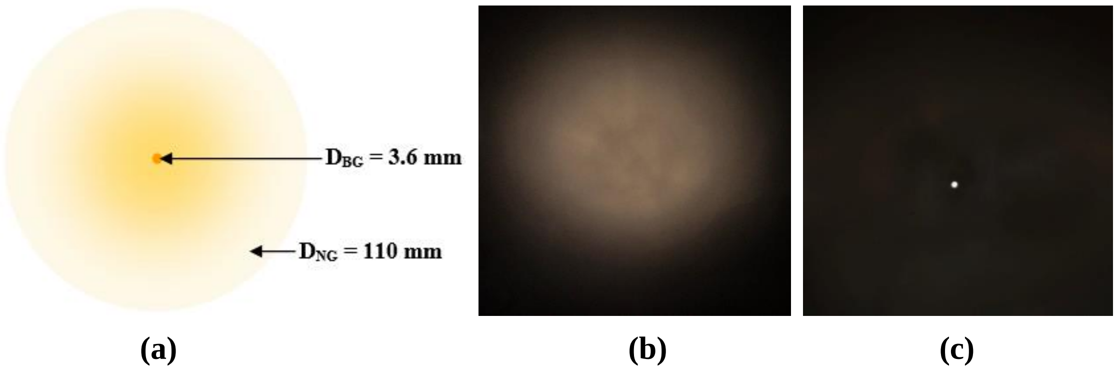

Figure 8.8. Illustration of light spots of two gratings at 13 cm: (a) schematic of two light spots; (b) photograph of the light spot of the normal grating; (c) photograph of the light spot of the BC grating.

To further study the BC beam properties, a *Gentec beamage* 3.0 beam profiling camera was used to compare the output light of the BC grating and the normal grating without BC effect. The same measuring system and procedure in Fig. 8.7 was used with a change of the power meter for a beam profiling camera. To measure the variation trend of the beam spots, the beam profiling camera was moved away from fibre tip and scanned the beam every 0.5 cm until the size of beam spots becomes larger than the maximum beam diameter camera can measure (30 mm). After doing measurements for both BC grating and normal grating, a straight sapphire fibre with same length and diameter but without grating was measured by the same system for comparison.

The result of output light beams of three fibres is potted in the Fig. 8.9 showing the beam diameter versus distance between the camera and the fibre tip. From the scatter diagram it can be seen that the straight fibre has almost the same result as the normal grating fibre; the beam diameter of both the straight fibre and normal grating fibre expands dramatically, approaching 29.4 mm at 4 cm distance, almost reaching the maximum beam diameter that the camera can measure (30 mm). After 4 cm the beam diameter of the straight fibre and normal grating exceeded 30 mm. By contrast, the diameter of the BC beam increased slowly, only reaching 0.92 mm at 4 cm. Based on the linear fitted lines, the divergence angles of each fibre were estimated. The normal grating and the straight fibre have a divergence angle of 80°, which is over 13 times larger than that of the BC grating (6°). Comparison between the output light of normal grating and BC grating at 4 cm in the 2D and 3D transmission graphs is also shown in Fig. 8.10 and Fig. 8.11, respectively. As it can be seen from the result of preliminary tests above, under identical conditions, the output beam of the BC coupling grating is much more collimated and concentrated than that of the straight fibre and normal grating fibre, and the fibre with BCG is able to deliver more signal for further distance with less attenuation (~0.65 dB/cm) than the other two fibres (~1.23 dB/cm).

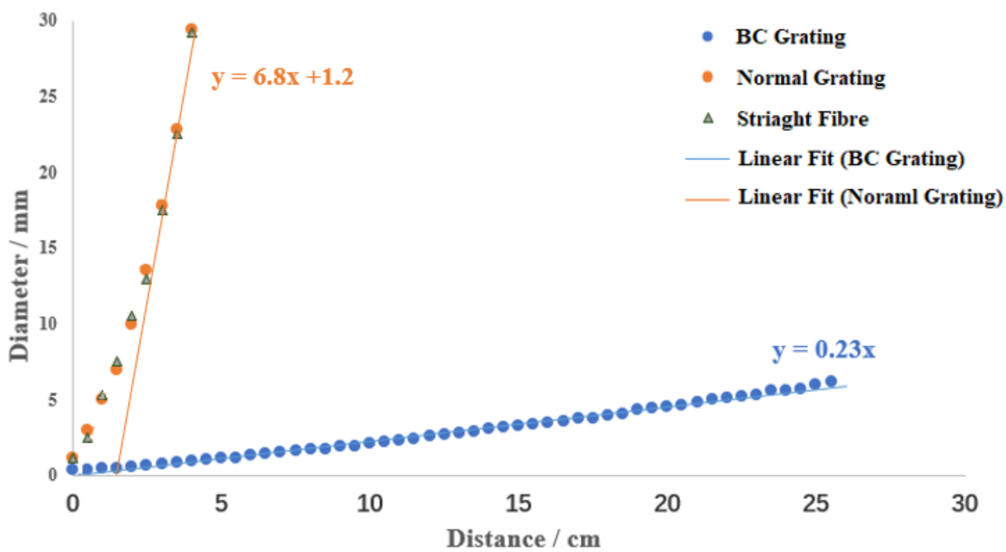

Figure 8.9. Beam measurement of two gratings using beam profiling camera

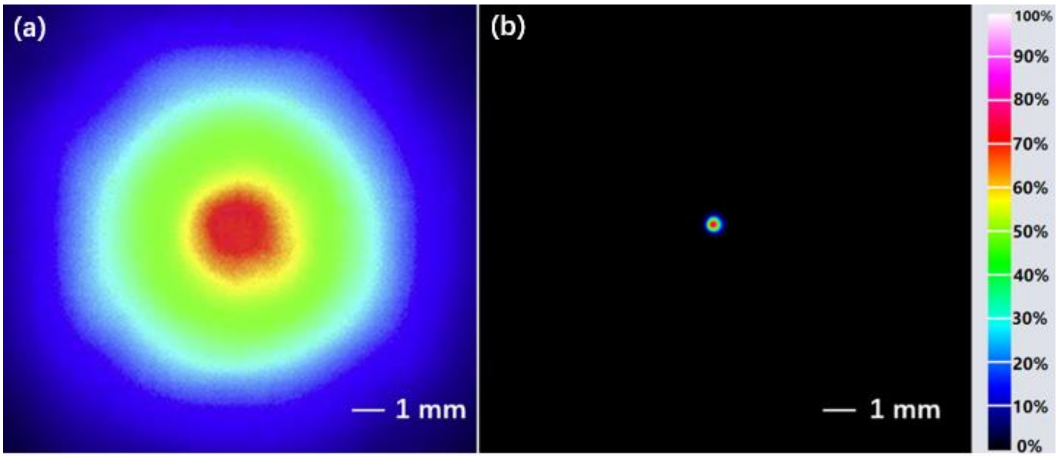

Figure 8.10. 2D transmission graphs of (a) normal grating beam and (b) BC grating beam at 4 cm

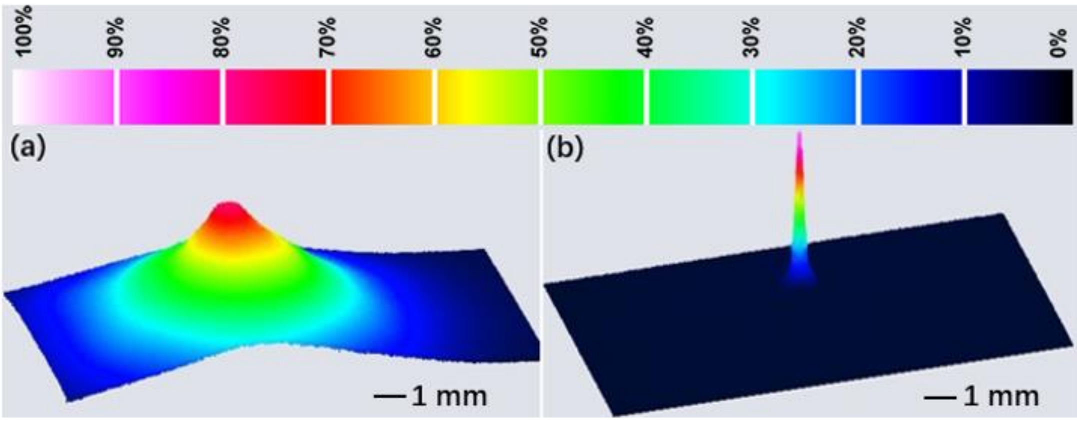

Figure 8.11. 3D transmission graphs of (a) normal grating beam and (b) BC grating beam at 4 cm

8.4 Improvement and potential applications

In this chapter, the BC effect was demonstrated in LPSFG for the first time. Instead of a loss of signal at the RWR, as seen in LPSFGs in **Chapter 7**, BCG can generate an evident RP with a clear peak in the output spectrum. This feature can compensate for the inherent shortcomings of LPSFG which results from a larger core diameter and a very high number of core modes than is usually seen in conventional multimode fibres. This significantly improves the practicality of the LPSFG sensor. The feasibility of the BCG sensor has been proven through the index oil experiment that directly showed the response of the RP of the BCG to the changing RI of surrounding material directly. The result shows the sensing ability of BCG as expected, becoming the basic template for the further development of the sensors such as the BC biological sensor discussed in [8.3]. The oil-clad temperature sensing experiment further demonstrated the sensing ability of the BCG sensors to ambient temperature change. This is significant, especially for LPSFG sensors since the greatest advantage of sapphire fibre is its excellent properties and stability in high-temperature environments.

To make the LPSFG prototype into a practical harsh environment sensor, the following work can be considered in two aspects: sensing structures and signal analysis. With regard to structures, firstly, a variety of BC gratings should be grown with different growth settings (grating length, grating period and FAM) for determining the best combination that produce the strongest BC effect; secondly, appropriate cladding materials such as zirconium dioxide or polycrystalline alumina can be used to coat the LPSFG to provide a cladding with a higher refractive index (~1.76) as well as decreasing the scattering loss. Lastly, as with the SCBBR and SCFPI sensors, the LPSFG needs to be connected to conventional fibres such as silica fibres for further signal transmission and analysis, which can be achieved by the fusion splice technique [8.4]. Regarding signal analysis, the peak tracking method [8.5, 8.6] can be used to determine the relationship between temperature change and wavelength shift thanks to the BC effect. Once the calibration of temperature and wavelength shift is established, the high sensitivity advantage of LPFG temperature sensors can be combined with the outstanding high-temperature resilience of the sapphire material, leading to a new type of high-temperature harsh environment sensor.

In addition to potential sensing ability, BCG fibres also have a particular characteristic in their output beam thanks to their unique grating structure fabricated by the MSV growth technique. In the preliminary test, a bare BCG fibre with a length of only 4.5 cm, without cladding, has shown obvious collimated light properties such as sharp focusing and high directionality from using a conventional white light source. Since the BCG beam can be generated without cladding, and the fact that the shape of the spectrum of the input light is unaltered, only the form of the output light is changed. Therefore, it could be used in a relay or cascade with other types of sensor such as FPI and FBG; the resonance spectrum of the other sensors can be passed on by a length of BCG fibre, without alteration, for substantially greater distances and with less attenuation, which can help to achieve remote sensing for various sensors in special environments. Also, by cladding and changing the period of BC gratings, the wavelength of the RP can be manipulated to fit the RW of other sensors, for example, the RP of FBG sensors. Thus, by transmitting a sensing signal through a length of BCG fibre, the signal at the RW of the sensor can be enhanced for both transmission and detection, ultimately improving the resolution and accuracy of the sensor.

BC fibres not only have potential uses in the OFS field; as BC coupling beam possesses some “coherent” beam advantages, including a directional beam, reduced light-emitting surface characteristics, it can also help form a future light source, in this case, this could be a white laser [8.6] or a laser-based white light source [8.7]. As a latest research topic: white light lasers have numerous applications at present and in the future. Since white lasers are more energy-efficient and luminous than conventional LEDs, they could be used for producing new types of lighting and display systems [8.7]. Also, white lasers could help to develop visible light communication, known as Li-Fi, which encodes information at an ultra-high frequency, with enough range to cover a living space. Compared with Wi-Fi, Li-Fi has particular potential advantages in terms of safety and security, speed, bandwidth, and energy efficiency [8.8]. Plus, as white light covers the total visible spectrum, it can provide a full range of colours. This advantage can contribute to confocal microscopes in biomedical studies and applications where a light source with tuneable colour and sufficient intensity is required for simultaneous excitation of a variety of samples [8.9].

Research on white lasers began in 2011, when Sandia National Labs combined four laser beams (yellow, blue, green and red) from four separate large lasers to produce high-quality white light [8.6], inspiring others to advance white laser technology. Later, in 2015, researchers at Arizona State University used three novel nanosheets in parallel, each allowing laser action within one of the three elementary colours, to demonstrate a semiconductor laser device that is capable of lasing any visible color [8.8]. Although there were still significant obstacles to overcome before applying this concept into white laser applications, it was a big step in development. In 2019, a new white lighting system was demonstrated by E Ning and his colleagues, which used a GaN laser diode to excite colour converters at different driving conditions, suggesting that a laser-based white light source can be used in high-efficiency illumination applications [8.7]. In this thesis, the collimated and concentrated light has been obtained with a 4.5-cm-long single-crystal sapphire grating fibre from a conventional white light source. Compared with other methods, this method not only has a simpler and more straight forward construction procedure, but also reduces the cost of components by simply using a conventional white light source instead of lasers. Although the results from the preliminary tests are limited, this does provide a new concept for further development of white lasers. Essentially, instead of generating a white laser beam based on lasers and innovative technologies, it could also be transformed from any general white light through different lengths of specially produced physical mediums such as the sapphire fibre BC gratings presented in this thesis. Depending on the required transmitting distance of the light beam, the size or length of the physical medium can be altered. With a lower cost of light source and ability to alter the amount of physical medium material required, the cost of generating white laser beams could be greatly reduced, especially for short-distance applications such as confocal microscopy, laser projection systems and short-distance illumination. Justified by the many merits and potential benefits to industrial, medical, scientific and commercial technologies listed above, there is considerable room for further worthwhile research in employing the BC effect with LPSFG. The direction of this research could be towards growing a larger set of samples with variance in parameters such as length, diameter, period, FAM etc. and refining the techniques that were showcased in this thesis.

8.5 References to Chapter 8

[8.1] J. Ding, A. Zhang, and L. Song, "Fiber-taper seeded long-period grating pair as a highly sensitive refractive-index sensor," *Photonics Technology Letters*, vol. 17, pp. 1247-1239, 2005.

[8.2] V. Grubsky and J. Feinberg, "Long-period grating fiber sensor with fixed resonance wavelength", in *Bragg Gratings, Photosensitivity, and Poling in Glass Waveguides*, Florida United States, 1999. ISBN: 1-55752-593-5

[8.3] O. L'Henaf, A. Zohrabyan and T. Galstian, "Development of fiber long period gratings for biological sensor applications," in *2008 SPIE,* vol. 7099. pp. 1-4, doi: 10.1117/12.805390

[8.4] Y. Li, T. Wei, J. Montoya and H. Xiao, "Measurement of CO_2-laser-irradiation-induced refractive index modulation in single-mode fibre toward long-period fibre grating design and fabrication," *Applied Optics,* vol. 47, pp. 5296-5304, 2008.

[8.5] S. Lee, R. Kumar and V. Nampoori, "Long-period gratings in multimode optical fibres: application in chemical sensing," *Optics Communications*, vol. 224, pp. 237-241, 2003.

[8.6] A. Neumann, J. Wierer, and W. Davis, "Four-color laser white illuminant demonstrating high color-rendering quality," *Optics Express*, vol. 19, pp. 982-990, 2011.

[8.7] E. Ooi, X. Sun, B. Ooi, T. Ng, and C. Shen, "Study on laser-based white light sources," in *Light-Emitting Devices, Materials, and Applications*, 2019. [online] Available: http://dx.doi.org/10.1117/12.2511094.

[8.8] F. Fan, S. Turdogan, Z. Liu, D. Shellhammer, and C. Ning, "A monolithic white laser," *Nature nanotechnology*, vol. 9, pp. 796, 2015.

[8.9] R. Borlinghasu and L. Kuschel (2012, Jun.). *White light laser the ultimate source for confocal microscopy*. [online] Available:https://www.leicmicarosystems.com/science-lab/white-light-laser

Chapter 9 – Conclusions and Future Work

Chapter 9 – Conclusions and Future Work

9.1 Conclusions

OFSs provide advantages of immunity to EMI and the ability to perform relatively cheap spatial sensing in places where space is limited. In today's energy and manufacturing industries, there is an increased requirement for instrumentation that can survive in harsh environments such as that would require a resistance to high temperature and strong radiation damage. Single crystal sapphire is a radiation hard material with a high melting point of 2050 °C. Thus, sapphire fibres are an excellent candidate for sensor applications in harsh environments. The principal work of this project focused on fabricating high-quality sapphire fibres with the LHPG technique for potential sensor applications. Based on the fundamental principle of OFSs, combined with the growth technique, different innovative sensor structures were produced for further development. As a result, three types of sapphire fibre based optical sensing structures were successfully designed and fabricated. One of three sensing structures was selected for further optical tests with an aim to present its sensing feasibility as a potential harsh environment sensor. Therefore, the major achievements and innovations of this project are summarized and listed below.

1. A high-quality SCF growth system, the LHPG system, has been successfully developed and evaluated, with the calibration of both hardware and software for straight and grating sapphire fibres. In this work, growth issues such as the transient bump structure and the asymmetric molten zone were solved through multiple trails. Regular striations were found in the grown sapphire fibres, which were proved to be seed-orientation related facets in sapphire fibre growth. The striations were eliminated by applying the c-axis sapphire seed for growth. The successful growth of quality sapphire fibres was achieved with a minimum diameter of 300 μm, its excellent signal transmission (150 to 3200 nm) capacity over the temperature range from room temperature to over 1000 °C can provide an advantageous condition for the development of harsh environment sensors.

2. A SiC-based sapphire capillary BBR sensor was successfully designed and fabricated. With combinations of the advantages of two excellent high-temperature materials, this new BBR sensor was not only relatively inexpensive to produce, but also more robust than conventional thin-film based BBR sensors. With the flexible use of the LHPG method, the size and shape of the SiC-sapphire blackbody cavity can be controlled, which could help to study the range and intensity of received radiation in sensor experiments. In the sensing system build process, different heating sources were tested and evaluated. As a result, furnace heating became the preferred heating method due to its good stability in temperature rise and heat control functions. A 14 cm length of sapphire fibre was grown for signal transmission, however, due to the long length and large loss of the unclad sapphire fibre, it was considered not suitable for the experiment. Optimized transmission approaches that combines the advantages of both sapphire fibres and conventional high-temperature fibres were proposed.

3. The design and fabrication of a novel air-based sapphire capillary FPI sensor was carried out. Different fabrication methods were applied. As a result, the crystal insertion method was considered as the most effective method to create a high-quality inner mirror of FPI. Compared with other methods, through this method, the size, toughness, and angle of the inner mirror can be controlled for a strong, clear, and orientated reflective signal in the FPI sensor. Also, the reduction in the use of high-temperature bonding material could further improve the durability and stability of the FPI sensor in high-temperature environments. Different sensing systems were designed, built and tested. The most challenges were the transmission and detection of the small reflection signals generated by the SCFPI sensor. Thus, after comparing the results of tests on different sensing systems, the coupler-based FPI system was selected as the suitable sensing system for the SCFPI sensor due to its low-loss transmission property. The design and selection of each component in the new coupler-based FPI system were also presented.

4. LPG has been successfully inscribed in sapphire fibres by the MSV technique in the LHPG growth process. Compared with the dicing method reported [9.1], this innovative method produced LPSFGs with distinct advantages in many aspects including but not limited to success rate, quality, sensing capability, cost, flexibility

and potential. An optical fibre sensor system has been developed to test the feasibility of the LPSFG sensor. A strong and clear grating effect was found in the optical test, where the RW of the LPG was found in the form of the RWR for the first time. The RWR showed evident response to the RI change of the cladding oil in the experiment, which further proved the very competent sensing capability of the LPSFG.

5. The BC effect was found in LPSFG for the first time. With the characteristics of an increased output signal and a sharp RP spectrum, the BC effect compensated some of the limitations of the original LPSFGs, which could greatly improve the accuracy and the resolution of the sensor. The sensing ability of the BC LPSFG sensor was further verified by the RI sensing experiment. The result indicated that the sensor showed a clear wavelength shift in terms of faster response, higher resolution, and higher accuracy, than that of the LPSFG without the BC effect. A specially designed temperature sensing system was built for the purpose of testing the temperature response of the sensor. The experiment achieved the temperature sensitivity of 2.5 nm/ °C and the results exhibited a strong linear relationship between the wavelength shift of the RP and temperature change, successfully proving the excellent temperature sensing ability of the sensor and therefore laid a solid foundation for further development of the ultimate high-temperature harsh environment sensor.

6. The unique BC beam of LPSFG was firstly found and characterised. It has a smaller divergence angle (6°) than that of straight fibre and normal grating without BC effect (80°), showing significant advantages in concentration, directionality, and transmission in the beam measurement. With its directional, collimated and concentrated beam properties, the BC beam showed great potential for applications not only in the optical sensor field such as remote sensing, low loss air transmission, but also in the field of laser devices in general as it provided a new concept and example to develop a novel white laser.

In summary, high-quality sapphire fibres were successfully fabricated, three sapphire fibre-based sensors were designed and fabricated, and one prominent candidate, the LPSFG sensor presented a good sensing capacity in the optical experiments. With the innate advantages of sapphire fibre, this unique LPSFG could result in a new generation of harsh environment sensors. The aim of this project was achieved, but in addition some breakthroughs were also made during the investigations, for example, with regard to the BC effect and BC beam. These breakthroughs could open up new avenues for exploration and applications in both the OFS and laser field. The results in the thesis can be used as input for higher-level development of the sapphire fibre-based BBR, FPI and especially LPG sensors, and can also function as an operating manual that would allow one to reproduce and develop these sensor structures with the LHPG technique for further work.

9.2 Further Work

Further work can be divided into two aspects: fibre growth and sensor development. For the fibre growth work, it is recommended to advance the LHPG system development in both hardware and software. Although quality sapphire fibres can be fabricated with the current system, it costs one too much time and energy in the alignment and monitoring before and during the growth. As an example, to ensure high quality, manual fine adjustment of the position of the source rod during the grating growth needs to be performed every 5 to 10 minutes during the 90 to 120 minutes of each LPSFG growth. To bring about a higher yield and lower cost for the growth, piezoelectric motors, a closed loop system, a beam expander, and a real-time diameter measurement function could be added into the system to improve the automation and precision of product.

For the sensor development work, as the work in this thesis was mainly focused on the fabrication of OFSs in terms of practical aspects, further work could include theoretical research and simulation, which could benefit the sensor system development and optimization. For instance, in the study of the BBR sensor, a detailed investigation of the relationship between radiation characteristics and the shape and size of the blackbody cavity would be valuable in fabricating suitable SiC-sapphire cavities fit for purpose. For further experimental work on sensor development, BBR and FPI could be tested for their optical response with applicable components and devices. Like the LPSFG sensor, new types of BBR and FPI sensors may result in unexpected breakthroughs during the investigation of their sensor performance. In terms of the LPSFG sensor, the further work can be focused on the study of the BC effect. Gratings with different value of diameter, length, period and FAM could be fabricated in different groupings to study their influence on the BC effect as well as the BC beam. This could help to explore the specific generating conditions of the BC effect in LPSFG, thus thereafter optimise the sensor performance and the beam quality.

It is worth noting that the main challenge in the development of the LPSFG sensor is that sapphire fibres were fabricated without cladding, which makes it difficult to obtain the RW of the LPG in air. To completely achieve production and commercialisation of the LPSFG sensor in practical applications such as a high-temperature or strain sensor for harsh environments, the grating fibres need to be cladded properly. Thus, study on sapphire fibre cladding should also be included in further sensor development work. Since SCFs have started being used in different sensor applications, the absence of a stable and effective cladding that is as durable as sapphire in harsh environments has always been a key technological barrier to widespread sapphire fibre-based OFSs. To expand the commercial applications of sapphire fibres, different groups of researchers have been especially focused on the development of an appropriate cladding for sapphire fibres. In the past ten years, sapphire fibre cladding strategies have been developing swiftly and steadily. Different sapphire fibre cladding, and coating techniques include magnesium aluminate spinel coating [9.2], hydrogen implantation [9.3, 9.4], nanoporous alumina cladding [9.5, 9.6], zirconium dioxide coating, polycrystalline alumina [9.7], and silica-based cladding [9.8]. These have emerged under the efforts of researchers from different parts of the world, pushing the highest acceptable temperature of the thermally stable cladding of sapphire fibres to 1700 °C [9.4], which greatly improved the operating temperature of OFSs. Thus, in further work, one could cooperate with partners who are focused in the cladding direction, so that both the original fabrication and subsequent cladding process in the sensor development can be manipulated holistically. Through further development, a new type of sapphire fibre sensor with numerous advantages could be active in the market of harsh environment sensors.

9.3 References to Chapter 9

[9.1] S. Nam, C. Zhun, and S. Yin, "Recent advances on fabricating in-fiber gratings in single crystal sapphire fibre," in *Conference on Photorefractive Fiber and Crystal Devices - Materials, Optical Properties and Applications*, Denver, 2004, pp. 147-155. doi: 10.1117/12.558656

[9.2] H. Chen, M. Buric, P. Ohodnicki, J. Nakano, B. Liu, B. Chorpening, "Review and perspective: Sapphire optical fiber cladding development for harsh environment sensing," *Appl. Phys. Rev*. vol. 5, pp. 2-19, 2018.

[9.3] W. Spratt, M. Huang, T. Murray, and H. Xia "Optical mode confinement and selection in single-crystal sapphire fibers by formation of nanometre scale cavities with hydrogen ion implantation," *J. Appl. Phys*, vol. 114, pp. 1-7, 2013.

[9.4] P. Aleksandrov, N. Belova, K. Demakov, and S. Shemardov, "On the generation of charge-carrier recombination centers in the sapphire substrates of silicon-on-sapphire structures," *Semiconductors*, vol. 49, pp. 1099–1103, 2015.

[9.5] H. Chen, F. Tian, J. Kanka, and H. Du, "A scalable pathway to nanostructured sapphire optical fiber for evanescent-field sensing and beyond," Appl. Phys. Lett., vol. 106, pp. 102-111, 2015.

[9.6] H. Chen, F. Tian, K. Liu, J. Kanka, H. Du, "Strategy and method for nanoporous cladding formation on silica optical fiber," *Opt. Lett*, vol. 41, pp. 2831-2834, 2016.

[9.7] M. Sherif, I. Kamel, F. Ko, M. Shaker, D. Roth, B. Lerch, and S. Swickard, "Proceedings of the 17th Annual Conference on Composites and Advanced Ceramic Materials," *in 17th Annual Conference on Composites and Advanced Ceramic Materials* (John Wiley & Sons, Inc., 2008), vol. 14, pp. 437–444.

[9.8] C. Lai, C. LO, D. Nguyen, J. Huang, W. Tsai, and Y. Ma, "Atomically smooth hybrid crystalline-core glass-clad fibers for low-loss broadband wave guiding," *Opt. Express*, vol. 24, pp. 20089-20106, 2016.